IN-PROCESS SENSING OF WELD PENETRATION DEPTH USING NON-CONTACT LASER ULTRASOUND SYSTEM

A Dissertation
Presented to
The Academic Faculty

by

Matthew Douglas Rogge

In Partial Fulfillment
of the Requirements for the Degree
Doctor of Philosophy in the
School of Mechanical Engineering

Georgia Institute of Technology
November 2009

IN-PROCESS SENSING OF WELD PENETRATION DEPTH USING NON-CONTACT LASER ULTRASOUND SYSTEM

Approved by:

Professor I. Charles Ume,
Committee Chair
School of Mechanical Engineering
Georgia Institute of Technology

Professor Nader Sadegh
School of Mechanical Engineering
Georgia Institute of Technology

Professor Ye-Hwa Chen
School of Mechanical Engineering
Georgia Institute of Technology

Professor Jennifer E Michaels
School of Electrical and Computer Engineering
Georgia Institute of Technology

Professor George Vachtsevanos
School of Electrical and Computer Engineering
Georgia Institute of Technology

Date Approved: November 13, 2009

ACKNOWLEDGEMENTS

I would like to thank my advisor, Dr. Charles Ume, for his guidance, advice, and mentorship throughout this research.

I would like to thank my thesis committee Professors Nader Sadegh, Ye-Hwa Chen, Jennifer Michaels, and George Vachtsevanos for their expertise and valuable suggestions.

I would also like to thank my colleagues for their support, feedback and collaboration throughout my studies: Dr. Bao Mi, Dr. Akio Kita, Tsun-Yen Wu, Tyler Randolph, Dr. Reinhard Powell, Dr. Jin Yang, Dr. Lizheng Zhang and Dr. Wei Tan.

Finally, I wish to thank my family, friends, and loved ones for their support, encouragement, and inspiration.

TABLE OF CONTENTS

LIST OF TABLES

LIST OF FIGURES

SUMMARY

Welding is one of the main methods used to join structural members. Of the many types of welding processes, Gas Metal Arc Welding (GMAW) is one of the most widely used. One of the largest challenges involved in production of welds is ensuring the quality of the weld. Automatic control of the welding process requires non-contact, non-destructive sensors that can operate in the presence of high temperatures and electrical noise found in the welding environment. Laser generation and Electromagnetic acoustic transducer (EMAT) reception of ultrasound were found to satisfy these conditions. Previous research worked towards development of ultrasonic time of flight based weld penetration depth measurement techniques. One such technique, the Rayleigh Generation Longitudinal to Shear Time of Flight (RGLS ToF) technique was developed recently.

The objective of this research was to compensate for the changes in time of flight exhibited when the RGLS ultrasonic technique is used during welding, thereby reducing penetration depth measurement error. A numerical model based on generalized ray theory was developed to determine the dominant frequency and means through which Rayleigh waves reach the bottom surface of a plate. The model results were validated experimentally. The underlying assumptions made when developing the technique were investigated and shown to be incorrect. In addition, the RGLS wave was not present in received ultrasonic signals.

Since the RGLS wave was not present in the received ultrasonic signals, an alternative wave path was selected. An automated weld inspection system was developed to permit inspection of welds during and after welding. Using the inspection system,

experiments were performed to identify the wave paths that reach the EMAT. Of the candidate wave paths, the longitudinal diffracted longitudinal to shear (LdLS) wave was found to be the strongest candidate that is not subject to interference by other waves. A theoretical model was developed to determine the optimal placement of the laser generation location and EMAT. The technique was then validated experimentally and found to perform well.

The inspection system was then used to inspect samples during and after welding. The times of flight of the LdLS wave were measured under both conditions and shown to be larger during welding because of the decreased wave speeds at elevated temperature. The root mean square (RMS) difference in wave speed was shown to decrease as the sensing system was placed further away from the welding torch. The differences in time of flight due to the temperature field during welding were large enough to produce negative penetration depth measurements and errors as large as 5 mm. In order to improve the in-process penetration depth measurement, two neuro-fuzzy penetration depth prediction models were developed. The first model compensates for the temperature induced error by producing an estimate of the room temperature time of flight based on the in-process time of flight and the time history of the wire feed rate. This model can be trained without performing any destructive measurements. The performance of the model was very good. The RMS difference in the estimated time of flight and the post-welding time of flight was reduced by a minimum of 68% and as much as 88%. The estimated time of flight was used to measure the penetration depth. The root mean square error (RMSE) of the penetration depth measurement was comparable to that obtained using the LdLS technique after welding. The second model predicts penetration depth directly by using destructively obtained measurements in the training process. This model performs significantly better than the offline LdLS technique and the time of flight error compensation model. By using the penetration depth prediction models, the accuracy of laser ultrasonic techniques

has been drastically increased. The in-process weld penetration depth measurement techniques developed in this research are effective and is suitable for application towards real-time weld quality monitoring and control. Real time weld quality control has the potential to drastically reduce costs, material waste, and human injury and increase throughput of manufacture of welded structures.

CHAPTER I

INTRODUCTION

Welding is one of the main methods used to join structural members. Of the many types of welding processes, Gas Metal Arc Welding (GMAW) is one of the most widely used. In GMAW, members are joined through the application of heat and filler material. The heat is applied by sending current through an electric arc between an electrode and the work piece. The electrode in GMAW also serves as filler material. As the wire electrode is fed towards the work piece, it is melted by the welding current and transferred to the work piece. There are three transfer modes in which the filler material may be transferred. The electrode can be dipped into the weld pool (short-circuited mode), material may be dropped into the weld pool (globular transfer mode) or material may be sprayed from the electrode to the work piece (globular transfer mode). Shielding gas is used to prevent gaseous inclusions in the weld [3].

Control of the welding process is commonly performed by using pre-determined input parameters or by operator supervision. The input parameters are arc voltage, wire feed rate, torch velocity, torch standoff height, and torch orientation. The optimal input parameters for a particular weld are chosen by following best practice guidelines and/or by performing test welds. This practice can yield acceptable results when little variation is present in the work piece and welding environment. Misalignment of the work piece, poor surface preparation, and disturbances in the welding process can lead to defects. When an operator controls the welding process, information regarding the arc voltage, instantaneous current and/or temperature profile on the surface of the work piece are displayed and corrections are made at the discretion of the operator. This may be cost prohibitive because of the high experience levels

required of the operator.

When defects are present in a weld, strength may be severely compromised. Weld quality inspection is therefore a major component of the manufacturing process for welded components. Weld quality can be assessed either in-process as welding is performed or off-line after the process has been completed. Off-line inspection may be performed by a number of means. Cut checks, radiographic, and ultrasonic methods are common. The use of cut-checks is undesirable as the technique is destructive in nature. Only a subset of the produced parts may be checked and checks are typically only performed on a few location for each part. Therefore defects may go undetected. Methods involving X-rays are expensive and may be hazardous if the proper safety precautions are not taken. Ultrasonic methods directly detect defects and weld geometry. However, interpretation of the received ultrasound may be difficult. Although off-line inspection may detect defects, it is desirable to prevent them in the first place. Thus, in order to realize real-time welding control, in-process quality estimation is necessary.

In-process weld inspection has a number of advantages over off-line inspection. Unlike inspection via cut checks, the entirety of the weld may be inspected with a much higher number of potential defects detected. In addition, parts lacking defects are not damaged. Since in-process inspection is performed while welding takes place, time and cost can be reduced because of the lack of need for human inspection. In addition, flaws may be detected before the part is completed, saving time, material, and reworking costs. Perhaps the most important advantage is that in-process weld quality inspection systems can be used as sensors for implementation of real-time welding control. One of the key components of weld quality is the weld bead geometry. Figure 1 shows the three most important bead geometry properties, weld reinforcement height, weld reinforcement width, and penetration depth. Of these three properties, penetration depth is the most difficult to measure and directly determines the load

bearing capability of the weld.

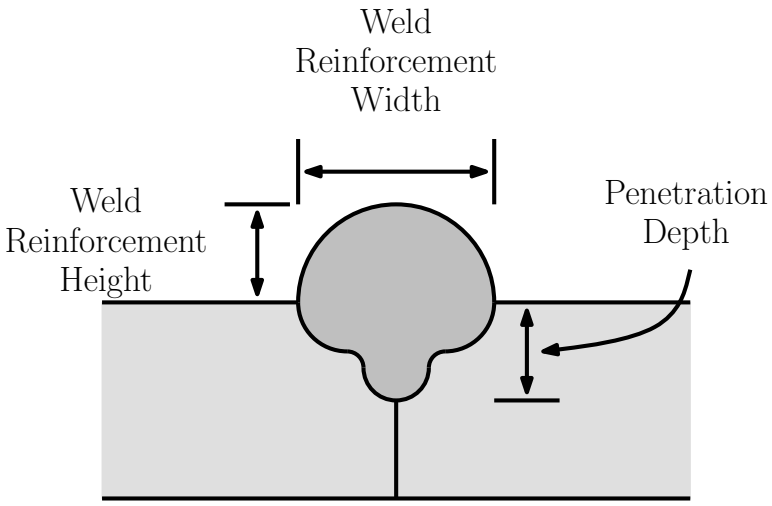

Figure 1: Definitions of weld geometry properties

Many techniques and technologies have been developed to measure weld penetration depth. The four general categories are through-arc sensing of arc current and voltage, thermal distribution measurement, weld bead and pool measurement using machine vision, and ultrasonic techniques.

1.1 Sensing of Arc Current and Voltage

One technique that requires little additional equipment is through-arc sensing of current and voltage. The arc voltage and current are measured during welding. The operating principle for this technique is to detect disturbances in the welding process by detecting disturbances in the arc voltage and current. The welding arc and weld pool are modeled as resistors. A constant voltage source is prescribed by the welder. This forms a circuit of two resistors in series. By monitoring disturbances in the voltage and current in this circuit, disturbances in the welding process may be detected. The main disadvantage of this method is that the weld geometry and defects cannot be determined directly, only disturbances of the welding process. In addition, disturbances in the measured arc voltage and current may be present without disturbances

in weld quality. There are two main advantages of through arc sensing of current and voltage: the system is non-contact and economical [1, 11, 31, 47, 57, 7, 8].

1.2 Thermal Distribution Sensor

As the GMAW process is characterized by high temperature and thermal gradients, this information can be used to infer weld geometry. An infrared CCD camera is used to capture the thermal profile on the surface(s) of the material. The temperature profile at the top surface of the work piece can be used to determine weld pool geometry. By measuring the thermal profile on the top and bottom surfaces, the thermal gradient can be used to calculate the penetration depth of the weld. Fitting numerical results to the measured temperature profile(s) can be used to estimate internal material temperatures. Once the internal temperatures are estimated, the penetration depth may be determined. Advantages of this method are that it is non-contact, can measure weld bead geometry directly and uses readily available sensors. The major disadvantages of this method are its inability to measure internal weld defects and the need for access to the reverse surface for penetration depth estimation [23, 44, 54, 57, 10, 25].

1.3 Machine Vision

The machine vision method uses at least one CCD sensor and image processing techniques to determine the weld pool and reinforcement geometry. This information is used to infer weld penetration depth. Infrared CCD sensors may be used to image the weld pool directly. Weld reinforcement has been measured by using structured light based techniques. These techniques direct laser light of known shape (such as a line or grid) onto a surface. The shape will be distorted based on the geometry of the surface. This permits measurement of reinforcement height and width [61]. This method has advantages similar to the thermal distribution sensor. It is non-contact,

uses inexpensive, readily available sensors and can measure the weld pool shape directly. Defects internal to the weld cannot be detected, but they can be predicted by monitoring the weld pool shape [12, 18, 49, 19, 34].

1.4 Ultrasonic Inspection

Ultrasonic inspection methods involve generation of ultrasonic waves which then interact with the weld. Internal defects cause the incident wave to reflect and or diffract. These waves are then detected and analyzed [13]. Porosity can be measured by detecting changes in the frequency spectrum of the received ultrasound. Weld geometry can be measured using Time of Flight (ToF) methods. Penetration depth, weld reinforcement height, reinforcement width can be measured [43]. In addition, ultrasonic techniques can be used for seam tracking [59]. The system may be non-contact if laser and/or Electromagnetic Acoustic Transducers (EMATs) are used to generate and receive the ultrasound. ToF methods require accurate knowledge of the sound speed(s) to determine geometric quantities. For known, uniform material temperature profiles, this is not an issue. However, for the in-process welding environment, high temperatures may effect the accuracy of such systems [40].

The main effect of elevated temperature on the accuracy of ToF based ultrasonic techniques is the dependency of wave speed on temperature. In addition, non-uniform temperature fields can cause the path followed by the ultrasound to deviate from a straight line, changing its length. Both of these effects introduce error in the geometry calculation. The temperature induced error may be minimized by placing the sensing system a large distance from the welding torch [33]. However, this causes the time difference between the welding of the material and sensing of the weld quality to increase. This may be acceptable for in-process monitoring, where the quality information is used to determine if and where any repairs are needed. When the system is to be used as a sensor for real time welding control, the increased delay

reduces stability margins and may complicate controller design.

This thesis is focused on realizing in-process ultrasonic weld penetration depth measurement for the purpose of real time control. The work in this thesis includes: 1) development of an automated weld inspection system capable of coordinating the welding process and inspecting the weld both while and after welding occurs; 2) an analysis of the underlying assumptions of the RGLS ToF weld penetration depth measurement technique including numerical modeling and experimental measurement of ultrasonic Rayleigh wave propagation due to pulsed laser sources; 3) a theoretical model for optimization of laser ultrasonic sensing systems for maximum signal amplitude in order to increase performance during welding; and 4) analysis of the effects of welding temperature profiles on time of flight of ultrasonic waves and development of temperature induced error compensation model.

This dissertation is organized as follows. Chapter 2 provides background for this work, including weld process monitoring techniques, wave propagation, laser generation of ultrasound, EMAT reception of ultrasound, and ultrasonic weld quality measurement techniques. Chapter three describes the in-process weld control and inspection system built for this research. Chapter four details an investigation of Rayleigh wave propagation in elastic plates. A numerical model based on generalized ray theory is developed to calculate the response of the plate to a laser ultrasonic source. The model is validated experimentally. Chapter five presents the process of optimizing the placement of inspection system components for maximum signal amplitude. Chapter six presents an analysis of the effects of the temperature field present during welding on ultrasound time of flight. A dynamic neuro-fuzzy model has been developed to compensate for errors caused by elevated temperatures present during welding. Chapter seven provides conclusions, contributions, impact of this work and recommendations for future research.

CHAPTER II

BACKGROUND

Background related to the work in this thesis is presented in this chapter. This review includes weld process monitoring techniques, ultrasonic wave propagation, laser generation of ultrasound, Electromagnetic Acoustic Transducers (EMATs) and ultrasonic weld quality measurement techniques.

2.1 Weld Process Modeling

Various types of models have been researched in order to model the welding process. The process is significantly nonlinear and quantities are spatially distributed.

Song and Hardt developed a quasi-static model based on solutions of the 2-dimensional heat equation [57]. The model is applied to penetration depth measurement by iteratively adjusting parameters of the model until the difference between the experimental and simulated surface temperature profiles is minimized. The penetration depth of the weld is estimated by finding the largest depth below the torch at which the liquidus temperature is reached. Computation of the model was shown to be short enough to permit real-time control at a rate of 2 Hz, implying computation time was significantly less than 500 ms.

Zhao et al. developed a three-dimensional dynamic analytical model that predicts weld pool geometry based on welding parameters [62]. The model includes heat transfer, fluid dynamic, surface tension, and arc dynamics in its formulation. It has been shown to accurately predict weld pool geometry for step changes in the parameters of the Gas tungsten arc welding process. The authors do not comment on the computation time necessary to perform the computations in the model, but it is expected that it is significant.

Andersen and Cook introduced a scheme in which the unobservable geometric quantities are determined from an artificial neural network (ANN) [2, 21]. The steady-state geometric weld properties were predicted based on static welding parameters using an artificial neural network (ANN). The ANN was trained using data obtained experimentally and shown to be accurate. Nagesh et al. also studied the effects of various static shielded arc welding parameters on geometric properties including bead height, bead width and penetration depth as well as the size of the heat affected zone [45]. Computation of ANN output is typically very fast when compared to numerical models.

Various researchers have used neuro-fuzzy systems to assist in welding parameter selection based on desired weld geometry. Similarly to work using ANNs, the models assume steady state and cannot model the dynamic nature of the welding process. However, much attention has been focused on using neuro-fuzzy systems for modeling of dynamic systems. Neuro-fuzzy inference systems have been shown to be very useful for nonlinear system identification for a variety of applications. A survey of various neuro-fuzzy techniques is presented in [6].

2.1.1 Neuro-Fuzzy Inference Systems

When the system to be identified cannot be modeled using a traditional linear approach, a nonlinear model type must be used. One such model type is the neuro-fuzzy inference system. The neuro-fuzzy paradigm is a way to organize the computation of a fuzzy inference system (FIS) in a way that permits use of training tools from the field of neural networks. Fuzzy inference systems are nonlinear systems that produce an output based on linguistic rules. One type of FIS that is particularly useful for nonlinear system modeling is the The Takagi-Sugeno FIS [58]. The Takagi-Sugeno model can be thought of as a smooth piece-wise affine model. The output of the FIS is determined by evaluating a set of linguistic rules. The rules for a two input first

order Takagi-Sugeno FIS with two membership functions per input are of the form

$$\text{IF } X \text{ is } A_1 \text{ AND } Y \text{ is } B_1 \text{ THEN } f_1 = p_1 x + q_1 y + r_1$$

$$\text{IF } X \text{ is } A_2 \text{ AND } Y \text{ is } B_2 \text{ THEN } f_2 = p_2 x + q_2 y + r_2$$

Where:

x, y	Inputs
A_i	Linguistic label associated with input X for rule i
B_i	Linguistic label associated with input Y for rule i
f_i	Output function corresponding to rule i
p_i, q_i, r_i	Parameters for affine output function f_i

The linguistic label is a term that holds meaning to the input. For example, three fuzzy sets may be defined with labels "small," "medium" and "large." For each rule, the extent to which the inputs satisfy the linguistic label A_i is defined by the membership function μ_{A_i}. Membership functions must satisfy $0 \leq \mu(x) \leq 1$ since the input cannot belong to any set with a membership greater than one and negative membership is not permitted. Many different membership functions have been used. One common membership function is the generalized bell function, defined in Eq. 1. The function is parameterized in order to vary its shape. The parameters a and b determine the shape of the function and parameter c determines the center of the function. The function is plotted in Figure 2 for parameters $[a, b, c] = [2, 4, 6]$. By changing the parameters of the membership functions, the input-output relationship of the FIS is altered.

$$\mu(x) = \frac{1}{1 + \left| \frac{x-c}{a} \right|^{2b}} \tag{1}$$

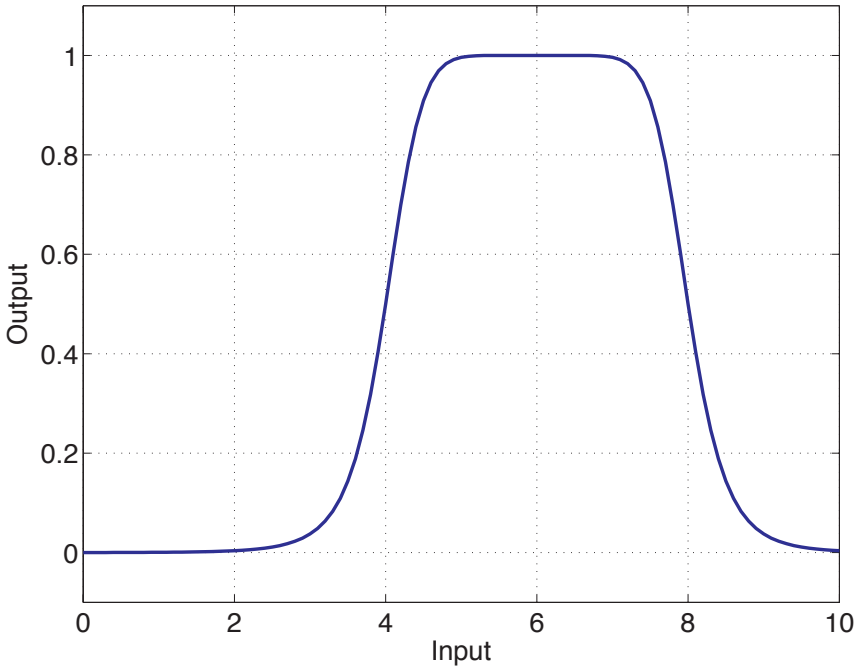

Figure 2: Generalized bell membership function for parameters $[a, b, c] = [2, 4, 6]$

The extent to which a rule is satisfied, w_i, (referred to as the firing strength) is determined by comparing the membership of the inputs to the labels A_i and B_i. Various techniques are found for making the logical AND statement. In this formulation, the product is used, but the $min()$ operation is also common. In this case, the product of the membership functions associated with that rule determine the firing strength as shown in Eq2. 2 & 3.

$$w_1 = \mu_{A_1}(x)\mu_{B_1}(y) \tag{2}$$

$$w_2 = \mu_{A_2}(x)\mu_{B_2}(y) \tag{3}$$

The output of the FIS, f, is the weighted sum of the affine output functions as in Eq. 4

$$f = \overline{w_1} f_1 + \overline{w_2} f_2 \tag{4}$$

The output functions are weighted by normalized firing strengths as in Eqs. 5 & 6.

$$\overline{w_1} = \frac{w_1}{w_1 + w_2} \tag{5}$$

$$\overline{w_2} = \frac{w_2}{w_1 + w_2} \tag{6}$$

Thus, the input/output relationship of the FIS is determined by the parameters of the membership functions (a, b, and c for the generalized bell functions) and the output functions (p, q, and r). The design process of a FIS involves changing these parameters until a performance goal is reached. For systems with few inputs and rules, this can be accomplished manually based on a designer's experience and knowledge of the system being modeled. When such information is not available, the design is much more difficult. Tools from the field of neural networks have been used to train fuzzy inference systems based on experimentally obtained data and/or simulation. Jang developed a training algorithm for training neuro-fuzzy inference systems based on a combination of nonlinear and linear optimization routines [29]. In order to apply tools developed for training neural networks to training fuzzy inference systems, the mathematical operations that make up the inference process are arranged as a nodal network as shown in Figure 3.

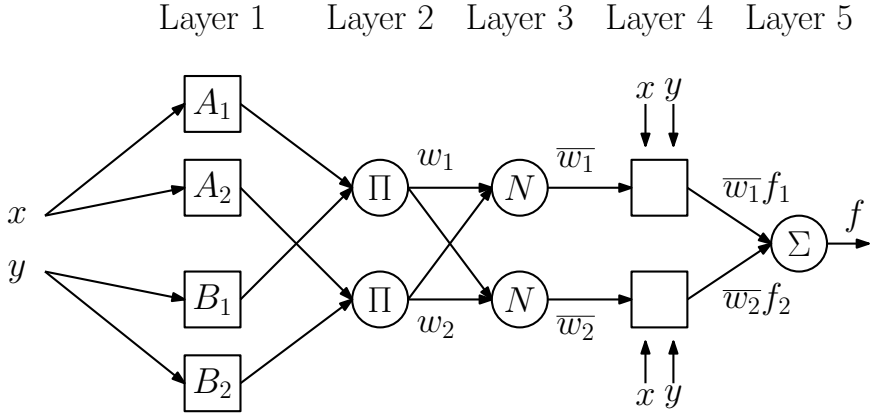

Figure 3: Neuro-fuzzy network structure following from [29]

While this does not change the computation of the output, it allows for use of

the back propagation algorithm during the training process. The back propagation algorithm is a very effective tool for training of nonlinear networks. The first layer contains the fuzzy input membership functions and determines the degree of membership of the inputs to each linguistic label. Layer two performs a product operation and produces the firing strength of each rule. Layer three normalizes the firing strengths. Layer four determines the output function for each rule and the fifth layer sums the weighted output functions to produce the FIS output. The Takagi-Sugeno type FIS employs linear output functions as described earlier. The hybrid learning algorithm described by Jang performs a least squares estimate to determine the parameters of the output functions and a gradient descent routine to determine the parameters of the nonlinear membership functions.

In a dynamic FIS, the inputs to the FIS are time dependent. The system can include moving average and autoregressive features. In a moving average model, the each input is delayed by some number of periods. Autoregressive models include feedback elements where the output of the system is delayed by some number of sampling periods and then used as an input to the system. As with any FIS, the task for the designer is to determine both the system structure and parameters. Specifically the number of inputs, signal fed into each input, membership function form(s), membership function parameters, and rule base must all be determined.

2.2 Propagation of Elastic Waves

In an elastic media, disturbances propagate through the media. This propagation is dictated by the wave equation. The wave equation for a three dimensional domain in Cartesian coordinates is shown in Eq. 7.

$$\mu\nabla^2\boldsymbol{u} + (\lambda+\mu)\nabla\cdot(\nabla\cdot\boldsymbol{u}) + \rho\boldsymbol{f} = \rho\ddot{\boldsymbol{u}} \tag{7}$$

Where:

$\boldsymbol{u}$:	Particle displacement
$\boldsymbol{f}$:	Force
μ, λ:	Lamé constants
ρ:	Mass density

Given Young‘s modulus and Poisson‘s ratio for a material, the Lamé constants may be calculated as shown in Eqs. 8 & 9.

$$\lambda = \frac{E\nu}{(1+\nu)(1-2\nu)} \tag{8}$$

$$\mu = \frac{E}{2(1+\nu)} \tag{9}$$

$$\tag{10}$$

2.2.1 Bulk Waves

In an isotropic elastic solid, two modes of bulk wave propagation are possible. Particle displacement may either be parallel or orthogonal to wave propagation. These propagation modes are called longitudinal and shear waves, respectively. Each propagation mode has a characteristic phase velocity at which the wave propagates, C_L and C_T, respectively. For 1020 steel, the longitudinal phase velocity is 5960 m/s whereas the shear phase velocity is 3240 m/s. These velocities are dependent only on material properties. The two phase velocities are determined by Eqs. 11 & 12, below.

$$C_L = \sqrt{\frac{\lambda + 2\mu}{\rho}} \tag{11}$$

$$C_T = \sqrt{\frac{\mu}{\rho}} \tag{12}$$

$$\tag{13}$$

For convenience, the ratio of the longitudinal to shear wave speeds, κ, is often used and defined below in Eq. 14.

$$\kappa = \frac{C_L}{C_T} \tag{14}$$

When a bulk wave is incident on a free surface, reflection will occur. This situation is depicted below in Figure 4. The angles at which the waves are reflected are functions of the phase velocities of the incident and reflected waves and angle of incidence. This relationship is given in Eq. 15.

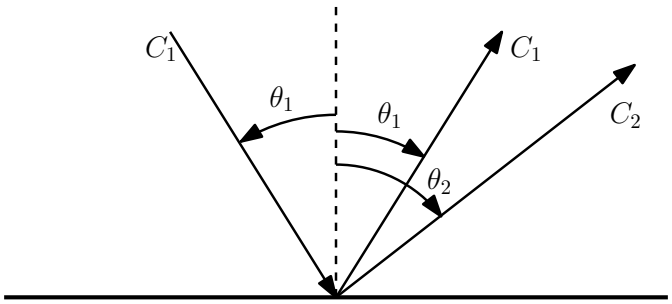

Figure 4: Mode Conversion of a bulk wave incident on a free surface

$$\frac{\sin\theta_1}{C_1} = \frac{\sin\theta_2}{C_2} \tag{15}$$

Where:

θ_1: Inclusive angle between incident wave propagation and surface normal

C_1: Incident wave phase velocity

θ_2: Inclusive angle between reflected wave propagation and surface normal

C_2: Reflected wave phase velocity

For the case of incident longitudinal waves incident at angle θ_L, longitudinal waves will be reflected at an angle equal to the incident angle. The angle of the reflected shear wave is determined by Eq. 16. The amplitudes of the reflected longitudinal and shear waves are determined by multiplying the incident wave amplitude by the reflection coefficients defined in Eqs. 17 and 18 and presented in Figure 5 for mild steel.

$$\sin\theta_T = \frac{\sin\theta_L}{\kappa} \tag{16}$$

$$\frac{A_L}{A_I} = \frac{\sin 2\theta_L \sin 2\theta_T - \kappa^2 \cos^2 2\theta_T}{\sin 2\theta_L \sin 2\theta_T + \kappa^2 \cos^2 2\theta_T} \tag{17}$$

$$\frac{A_T}{A_I} = \frac{2\kappa \sin 2\theta_L \cos 2\theta_T}{\sin 2\theta_L \sin 2\theta_T + \kappa^2 \cos^2 2\theta_T} \tag{18}$$

Likewise, for shear waves incident at angle θ_T, the shear wave will be reflected at an angle equal to the incident angle. Longitudinal waves may also be reflected, at angle θ_L as given in Eq. 19. The amplitudes of the reflected waves are determined by the reflection coefficients defined by Eqs. 20 and 21 and presented in Figure 6 for steel.

$$\sin\theta_L = \kappa \sin\theta_T \tag{19}$$

$$\frac{A_T}{A_I} = \frac{\sin 2\theta_T \sin 2\theta_L - \kappa^2 \cos^2 2\theta_T}{\sin 2\theta_T \sin 2\theta_L + \kappa^2 \cos^2 2\theta_T} \tag{20}$$

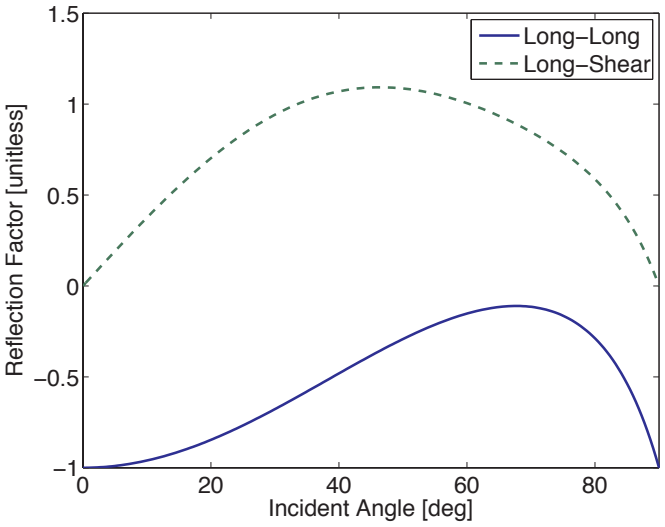

Figure 5: Reflection coefficients for incident longitudinal waves in steel

$$\frac{A_L}{A_I} = -\frac{\kappa \sin 4\theta_T}{\sin 2\theta_T \sin 2\theta_L + \kappa^2 \cos^2 2\theta_T} \tag{21}$$

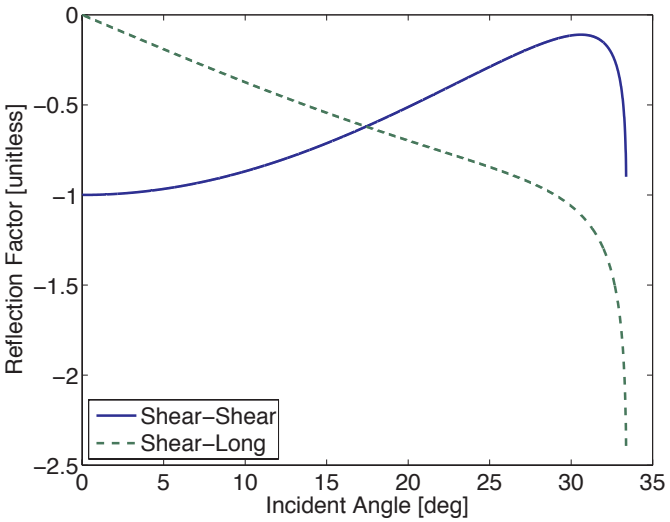

Figure 6: Reflection coefficients for incident shear waves in steel

For incident shear waves, there is a critical angle at which no shear or longitudinal waves will be reflected. The angle is dependent on material properties and is equal

to 33.4° for mild steel. The reflection coefficients for incident shear and longitudinal waves are used later when optimizing the placement of components of the weld penetration depth sensing system.

2.2.2 Rayleigh Surface Waves

Rayleigh waves propagate along the free surface of a medium. Rayleigh waves can be generated by PZTs with angle wedges, laser generation, and EMATs [24, 30]. They are characterized by particle displacement with components both parallel and perpendicular to wave propagation. The two components of displacement are 90^o out of phase with each other resulting in elliptical motion. The Rayleigh wave phase velocity can be determined by solving Eq. 22 for the real root less than C_T. For mild steel, solution of Eq. 22 results in a Rayleigh phase velocity equal to 3000 m/s.

$$\left(2 - \frac{C^2}{C_T^2}\right)^2 - 4\sqrt{\left(1 - \frac{C^2}{C_L^2}\right)\left(1 - \frac{C^2}{C_T^2}\right)} = 0 \tag{22}$$

The in-plane (u) and out-of-plane (w) displacements for a plane Rayleigh wave are given in Eqs. 23 and 24 and plotted in Figure 7. The amplitudes have been normalized to the out-of-plane displacement amplitude at the surface. The amplitudes decay quickly with respect to the product of wavenumber and depth below the free surface. For higher frequencies (and therefore wavenumbers) the amplitude decreases faster. Thus, the frequency content of the Rayleigh wave will vary with depth below the surface.

Rayleigh waves have been shown to be applicable for inspection over long distances and for determination of effects that are local to the surface such as residual stresses and surface breaking cracks.

$$u = \left(2 - \frac{Cr^2}{Ct^2}\right) e^{-\sqrt{1-Cr^2/Ct^2}kz} - 2\sqrt{1 - \frac{Cr^2}{Cl^2}}\sqrt{1 - \frac{Cr}{Ct^2}} e^{-\sqrt{1-(Cr/Cl)^2}kz} \tag{23}$$

$$w = -\sqrt{1 - \frac{Cr^2}{Ct^2}} \left(2 - \frac{Cr^2}{Ct^2}\right) e^{-\sqrt{1-(Cr/Ct)^2}kz} - 2e^{-\sqrt{1-(Cr/Cl)^2}kz} \tag{24}$$

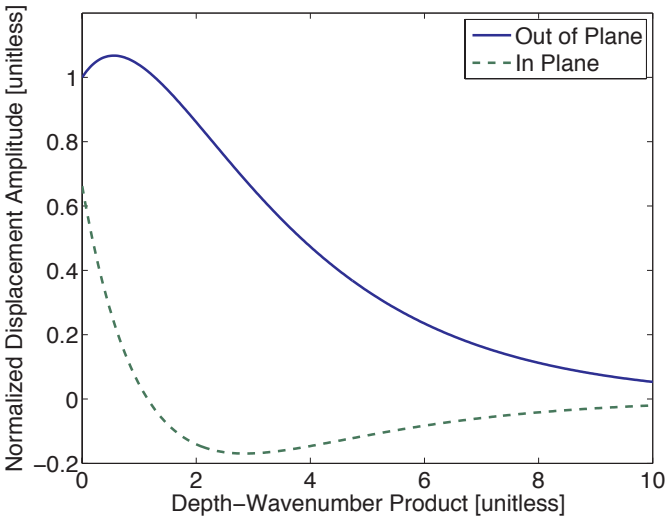

Figure 7: Rayleigh wave amplitudes as a function of depth wavenumber product

2.2.3 Diffraction of Elastic Waves by Crack Tips

When a bulk wave travels and reaches a crack, three phenomena occur: the wave is reflected from the crack surface, Rayleigh waves that travels along the crack, and diffracted waves will propagate away from the crack tip. Figure 8(a) depicts the wavefronts of an incident longitudinal wave and the reflected and diffracted waves. The figure illustrates the shadow zone, the region in the medium where only the diffracted waves are present. Incident waves will result in diffracted longitudinal and shear waves regardless of the mode of the incident wave.

The amplitudes of the diffracted shear and longitudinal waves are dependent on the incident angle and the angle at which the diffracted wave travels away from the crack tip. The diffracted wave potentials for incident plane longitudinal waves diffracting to longitudinal waves were originally derived by Chapman [17] and are given in Eq. 25. Ravenscroft et. al confirmed that these solutions approximate the amplitude of laser ultrasonic waves diffracted by thin slots and fatigue cracks [50].

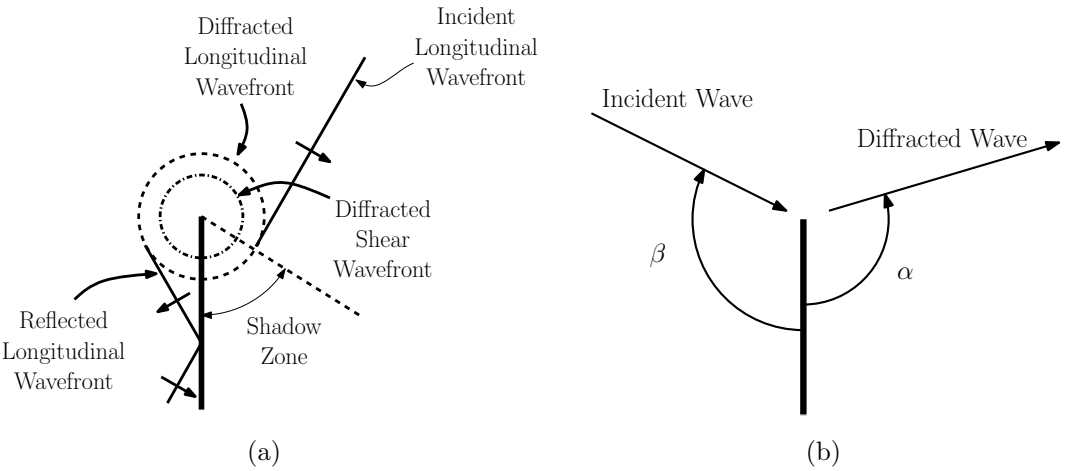

Figure 8: (a) Incident, reflected and diffracted wavefronts (b) Definition of angles α and β in Eqs. 25-30

$$\Phi = G(\alpha, \beta)(\lambda_p/R)^{1/2} e^{ik_p R} \tag{25}$$

$$G(\alpha, \beta) = \frac{\psi_1 + \psi_2}{D} e^{i\pi/4} \sin\frac{\beta}{2} \tag{26}$$

$$\psi_1 = \sin\frac{\alpha}{2}\left(2k_p^2\cos^2\beta - k_s^2\right)\left(2k_p^2\cos^2\alpha - k_s^2\right) \tag{27}$$

$$\psi_2 = 2k_p^3\cos\frac{\beta}{2}\cos\beta\sin 2\alpha\left(k_s - k_p\cos\alpha\right)^{1/2}\left(k_s - k_p\cos\beta\right)^{1/2} \tag{28}$$

$$D = 2\pi(k_s^2 - k_p^2)(\cos\alpha + \cos\beta)(k_o - k_p\cos\alpha)(k_o - k_p\cos\beta)K^+(-k_p\cos\alpha)K^+(-k_p\cos\beta) \tag{29}$$

$$K^+(\sigma) = \exp\left[-\frac{1}{\pi}\int_{k_p}^{k_s}\tan^{-1}\left(4x^2(x^2 - k_p^2)^{1/2}(k_s^2 - x^2)^{1/2}/(2x^2 - k_s^2)^2\right)\frac{dx}{x + \sigma}\right] \tag{30}$$

2.3 Laser Generation of Ultrasound

Laser generation of ultrasound is a non-contact means of generating ultrasound that is achieved by focusing laser light energy on the material surface.

Various laser types can be used to generate ultrasound. Q-switched lasers are capable of large power densities and short pulse durations (20ns typ.). The short duration of pulsed lasers result in broadband ultrasound [41]. Temporal modulation

permits tuning of the frequency content of the generated ultrasound. A sinusoidally modulated source can yield narrow band ultrasound if enough periods are generated [53]. There are three regimes of laser generation of ultrasound; thermoelastic, transition, and ablative.

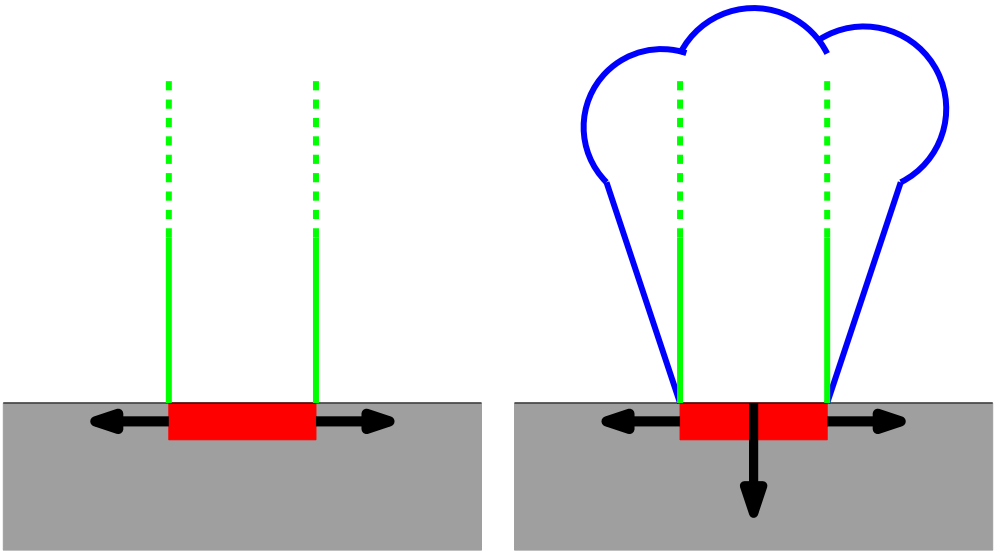

Figure 9: (a) Thermoelastic and (b) ablative generation of ultrasound

2.3.1 Thermoelastic Generation

Thermoelastic generation is achieved when a relatively low power density is incident on the material surface. In thermoelastic generation, the temperature of the material does not exceed the melting point. The incident energy causes the temperature of a thin layer of the material to heat very rapidly. The material expands with the temperature changes via the thermoelastic effect. If the laser source is circular and the laser beam diameter is less than approximately 1 mm, the resulting forces in the material can be modeled as a force dipole symmetric about the center of the circular laser source in the plane of the material surface [27, 4]. For larger beam diameters thermal diffusion is significant and must be included in the calculation of source directivity [36]. Forces due to the expansion and contraction of the material in

the surface normal direction can be neglected because of the assumed aspect ratio of the heated region [56]. The amplitude of the generated elastic waves are dependent on angle to the surface normal, θ. These dependency of the amplitude of a wave as a function of angle is called the directivity pattern. The directivity patterns for longitudinal and shear waves generated by a thermoelastic laser source are given in Eqs. 31 and 32 and presented graphically in Figure 10 [52].

$$u_L \propto \frac{\sin\theta \sin 2\theta \sqrt{\kappa^2 - \sin^2\theta}}{(\kappa^2 - 2\sin^2\theta)^2 + 4\sin^2\theta\sqrt{1-\sin^2\theta}\sqrt{\kappa^2-\sin^2\theta}} \tag{31}$$

$$u_T \propto \frac{\kappa \sin 4\theta}{\kappa(1 - 2\sin^2\theta)^2 + 4\sin^2\theta\sqrt{1-\sin^2\theta}\sqrt{\kappa^2-\sin^2\theta}} \tag{32}$$

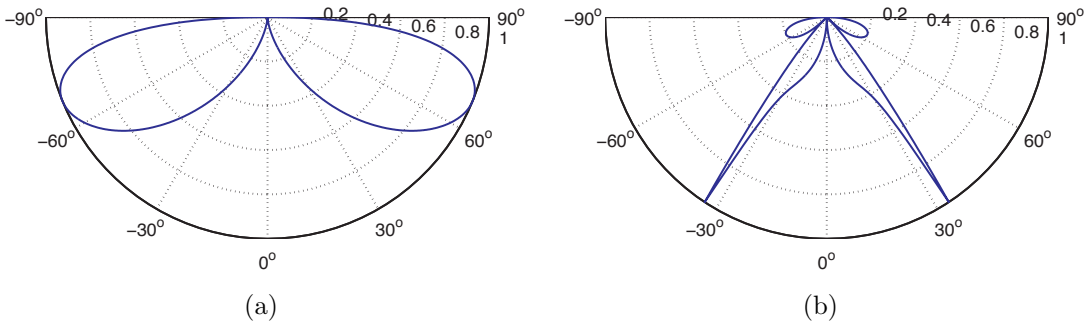

Figure 10: (a) Longitudinal and (b) shear directivity patterns for thermoelastic generation of ultrasound

2.3.2 Transition Generation

When the incident laser power is less than that required for ablation and greater than purely thermoelastic levels, ultrasound is produced by what is called transition generation. In the transition regime, the temperature of the material exceeds the melting temperature, but is less than the vaporization temperature. Transition generation can cause some damage caused by the melting and re-solidification of the surface and is not commonly used in the literature.

2.3.3 Ablative Generation

Ablative generation is achieved when the power density of the incident laser light is high enough to ablate a small portion of the heated material. For steel, power densities greater than $\sim 10^7$ W/cm^2 produce appreciable ablation [56]. Ablation is the removal of a thin layer of the surface of the material. The rapid increase in temperature at the surface causes the material to be vaporized and ionized, producing a plasma. The rapidly expanding plasma exerts a reaction pressure acting normal onto the surface. Ablative generation results in ultrasound with a much larger amplitude than that generated in the thermoelastic regime. In addition, the directivity patterns for longitudinal and shear waves are very different. The directivity patterns for longitudinal and shear waves are defined in Eqs. 33 and 34 and presented in Figure 11 [56].

$$u_L \propto \frac{2\kappa^2 \cos\theta(\kappa^2 - 2\sin^2\theta)}{(\kappa^2 - 2\sin^2\theta)^2 + 4\sin^2\theta\sqrt{1-\sin^2\theta}\sqrt{\kappa^2-\sin^2\theta}} \tag{33}$$

$$u_T \propto \frac{\sin 2\theta\sqrt{1-\kappa^2\sin^2\theta}}{\kappa(1 - 2\sin^2\theta)^2 + 4\sin^2\theta\sqrt{1-\sin^2\theta}\sqrt{\kappa^2-\sin^2\theta}} \tag{34}$$

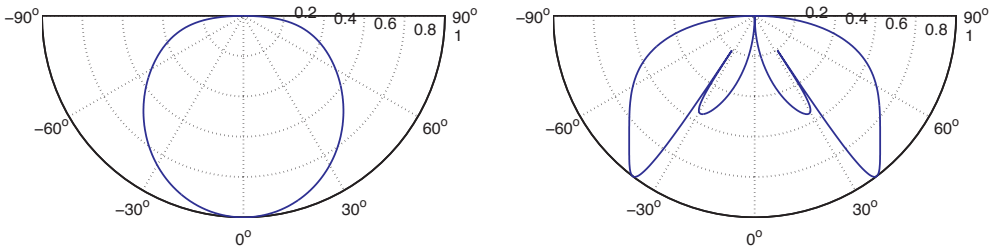

(a) (b)

Figure 11: (a) Longitudinal and (b) shear directivity patterns for ablative generation of ultrasound

2.4 EMAT Reception

When a non-contact means of detecting ultrasound is required, many devices can be used. Laser interferometers, air-coupled piezoelectric transducers, and electromagnetic transducers (EMATs) are all suitable for non-contact measurement. Laser interferometers require a smooth, reflective surface for operation. Air-coupled piezoelectric transducers are susceptible to noise from the welding arc. EMATs are less susceptible to surface variations but are susceptible to electromagnetic interference.

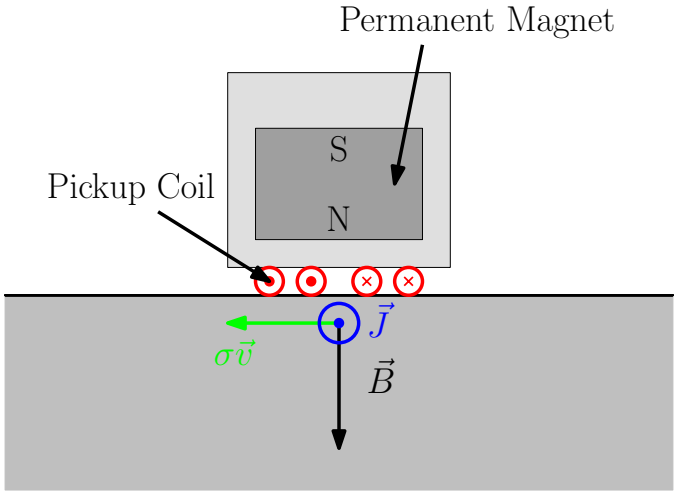

Figure 12: Lorentz force based EMAT reception

EMATs function through the detection interaction of magnetic fields and an electrically conductive material via either the magnetostrictive or Lorentz force mechanisms. Magnetostrictive EMATs are typically used only when the sample has a significant oxide scale layer on the surface. Lorentz EMATs receive ultrasound by creating and detecting eddy currents within the sample. As the material with conductivity σ vibrates with velocity v within the magnetic field created by the permanent magnet B, eddy currents J are created as described by Eq. 35.

$$\vec{J} = \sigma\vec{v} \times \vec{B} \tag{35}$$

These eddy currents induce currents in the pickup coil. The voltage across the coil is

amplified by a preamp allowing for measurement of material velocity at the surface of the sample. Because of the nature of the induction of the currents, EMATs are particularly sensitive to liftoff, the distance from the surface to the coil.

The EMAT used in this research is configured to measure shear-vertical ultrasonic waves propagating towards the surface at angles close to the normal. A permanent magnet, pickup coil and preamp are internal to the EMAT. Figure 12 presents a schematic of the EMAT used in this research. Here, a permanent magnet creates a vertical magnetic field normal to the surface and the pickup coil is wound such that the effective portion of the coil's wires run into and out of the page. The magnitude of the eddy current and therefore voltage signal produced by the EMAT will vary with incident angle. The directivity of the SV EMAT is greatly dependent on magnet and coil geometry and placement. The EMAT used in this research performs best when a shear wave is incident at an angle close to the surface normal ($\theta \approx 0^o$). In addition to SV waves, the EMAT can also be used to receive Rayleigh and Lamb waves.

2.5 Time of Flight Diffraction Penetration Depth Measurement Technique

The diffraction phenomena is commonly used to measure weld penetration depth using one of two transducer configurations. The first configuration, called pulse-echo, uses one transducer as shown in Figure 13(a). The transducer emits a wave that is directed towards the weld bead. The wave is diffracted by crack like defects and is received by the transducer. The times of flight of the various paths that the sound follows can be related to defect location and size. This technique is primarily used by technicians who place the transducers manually. Alternatively, two transducers can be used as shown in Figure 13(b) in a pitch-catch configuration. This configuration is used in the Time of Flight Diffraction (ToFD) technique [9]. In this technique, the ultrasound is directed at the crack by the transmitting transducer. The wave diffracts at the crack tip and the diffracted wave is received by the receiving transducer. In

addition to piezoelectric transducers as shown in Figure 13, EMATs and laser based transducer have been used [22, 42, 46]. The time of flight diffraction technique can be used to measure weld penetration depth and size other defects such as lack of fusion. Careful consideration must be paid to the placement of the transducers.

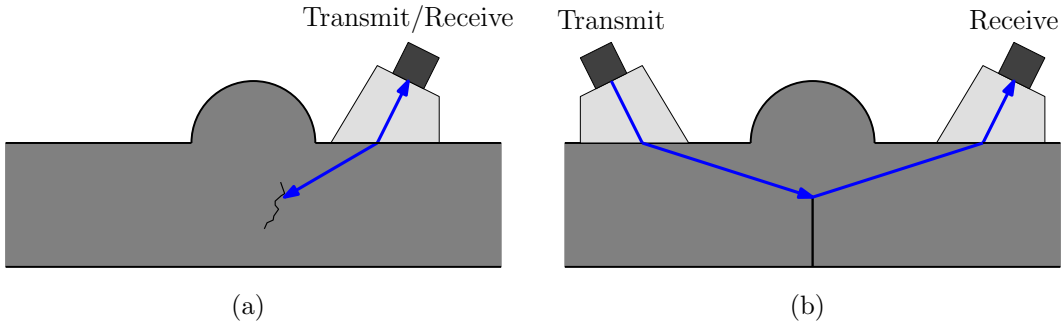

Figure 13: (a) Pulse-echo and (b) pitch-catch transducer configurations for ultrasonic weld inspection

2.6 RGLS Penetration Depth Measurement Technique

The Rayleigh Generation Longitudinal to Shear (RGLS) penetration depth measurement technique relates the time of flight the RGLS wave path to the weld penetration depth [32]. As its name suggests, this wave path involves multiple wave propagation modes. As shown in Figure 14, the RGLS wave is composed of paths on the generation and reception sides of the weld. The generation side consists of a bulk wave that undergoes mode conversion to a Rayleigh wave which travels along the bottom surface and crack between the two welded pieces. The reception side consists of a longitudinal to shear mode conversion which is received on the top surface.

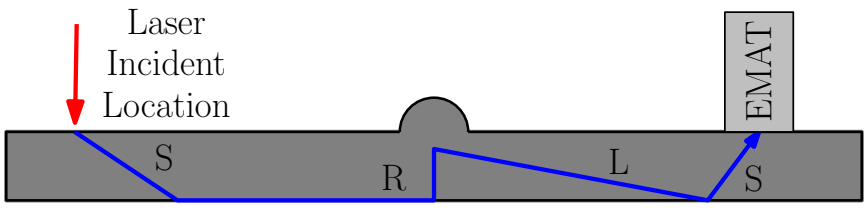

Figure 14: RGLS wave path

The time of flight of the RGLS wave, ToF_{RGLS}, is given in Eq. 36.

$$ToF_{RGLS} = \frac{T}{C_T \cos\theta_{RG}} + \frac{D_{SW} + T - PD - T\tan\theta_{RG}}{C_R} + \frac{T - PD}{C_L \cos\theta_L} + \frac{T}{C_T \cos\theta_T} \quad (36)$$

Where:

T: Plate thickness

θ_{RG}: Rayleigh generation angle

C_L, C_T: Longitudinal, shear wave speeds

C_R: Rayleigh wave speed

D_{SW}: Distance from laser incident location to weld

PD: Weld penetration depth

θ_L, θ_T: Angles for longitudinal to transverse mode conversion

In order for the wave to reach the receiver, the angles for the mode conversion, θ_L & θ_T, must satisfy Eqs. 15 and 37.

$$D_{WR} = T\tan\theta_T + (T - PD)\tan\theta_L \quad (37)$$

Where:

D_{WR}: Distance from weld to receiver

In Eq. 36, above, the Rayleigh generation angle, θ_{RG}, is assumed to be the mean of two angles, θ_{GL} and θ_{GT} as defined below.

$$\theta_{GL} = \arcsin\frac{C_R}{C_L} \quad (38)$$

$$\theta_{GT} = \arcsin\frac{C_R}{C_T} \quad (39)$$

$$(40)$$

Although the performance of the technique was very good, the fore-mentioned assumption was neither explained nor justified. This leaves a question regarding the mechanism through which the Rayleigh wave is generated via mode conversion of laser generated bulk waves.

CHAPTER III

IN-PROCESS WELD CONTROL AND INSPECTION SYSTEM

A system was developed in order to accomplish the goals of this research and to permit in-process weld penetration depth measurement. Previous systems in the Laser Ultrasonic Research Lab have been restricted to measuring weld penetration depth at a single location during or after welding. This research requires inspecting the sample at a fixed distance behind the welding torch as welding occurs. In addition, the industrial robotic welding system used in previous research is unable to vary welding parameters throughout the welding process. Since the in-process measurement is intended to be used for real time control, the robot must be capable of welding with time varying parameters. To this end, a microcontroller was configured to interface with the welder and positioning device. A schematic of the system is shown below in Figure 15. In the above system, the welding torch and sensing system are stationary while the welding sample moves. This configuration ensures accurate torch placement throughout the weld and eliminates the need for an industrial welding robot. The system was designed to weld two mild steel plates in butt weld configuration. A laser is incident on one piece and an Electromagnetic Acoustic Transducer (EMAT) is located opposite the weld on the other piece. A computer receives and interprets the ultrasound. The components of the system are now described.

3.1 LURL EMAT (Kita)

The LURL EMAT was designed for the purpose of receiving ultrasound in high temperature environments. The EMAT consists of a coil that is connected to a differential

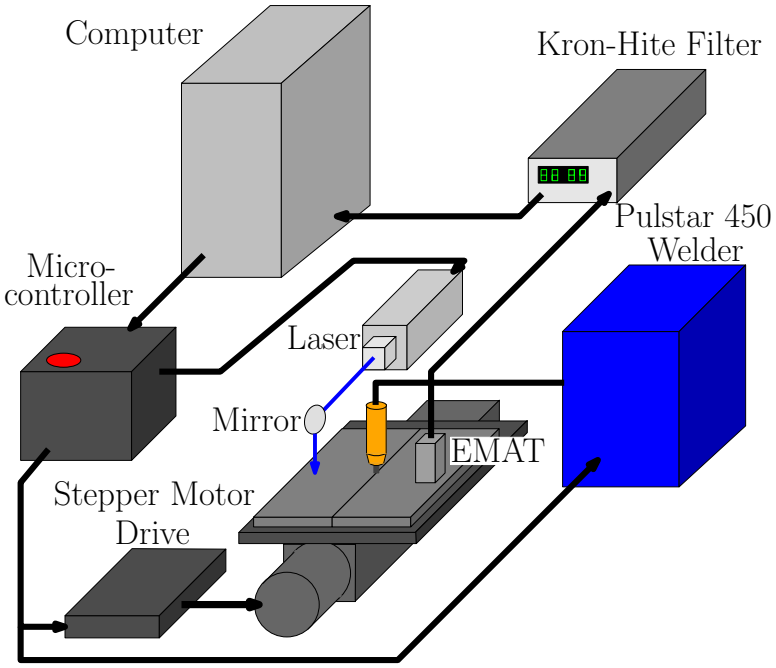

Figure 15: Schematic of experimental system

amplifier housed inside the body of the EMAT and a battery. The coil is wound in a racetrack configuration out of 44 gauge enameled magnet wire. The coil has a 30 Ω resistance and dimensions 4 by 14 mm. The housing measures 1.5 (0.032m) x 1.5 (0.032m) x 4 (0.102m). The EMAT has been shown to have excellent bandwidth and signal-to-noise ratio when the case is carefully grounded to the sample. In order to reduce the effects of noise due to the welding arc and provide a consistent ground connection, a grounding yoke was designed and built. The purpose of the yoke is to provide an electrical connection between the housing of the EMAT and the sample. The yoke uses a flexible electromagnetic interference (EMI) gasket from Spira Manufacturing Corporation. The gasket consists of a metal coil wrapped around a flexible plastic tube. The gasket provides a compliant electrical connection and helps shield the coil and preamp from EMI caused by the welding arc. The EMAT and yoke are shown in Figure 16.

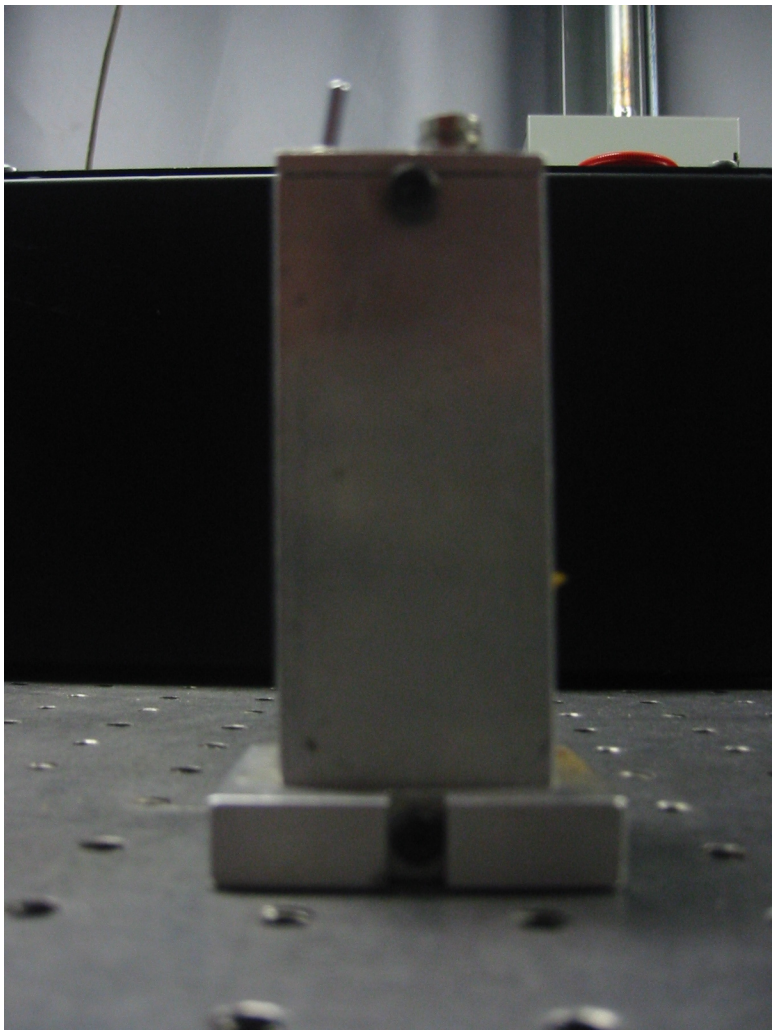

Figure 16: LURL EMAT with grounding yoke installed

3.2 Filter/Amplifier

A Kron-Hite model 3945 filter is used to amplify and filter the signal to remove unwanted electrical noise introduced by the welding process. The filter is configured as a Bessel band-pass filter with a pass band of 0.1 to 5.0 MHz in order to prevent aliasing and reduce low frequency noise. A Bessel filter is used because of its maximally flat group delay in the pass band.

Figure 17: Krohn-Hite model 3945 filter

3.3 Laser

The laser used is a Laser Photonics Nd:Yag with 1064 nm wavelength. It has an external sync feature that permits laser firing to be controlled by a TTL signal generated by the microcontroller.

Repetition Rate:	20 pulses/sec
Energy:	2 mJ/pulse maximum
Pulsewidth:	8-10 ns
Divergence:	0.6 mrads
Energy Stability:	0.5 %
Power Drift:	3%

3.4 Laser Trigger

A new trigger was implemented that has been shown to be insensitive to light from the welding arc but has a large sensitivity to the light emitted by the laser. The sensor is a NTE3032 phototransistor designed to be sensitive to light in the near infrared band (0.75-1.4 μm wavelength). The collector is connected to Channel A of the data acquisition card and the emitter is connected to ground. The trigger is placed so that one output of a beamsplitter is incident on the photodiode. The beamsplitter is configured to direct approximately 1% of the incident laser energy to the photodiode. This causes minimal reduction of the laser energy that reaches the part surface, yet provides a consistent means to trigger data acquisition.

3.5 Welder

A Miller Pulstar 450 gas metal arc welder was used to weld specimens. The welder has an interface for remote control of the welding parameters and actions (such as start/stop and gas flow). Two 24 V digital signals control shielding gas flow and the welding arc. Two analog signals determine the arc voltage and wire feed rate during welding. The arc voltage analog command signal ranges from 0-10 V and corresponds to 0-50 V arc voltage. The wire feed rate analog command signal ranges from 0-8 V and corresponds to 0-800 in/min (0-33.9 cm/s) wire feed rate.

3.6 Data Acquisition System

A Gage Compuscope 8349 PCI A/D card is used to digitize and capture signals created by the laser trigger and EMAT. The card is installed on a dual core Xenon based computer system. The card has the following specifications:

Channels:	4
Amplitude Resolution:	14 bit
Gain settings:	100 mV, 200 mV, 500 mV, 1 V, 2 V, 5 V

Input Impedance: 50 Ω or 1MΩ

Maximum sample rate: 125 Mhz (8 ns time resolution)

Onboard memory: 128 MSamples

3.7 User Interface and Data Acquisition Program

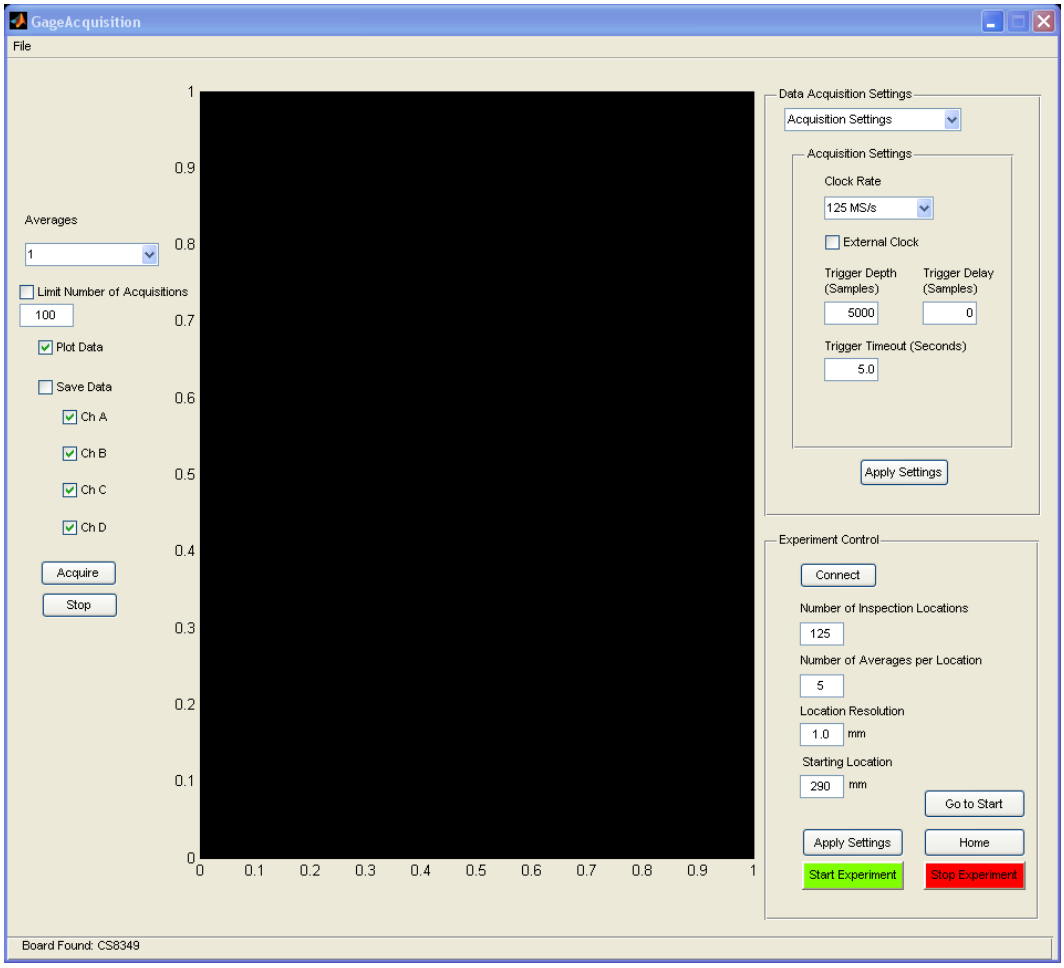

Figure 18: Graphical User Interface for MATLAB data acquisition and experiment control program

A Matlab program was developed to allow the user to control the experiment. The user defines the parameters of the data acquisition (gain, sample rate, trigger settings, etc.) and inspection (number of averages per location, etc.) via a Graphical User

Interface (GUI). The program is capable of acquiring and storing digitized signals at a 125 Mhz sample rate. Since the program is developed in MATLAB, signal processing tools can be integrated directly into the application. In addition to data acquisition, the program is capable of communicating with the microcontroller module in order to relay user commands. The microcontroller module is described in the next section.

3.8 Microcontroller Module

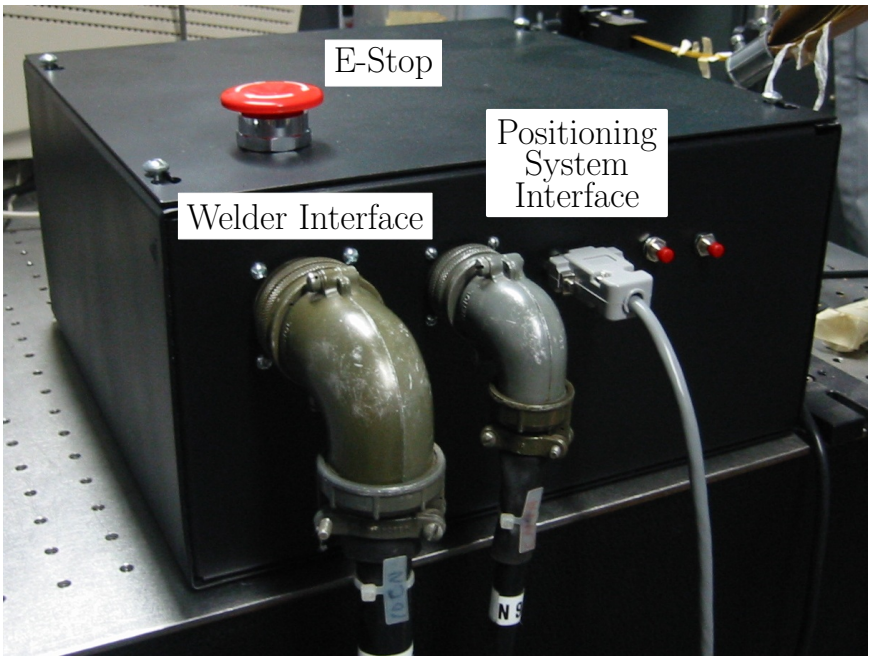

Figure 19: Microcontroller module

A microcontroller module was designed and built to interface with equipment and to ensure the process is controlled at a consistent rat. The module is shown in Figure 19. At the heart of the module is a Freescale Semiconductor 68HC11E9 microprocessor operating at a system clock rate of 2 MHz. The microcontroller controls the automatic aspects of the experiment. It communicates with the welder by means of the digital and analog signals already mentioned. Communication to a PC is performed through a RS-232 interface. Custom circuitry was designed and created in order to interface with the other components of the system. An Analog Devices

AD7327 dual 12-bit Digital to Analog Converter (DAC) is addressed on the HC11 address bus and used to generate 0-8 V and 0-10 V analog control signals sent to the welder. MOSFETs are used to switch the 24V signals to control shielding gas flow and to initiate the welding arc. A 5 V digital signal is connected to the external sync port on the laser to control laser firing. Finally, the microcontroller controls the motion of the positioning stage by sending step and direction commands to the stepper motor drive.

3.9 Positioning System

In traditional welding practice, the welding torch moves along the weld seam. Modern welding robots are capable of moving the torch along complex paths in multiple degrees of freedom. The relatively simple weld geometry considered in this research does not require complex motion. In addition, the sensing system used in this research must follow the welding torch at a fixed distance. In order to ensure accurate and consistent positioning of the sensing system relative to the torch and weld seam, the torch, EMAT and optics were held fixed. The work pieces were placed on a table and moved underneath the torch and sensing system by a lead screw.

The lead screw is a ball screw with 3.0 mm lead and is driven by a stepper motor. The motor used is an Oriental Motor 5-phase stepper motor with a resolution of 0.72 degrees per step. A five phase stepper motor is used because of its reduced vibration and increased angular resolution when compared to a two phase stepper motor. Given the lead of the ball screw, this corresponds to a linear resolution of 6 μm per step. Calibration of table position is achieved by means of an optical limit switch. Welding samples are placed on the table and located by means of dowel pins. This allows for repeatable placement of the samples. Repeatable placement reduces possible error in sample placement relative to the torch and sensing system. The welding torch and mirror are positioned using optical bench equipment. The EMAT is positioned

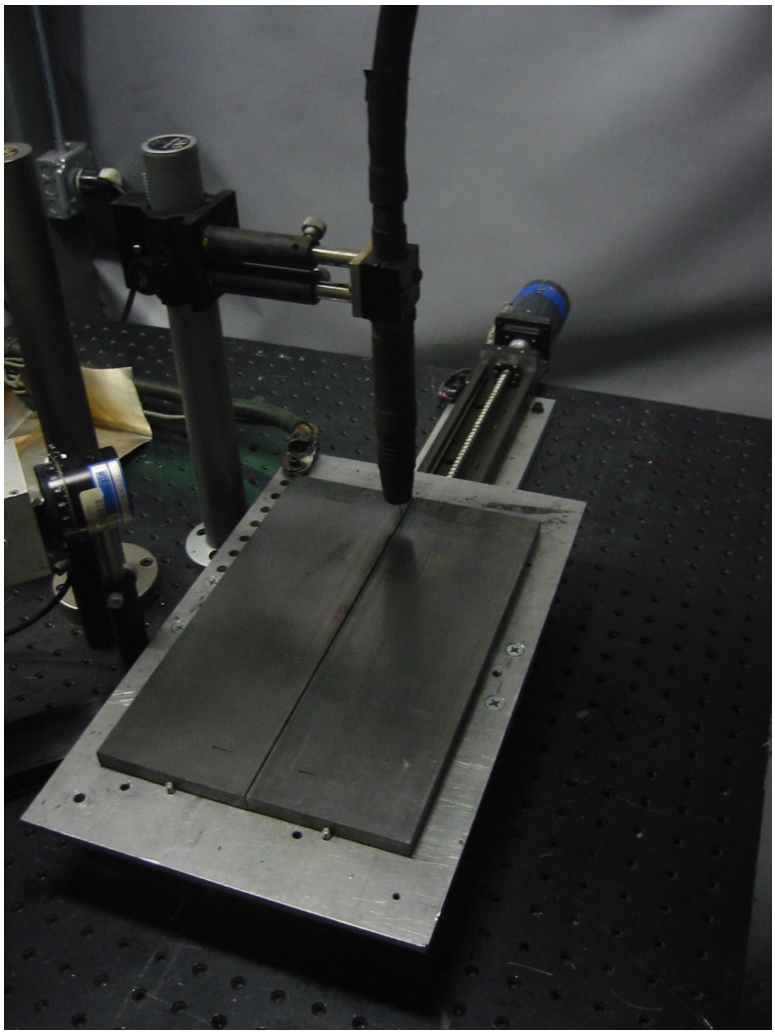

Figure 20: Positioning system

using a custom mount. The positioning system is shown in Figure 20 with EMAT and laser optics removed. From inspecting previous specimens welded using a 5-DOF robot, it is clear that torch positioning is of great importance. The flexibility of the robot resulted in error in torch position. If the torch is positioned incorrectly, the penetration depth will be greatly affected. The positioning system minimizes errors in torch positioning.

CHAPTER IV

RAYLEIGH WAVE PROPAGATION IN ELASTIC PLATES

The RGLS ToF weld penetration depth measurement technique has been used to accurately measure weld penetration depth. As described in Chapter II, the technique yields a penetration depth measurement by relating the measured time of flight to the path taken by the ultrasonic wave from the source to the receiver. The path used in the RGLS ToF technique involves propagation of bulk waves from the generation point to the bottom surface of the material. It was assumed that these bulk waves undergo mode conversion to a Rayleigh wave that propagates along the bottom surface of the plate to the weld seam, travels up the crack and is diffracted at the root of the weld. This assumption was not verified. Gaining a more complete understanding of the processes involved permits determining the limitations of the technique and optimization of the system configuration for a given sample and weld geometry. To this end, the propagation of Rayleigh waves traveling in plates was studied experimentally and via numerical simulation.

4.1 Experimental Measurement of Rayleigh Waves

In order to determine the source and nature of the Rayleigh wave that travels on the bottom surface of an elastic plate, an experiment was performed. Acoustic waves were generated on the top surface of a plate and received on the bottom surface at varying distances from the source. Two plates were used, with thicknesses equal to 12.6 and 25.4 mm. A Nd:YAG laser was configured to emit 60 mJ of energy per pulse and generate ultrasound via ablation. The laser head was placed on a platform attached to an automated linear positioning system. The system was configured to direct the laser at the top surface of the plate at distances 0 to 90 mm in 0.5 mm

increments for the 12.6 mm thick plate and 0 to 180 mm in 1.0 mm increments for the 25.4 mm thick plate. A Polytec OFV-534 laser interferometer sensor head with OFV-2570 controller (bandwidth 30 kHz to 24 MHz) and the custom built LURL EMAT (bandwidth 100 kHz to 3 MHz) were placed on the bottom surface to receive the ultrasound generated by the laser. For each measurement location, the laser was fired 64 times and the acquired signals were averaged to increase the signal to noise ratio. A schematic of the experimental setup is shown in Figure 21 and a photograph of the setup is shown in Figure 22.

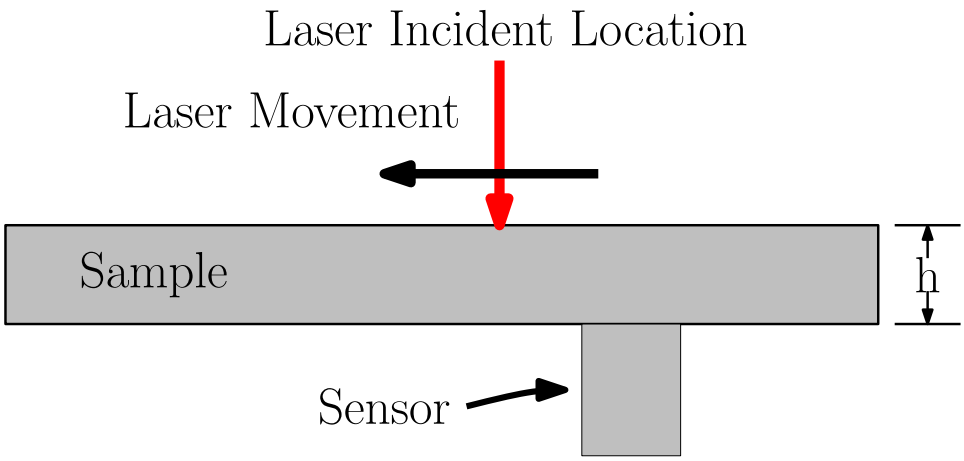

Figure 21: Experimental setup for measurement of Rayleigh waves

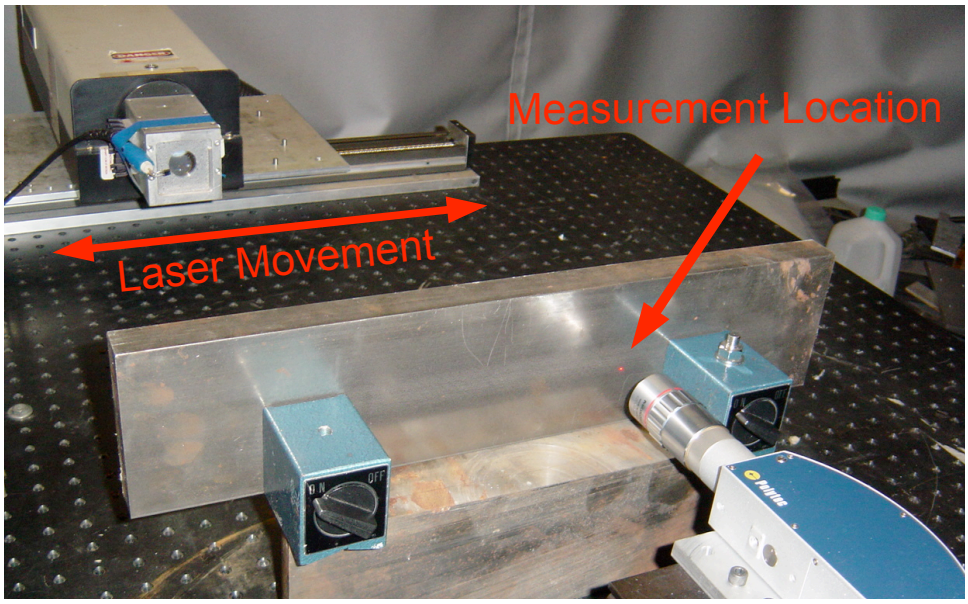

Figure 22: Image of Experimental Setup

Signals recorded by the interferometer and the EMAT at the radial distance 60 mm in the 12.6 mm plate are shown below in Figure 23. Some of the many bulk waves that reach the sensor are indicated by labels where L indicates longitudinal, T shear, H head, and R Rayleigh waves. In addition, there is a low frequency component of the signal present from 18 to 22 μs. This is the Rayleigh wave traveling along the bottom surface.

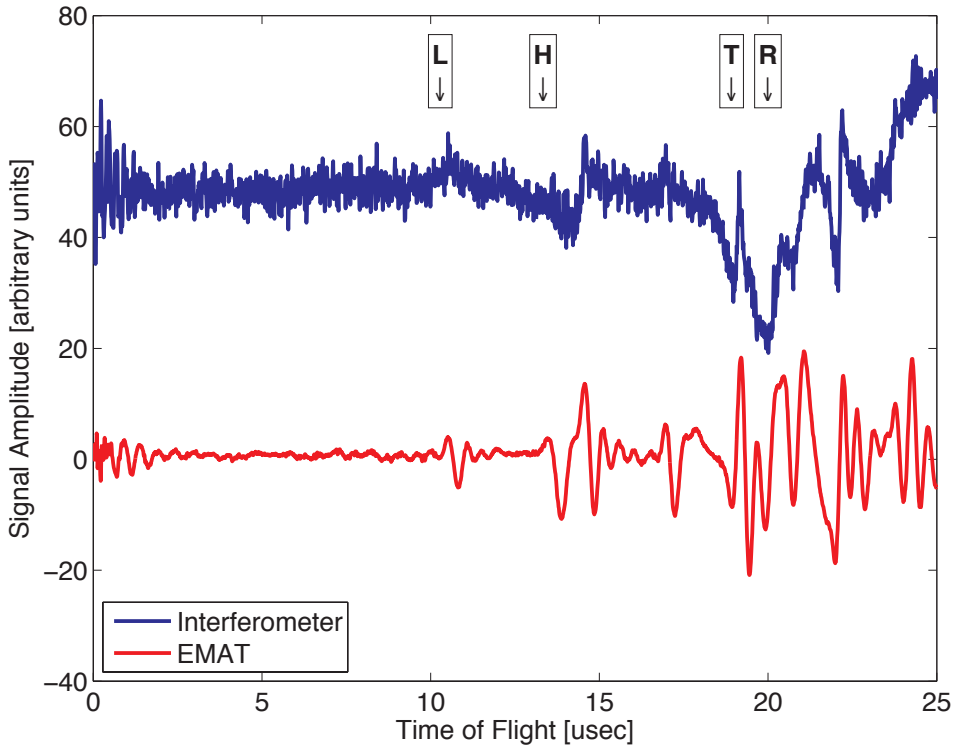

Figure 23: Signals received by the interferometer and EMAT at 60 mm radial distance (signals are scaled for presentation)

In order to identify the location where the Rayleigh wave is first present on the bottom of the plate, the averaged signals were compiled into scans. In the scans, the abscissa corresponds to time of flight and the ordinate corresponds to radial distance from the laser source to the receiver. The amplitude of the signal is represented by the grayscale value as shown in the color bar. The theoretical ToFs for the direct longitudinal, shear, and head waves were determined by Eqs. 41 - 43, where r is the radial distance from the source to the receiver and h is the thickness of the plate.

The signals recorded by the interferometer and the EMAT are shown in Figures 24 and 25.

$$ToF_L = \frac{\sqrt{r^2 + h^2}}{C_L} \tag{41}$$

$$ToF_T = \frac{\sqrt{r^2 + h^2}}{C_T} \tag{42}$$

$$ToF_H = \frac{r}{C_L} + \frac{h}{C_L \tan(\sin^{-1} \frac{C_T}{C_L})} \tag{43}$$

Within the ellipse in the figures, the Rayleigh wave is seen at large radial distances from the laser source. The frequency content of this wave is much lower; it appears more like a rolling ridge in the scan as opposed to the sharper ridges corresponding to the direct bulk waves. The amplitude of the ridge received on the 25.4 mm plate is less than that received on the 12.6 mm plate. The ridge is not clearly visible in the signals received by the EMAT on the 25.4 mm plate.

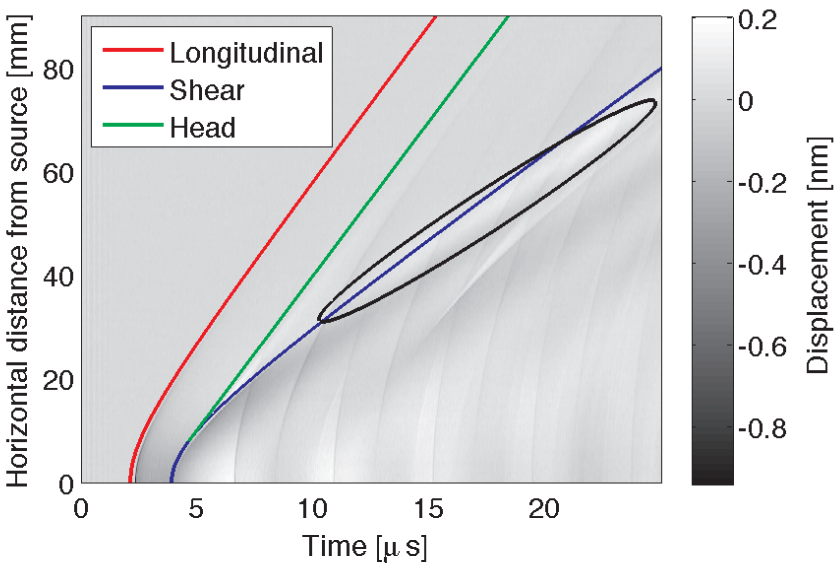

(a)

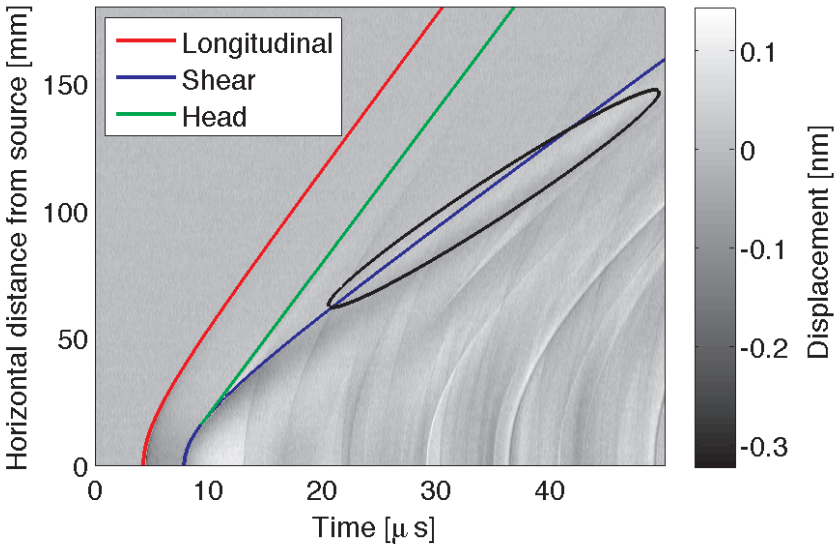

(b)

Figure 24: Displacements received by laser interferometer for (a) 12.6 mm and (b) 25.4 mm thick steel plates. Red, green and blue lines denote longitudinal, head, and shear wave theoretical ToF, respectively.

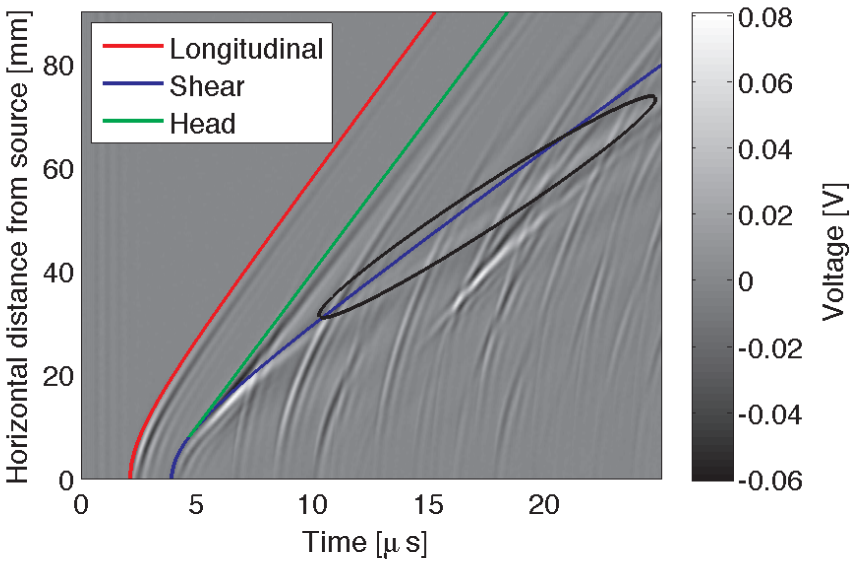

(a)

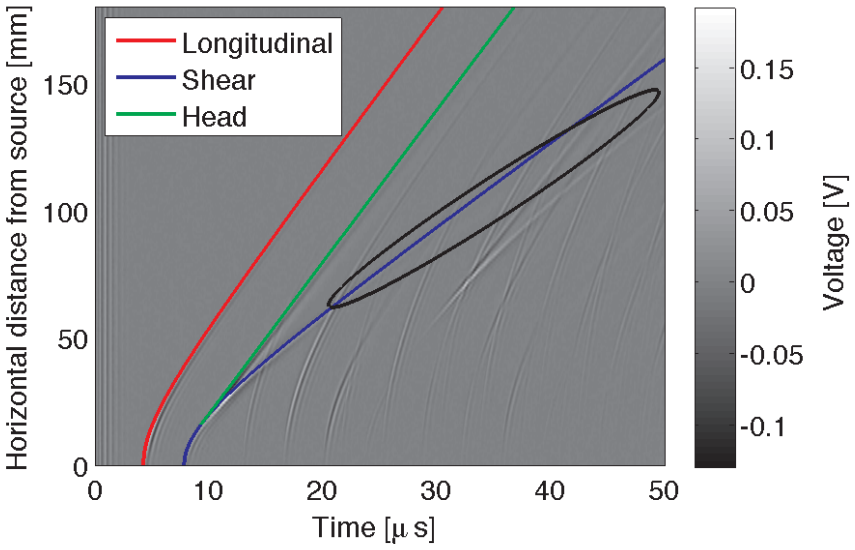

(b)

Figure 25: Signals received by LURL EMAT for (a) 12.6 mm and (b) 25.4 mm thick steel plates. Red, green and blue lines denote longitudinal, head, and shear wave theoretical ToF, respectively.

In order to more easily visualize the Rayleigh wave, new scans were created by plotting the signals not with respect to time of flight but to the parameter τ as defined in Eq. 44 where r is the radial distance from the source to the receiver.

$$\tau = t - \frac{r}{C_R} \tag{44}$$

This parameter is the difference in time of flight and the Rayleigh time of flight. When the signals are plotted with respect to τ, any waves that travel at the Rayleigh speed will be seen as vertical ridges in the figure. The resulting scans for the 12.6 and 25.4 mm thick plates are shown in Figures 26 and 27.

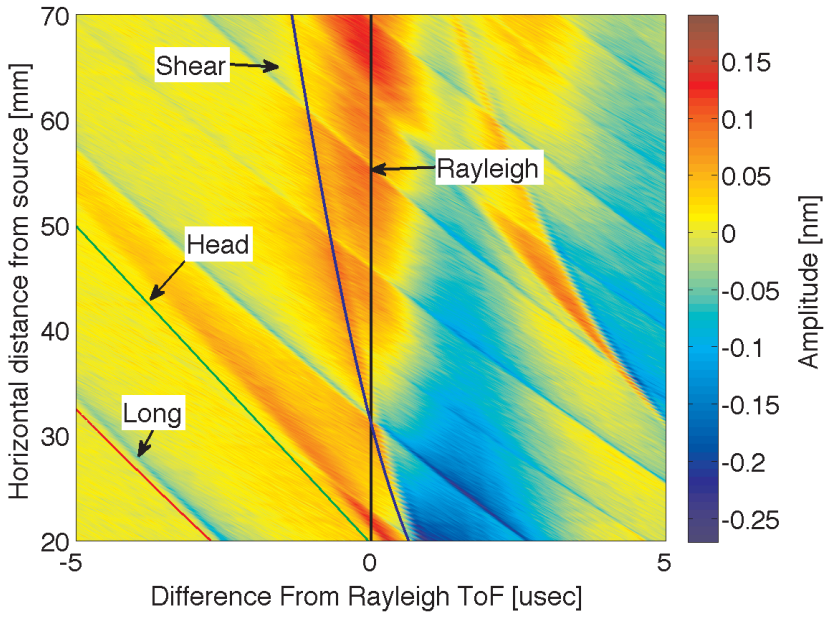

Figure 26: Displacements received by laser interferometer for 12.6 mm thick steel plate plotted with respect to τ

The low frequency ridge present in the signals is vertical, centered about $\tau = 0$. This indicates the wave travels at the Rayleigh wave velocity. For the thicker plate, the width of the ridge is approximately 2 μs and for the 12.6 mm thick plate the width is approximately 1 μs. This indicates the frequency content of the wave is dependent on plate thickness. The ridge arrives after the shear wave and is only

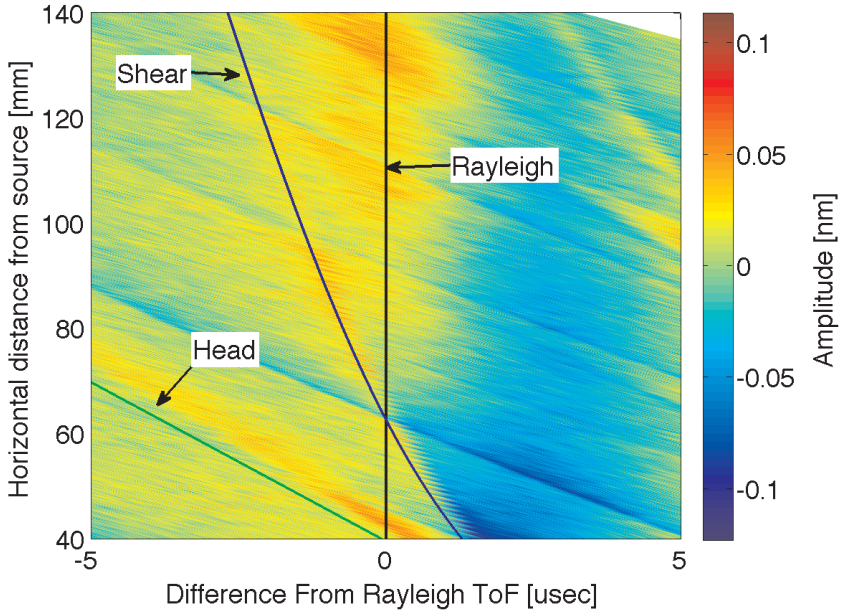

Figure 27: Displacements received by laser interferometer for 25.4 mm thick steel plate plotted with respect to τ

present at horizontal distances greater than a critical distance. This critical distance is the distance where the shear and Rayleigh ToFs are equal. This corresponds to the intersection of the shear and Rayleigh times of flight in Figures 26 and 27. The critical distance is given by Eq. 45.

$$r_{crit} = \frac{C_R h}{\sqrt{C_T^2 - C_R^2}} \tag{45}$$

For the 12.6 mm thick plate, the critical distance is 31.3 mm and for the 24.5 mm thick plate, the critical distance is 63.1 mm. Previous research assumed the interaction of the longitudinal and shear waves resulted in mode conversion to a Rayleigh wave. The wave was assumed to be created on the bottom surface of the plate at a location called D_{RG} given by Eq. 46. This location is where a shear wave traveling at angle θ_{RG} (defined in Eq. 47) reaches the bottom of the plate as shown in Figure 28.

$$D_{RG} = \frac{h}{\tan\theta_{RG}} \tag{46}$$

$$\theta_{RG} = \frac{1}{2}\left(\sin^{-1}\left(\frac{C_R}{C_T}\right) + \sin^{-1}\left(\frac{C_R}{C_L}\right)\right) \tag{47}$$

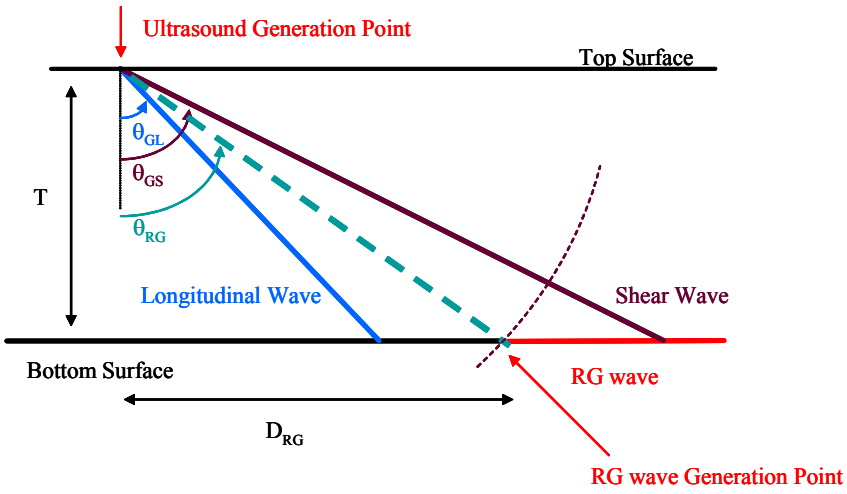

Figure 28: Assumed generation location according to previous research [33]

For the 12.6 and 25.4 mm plates, the corresponding D_{RG}'s are 10.9 and 22.0 mm, respectively. No wave that travels at the Rayleigh speed is present in the recorded signals at these source to receiver distances. This suggests the aforementioned assumption is incorrect. The result of making this assumption is a constant error in time of flight for any penetration depth. Using this assumption, the expected time of flight is longer because of the larger distance traveled by the Rayleigh wave. In the previous work, the ToF is measured by finding the local minima of the recorded signal. It is possible that the calibration of the time of flight measurement may have been done in error. Therefore, this error in ToF measurement may have been compensated by the incorrect assumption.

The aforementioned assumption that the wave is the result of mode conversion of bulk waves was not proven in earlier works. Interestingly, the Rayleigh wave on the bottom surface of the plate has the same time of flight as the Rayleigh wave on the

top surface. There are two possible explanations for this. First, the wave is the result of mode conversion of a shear wave that travels at an angle at which the horizontal component of the wave velocity vector is equal to the Rayleigh speed and reaches the bottom surface at r_{crit}. Secondly, the wave may actually be the same Rayleigh wave that travels along the top surface. It is well understood that the shear wavefront expands hemispherically while the Rayleigh wavefront expands radially outward from the source. However, the Rayleigh wave will extend some distance below the top surface of the plate, resulting in a cylindrical wavefront as shown in Figure 29.

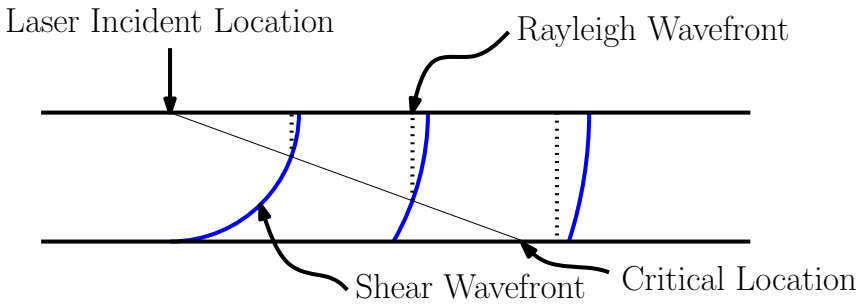

Figure 29: Expansion of Shear and Rayleigh Wavefronts

The amplitude of a Rayleigh wave decreases distance below the surface increases. The rate at which the amplitude decreases is dependent on the wavelength of the wave. Since laser generated ultrasound is broadband, the generated Rayleigh wave will have both low and high frequency components (corresponding to long and short wavelengths). Because the amplitude decay of the Rayleigh wave is dependent on wavelength, the frequency content of Rayleigh wave varies with depth, i.e. at larger distances below the surface, the high frequency components should be attenuated more than the low frequency components. In order to choose the optimal receiver for this wave, it is necessary to match the dominant frequency of the wave with the center frequency of the transducer. A model was developed that can show the mechanism through which the Rayleigh wave reaches the bottom surface of the plate and can predict the Rayleigh wave dominant frequency.

4.2 Generalized Ray Theory

Generalized Ray Theory was developed in order to study the propagation of elastic waves in layered media such as the earth's crust. Pao and Gajewski applied the technique for use in acoustic emission of layered plates and wrote a thorough treatment on the subject [48]. Ceranoglu and Pao then continued the work and determined the response of plates due to a variety of force and moment sources [15, 16, 14]. While computationally intensive, the theory permits the computation of the displacement at a given location in the media as a summation of components from multiple generalized rays. The utility of the theory for this work is the ability to determine the response of the plate when only the direct ray is considered. Other simulation tools, such as finite element modeling, compute the total response with all reflections included. In this case, it would be difficult to directly analyze only the Rayleigh wave because of the interference of other waves. The principles and implementation of Generalized Ray Theory are now presented.

4.2.1 Theory

Consider a layer of elastic material. When stresses are applied at a location in the layer, elastic waves will propagate away from this location. The response of the material depends on material properties and the direction(s) and amplitude of the applied stresses as a function of time. Generalized ray theory formulates the solution of the displacement of the layer of the sum of the displacements of multiple rays, with each ray possibly being composed of multiple segments. Each ray is defined by the initial mode, the modes of the segment(s), and the final mode. Figure 30 shows multiple ray paths for the case when the source is within the layer and the receiver is located on the bottom surface. Three types of rays are shown, the direct ray (solid line), a ray with a single reflection (dotted line), and a ray that undergoes two reflections and mode conversion. Rays with many segments can reach the receiver

and all rays that reach the receiver within the time range considered must be included in the calculation.

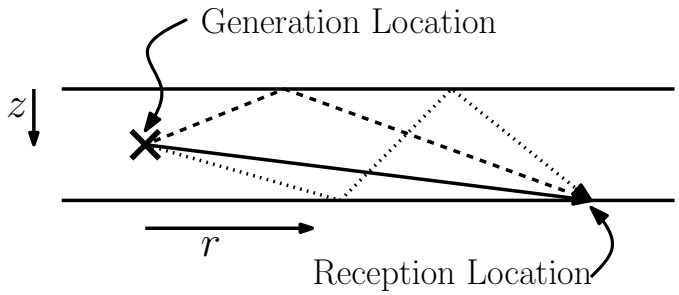

Figure 30: Possible ray paths showing the direct (solid), single reflection (dashed) and two reflections with mode conversion (dotted)

As detailed in [48], the response of the plate due to the acoustic source is obtained through the use of integral transforms and numerical integration. The formulation of the problem for the case of a point source is now outlined. Consider an elastic plate with known material constants. The wave equation defines the response of the material due to an applied acoustic source as given in Eq. 7.

Because of the axisymmetric nature of this problem, the cylindrical coordinate system shown in Figure 31 is used. The origin is located at the top surface of the plate coaxial with the source (when the source is located on the surface, the origin is coincident with the source) and the z-axis is normal to the surface, increasing downwards.

For axisymmetric cylindrical coordinates the wave equation may be written in terms of scalar potential ϕ and vector potential $\boldsymbol{\psi}$ (in bold). The potentials are functions of radial distance, r, distance below the top surface, z, and time, t. The potentials satisfy Eqs. 48 and 49.

$$\nabla^2\phi = \frac{1}{C_L^2}\ddot{\phi} \tag{48}$$

$$\nabla^2\boldsymbol{\psi} = \frac{1}{C_T^2}\ddot{\boldsymbol{\psi}} \tag{49}$$

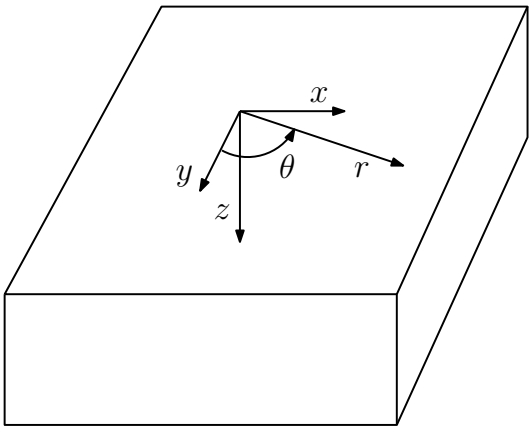

Figure 31: Cylindrical coordinate system used for generalized ray theory formulation

For cylindrical coordinates, the Laplacian ∇^2 is given as Eq. 50

$$\nabla^2 = \frac{1}{r^2}\frac{\partial}{\partial r} + \frac{\partial^2}{\partial r^2} + \frac{1}{r^2}\frac{\partial^2}{\partial \theta^2} + \frac{\partial^2}{\partial z^2} \tag{50}$$

Following the notation in [48], the vector potential $\boldsymbol{\psi}$ can be formulated in terms of two scalar potentials as shown in Eq. 51.

$$\boldsymbol{\psi} = \left(\frac{1}{r}\frac{\partial \psi}{\partial \theta}, -\frac{\partial \psi}{\partial r}, \chi\right) \tag{51}$$

Since the problem at hand is axisymmetric, the displacement and potentials are independent of coordinate θ. Therefore, $\chi = 0$ and only ψ is considered. Note that ψ satisfies the scalar wave equation in Eq. 52

$$\nabla^2 \psi = \frac{1}{C_T^2}\ddot{\psi} \tag{52}$$

Expanding Eq. 48 and 52 leads to the following equations:

$$\frac{\partial^2 \phi}{\partial r^2} + \frac{1}{r}\frac{\partial \phi}{\partial r} + \frac{\partial^2 \phi}{\partial z^2} = \frac{1}{C_L^2}\ddot{\phi} \tag{53}$$

$$\frac{\partial^2 \psi}{\partial r^2} + \frac{1}{r}\frac{\partial \psi}{\partial r} + \frac{\partial^2 \psi}{\partial z^2} = \frac{1}{C_T^2}\ddot{\psi} \tag{54}$$

The displacement and stress components are determined in terms of the scalar potentials as given in Eqs. 55-58.

$$u_z = \frac{\partial \phi}{\partial z} + \frac{\partial^2 \psi}{\partial z^2} - \frac{1}{C_T^2}\ddot{\psi} \tag{55}$$

$$u_r = \frac{\partial \phi}{\partial r} + \frac{\partial^2 \psi}{\partial r \partial z} \tag{56}$$

$$\sigma_{zz} = \frac{\lambda}{C_L^2}\frac{\partial^2 \phi}{\partial t^2} + 2\mu \frac{\partial}{\partial z}\left(\frac{\partial \phi}{\partial z} + \frac{\partial^2 \psi}{\partial z^2} + \frac{1}{C_T^2}\frac{\partial^2 \psi}{\partial t^2}\right) \tag{57}$$

$$\sigma_{zr} = \mu\left(2\frac{\partial^2 \phi}{\partial r \partial z} + 2\frac{\partial^3 \psi}{\partial r \partial z^2} - \frac{1}{C_T^2}\frac{\partial^3 \psi}{\partial r \partial t^2}\right) \tag{58}$$

The crux of the formulation of the solution is to apply integral transform techniques to reduce the complexity of the above equations. First, the Laplace transform is performed with respect to time. The Laplace transform of a variable is denoted by a bar above the symbols. The Laplace transforms of Eqs. 53 and 54 are shown in Eqs. 59 and 60.

$$\frac{\partial^2 \bar{\phi}}{\partial r^2} + \frac{1}{r}\frac{\partial \bar{\phi}}{\partial r} + \frac{\partial^2 \bar{\phi}}{\partial z^2} = \frac{s^2}{C_L^2}\bar{\phi} \tag{59}$$

$$\frac{\partial^2 \bar{\psi}}{\partial r^2} + \frac{1}{r}\frac{\partial \bar{\psi}}{\partial r} + \frac{\partial^2 \bar{\psi}}{\partial z^2} = \frac{s^2}{C_T^2}\bar{\psi} \tag{60}$$

Next the zero-th order Hankel transforms are performed on Eqs. 59 and 60. The Hankel transform is used because of it's ability to reduce the sum of partial derivatives in Eqs. 59 and 60. The Hankel transform uses a Bessel function as the kernel for the transformation. The Hankel transform of order n of an already Laplace transformed function $\bar{g}(r, z, s)$ is defined below in Eq. 61 where $J_n(s\xi r)$ is the n-th order Bessel function of the first kind and the caret symbol designates the twice transformed quantity.

$$\hat{F}(\xi, z, s) = \int_0^\infty r\bar{g}(r, z, s) J_n(s\xi r) dr \tag{61}$$

The transform variable $s\xi$ is used for convenience. The inverse Hankel transform is given by Eq. 62.

$$\bar{g}(r,z,s) = s^2 \int_0^\infty \xi \hat{F}(\xi,z,s) J_n(s\xi r) d\xi \tag{62}$$

For the n-th order Hankel transform, the following identity proves useful.

$$\frac{\partial^2 g}{\partial r^2} + \frac{1}{r}\frac{\partial g}{\partial r} - \frac{n^2}{r^2} g = -s^2 \xi^2 \hat{g}(s\xi) \tag{63}$$

After applying the zeroth order Hankel transform to Eqs. 59 and 60 and using the identity in Eq. 63, the homogeneous wave equations are

$$\frac{\partial^2 \hat{\phi}}{\partial z^2} - s^2 \left(\xi^2 + \frac{1}{C_L^2} \right) \hat{\phi} = 0 \tag{64}$$

$$\frac{\partial^2 \hat{\psi}}{\partial z^2} - s^2 \left(\xi^2 + \frac{1}{C_T^2} \right) \hat{\psi} = 0 \tag{65}$$

The terms η and ζ are defined by Eqs. 66 and 67 to allow for a more compact representation.

$$\eta^2 = \xi^2 + \frac{1}{C_L^2} \tag{66}$$

$$\zeta^2 = \xi^2 + \frac{1}{C_T^2} \tag{67}$$

The procedure now continues by solving the above equations for the given boundary conditions. Once the boundary conditions are applied, the Laplace transforms of the potentials can be formulated by applying the inverse Hankel transform.

Consider the case of a source located at a depth $z = z_0$ in a plate. Following the generalized ray formulation developed by Pao, the Hankel-Laplace transformed potentials for one generalized ray are expressed as in Eqs. 68 and 69.

$$\hat{\phi}(\xi,z,s) = F(s) S(\xi) \pi(\xi) e^{-sh(\xi,z)} \tag{68}$$

$$\hat{\psi}(r,z,s) = F(s) S(\xi) \pi(\xi) e^{-sh(\xi,z)} \tag{69}$$

$$h(\xi, z) = z_p \left(\xi^2 + \frac{1}{C_L}^2 \right)^{1/2} + z_s \left(\xi^2 + \frac{1}{C_T}^2 \right)^{1/2} \tag{70}$$

where $F(s)$ is a function that includes the time dependency of the source, S is the source function, and $\pi(\xi)$ is the product of all reflection coefficients that occur in the path taken by the ray. The terms z_p and z_s are the z-component of the total distance travelled by the wave from the source to the receiver as longitudinal and shear waves, respectively. The source function is obtained by applying the appropriate loading and boundary conditions to the wave equation and constitutive equations. These functions are defined for applied normal forces and centers of expansion as in Table 1. The source function used in Eqs. 68 and 69 depends on the mode of the first segment of the ray in consideration. When the first mode is longitudinal, the function S_P for the appropriate source is used. When the first mode is shear, S_V is used.

Table 1: Source Functions [48]

Souce Type	$F(s)$	S_P	S_V
Buried Center of Expansion	$\frac{f(s)}{4\pi C_L^2 s}$	$\frac{1}{\eta}$	0
Buried Normal Force	$\frac{f(s)}{4\pi\rho s^2}$	$-\varepsilon$	$\frac{\xi}{\zeta}$
Surface Normal Force	$\frac{f(s)}{2\pi\mu s^2}$	$\frac{\xi^2+\zeta^2}{\Delta_r(\xi)}$	$-\frac{2\xi\eta}{\Delta_r(\xi)}$

When the wave encounters a free surface, it is reflected and mode conversion may occur. The reflection coefficients for a free surface are given in Eqs. 71 - 74 where the superscript indicates the incident and reflected modes (i.e., R^{PS} is the reflection coefficient for incident longitudinal and reflected shear waves). In these equations, ε is equal to +1 if the incident wave is traveling in the positive z direction and -1 if it

is traveling in the negative z direction.

$$R^{PP} = [4\eta\zeta\xi^2 + (\xi^2 + \zeta^2)^2]\Delta_r^{-1} \tag{71}$$

$$R^{PS} = 4\varepsilon\xi\eta(\xi^2 + \zeta^2)\Delta_r^{-1} \tag{72}$$

$$R^{SP} = 4\varepsilon\xi\zeta(\xi^2 + \zeta^2)\Delta_r^{-1} \tag{73}$$

$$R^{SS} = [4\eta\zeta\xi^2 + (\xi^2 + \zeta^2)^2]\Delta_r^{-1} \tag{74}$$

$$\Delta_r = 4\eta\zeta\xi^2 - (\xi^2 + \zeta^2)^2 \tag{75}$$

As an example, consider the ray shown in Figure 32 traveling in a plate of thickness h. In this case, the ray consists of three segments. The wave propagates as longitudinal, then shear, then longitudinal waves. In this case, z_p is twice the plate thickness $2h$, z_s is equal to the plate thickness h and $\pi(\xi)$ is equal to $R^{PS}R^{SP}$.

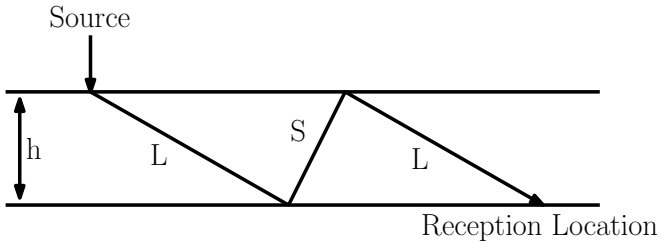

Figure 32: Example path for Longitudinal to Shear to Longitudinal ray

The displacement of the medium can be calculated from the potentials as shown in Eqs. 55 and 56. The formulation presented by Pao organizes the transformed displacements by multiplying the potentials in Eqs. 68 and 69 by $sD(\xi)$. The receiver functions for the z and r components of the displacement are shown in Table 2

$$\hat{u_z}(\xi, z, s) = s\bar{F}(s)S(\xi)\pi(\xi)D(\xi)e^{-sh(\xi,z)} \tag{76}$$

$$\hat{u_r}(\xi, z, s) = s\bar{F}(s)S(\xi)\pi(\xi)D(\xi)e^{-sh(\xi,z)} \tag{77}$$

In order to calculate the displacements due to a generalized ray at a given location (r, z) in the time domain, the inverse Hankel and Laplace transforms of the expressions

Table 2: Receiver Functions [48]

Received Quantity	D (P Wave)	D (SV Wave)
u_z	$-\varepsilon\eta$	$-\xi$
u_r	$-\xi$	$-\varepsilon\zeta$

in Eqs. 76 and 77 must be performed. The inverse Hankel transforms are given in Eqs. 78 and 79.

$$u_z(r,z,s) = s^3\bar{F}(s)\int_0^\infty S(\xi)\pi(\xi)D(\xi)e^{-sh(\xi,z)}J_0(s\xi r)\xi d\xi \tag{78}$$

$$u_r(r,z,s) = s^3\bar{F}(s)\int_0^\infty S(\xi)\pi(\xi)D(\xi)e^{-sh(\xi,z)}J_1(s\xi r)\xi d\xi \tag{79}$$

The portion of the above expressions that depend on ξ is separated from the rest into functions $\bar{I}_r(r,z,s)$ and $\bar{I}_z(r,z,s)$.

$$u_z(r,z,s) = s^3\bar{F}(s)\bar{I}_r(r,z,s) \tag{80}$$

$$u_r(r,z,s) = s^3\bar{F}(s)\bar{I}_z(r,z,s) \tag{81}$$

$$\bar{I}_r(r,z,s) = \int_0^\infty S(\xi)\pi(\xi)D(\xi)e^{-sh(\xi,z)}J_0(s\xi r)\xi d\xi \tag{82}$$

$$\bar{I}_z(r,z,s) = \int_0^\infty S(\xi)\pi(\xi)D(\xi)e^{-sh(\xi,z)}J_1(s\xi r)\xi d\xi \tag{83}$$

The bessel functions in these inverse transforms are now replaced by integral representations as defined in Eq. 84.

$$J_n(z) = \frac{i^{-n}}{\pi}\int_0^\pi e^{iz\cos\omega}\cos(n\omega)d\omega \tag{84}$$

$$= \frac{2}{\pi}i^{-n}Re\int_0^{\pi/2} e^{iz\cos\omega}\cos(n\omega)d\omega, n = 0,2,4,... \tag{85}$$

$$= \frac{2}{\pi}i^{-n+1}Im\int_0^{\pi/2} e^{iz\cos\omega}\cos(n\omega)d\omega, n = 1,3,5,... \tag{86}$$

After replacing the bessel functions with their integral representations, the Cagniard technique is performed. This technique uses a path of integration for ξ that permits determining the inverse Laplace transform by inspection. The path used is specified in Eq. 87.

$$-t = i\xi r\cos\omega - h(\xi, z) \tag{87}$$

After some manipulation, this results in the following integrals given in Eqs. 88 and 89. The upper limit of integration, $\xi_1(t)$, satisfies Eq. 90. The function K is defined as in Eq. 91.

$$I_r(r,z,t) = \frac{2}{\pi r} Im \int_0^{\xi_1(t)} \xi E_r(\xi) \frac{t - \sum z_j (\xi^2 + 1/C_j^2)^{1/2}}{K(\xi; r, z, t)} d\xi \tag{88}$$

$$I_z(r,z,t) = \frac{2}{\pi} Im \int_0^{\xi_1(t)} E_z(\xi) \frac{\xi}{K(\xi; r, z, t)} d\xi \tag{89}$$

$$t = \sum z_j \left(\xi_1^2 + \frac{1}{C_j^2}\right)^{1/2} - i\xi_1 r \tag{90}$$

$$K(\xi; r, z, t) = \left[\xi^2 r^2 + \left(t - \sum_j z_j \left(\xi^2 + \frac{1}{C_j}^2\right)^{1/2}\right)^2\right]^{1/2} \tag{91}$$

For each time value at which the displacement is to be determined, the integrations in Eqs. 88 and 89 must be performed for each ray to be considered. Since the variable of integration, ξ, is complex, the integrals are performed in the complex domain. Figure 33 shows path defined in Eq. 87 in the complex plane. The integrands contain branch points at $\xi = ia_4, ia_5, ia_6$ where a_4, a_5 and a_6 are the reciprocals of the Rayleigh, shear and longitudinal wave speeds, respectively. The path of integration is $SM\xi_1(t)$. Point M is located at ib_M where b_M is real and found by solving Eq. 92.

$$-ir + \frac{iz_p b_M}{\eta(ib_M)} + \frac{iz_s b_M}{\zeta(ib_M)} = 0 \tag{92}$$

The presence of the branch points makes numerical integration along this path difficult. The path $QP\xi_1(t)$ is used as an alternative. This is possible since the integrand is analytic to the right of the original contour. Point P is chosen to be equidistant from Q and $\xi_1(t)$. Point Q is fixed at $\xi = i0.8a_6$

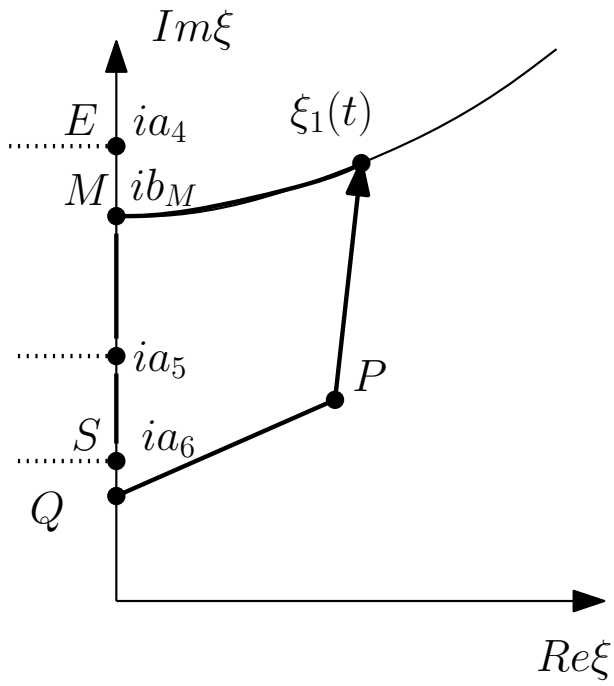

Figure 33: Path of integration in the complex domain

The integration is performed via a complex Gaussian quadrature routine included in MATLAB called quadgk. Once $I_r(r,z,t)$ and $I_z(r,z,t)$ are calculated, the displacements are calculated by convolving $I_r(r,z,t)$ and $I_z(r,z,t)$ with the inverse Laplace transform of $s^3\bar{F}(s)$. For the normal force applied at the surface, this results in Eqs. 93 and 94.

$$u_z(r,z,t) = \frac{f'(t)}{2\pi\mu} * I_z(r,z,t) \tag{93}$$

$$u_r(r,z,t) = \frac{f'(t)}{2\pi\mu} * I_r(r,z,t) \tag{94}$$

The convolutions in these expressions are easily calculated via numerical routines.

The derivative of the time dependency of the source can be calculated via numerical differentiation or analytically if the time dependency is a known differentiable function. While the numerous integrations require significant computation time, the ability of the technique to handle layered media and to determine the motions due to a particular ray path is quite useful. In order to apply generalized ray to model laser generated ultrasound, the source function for thermoelastic expansion is now derived.

4.2.2 Derivation of thermoelastic source function

It has been shown that the stresses caused by relatively low laser energy levels are due to the thermoelastic effect. The absorbed heat causes omnidirectional expansion at the surface of the medium. Although other authors have determined the displacements due to this source, solutions are presented only for special cases and not in the generalized ray theory framework. In order to use the generalized ray formulation for this source, the source function for the so-called Surface Center of Expansion (SCOE) is now derived.

The derivation will start by assuming a point center of expansion some distance z_0 below the surface of an elastic half space as shown in Figure 34. The center of expansion causes only longitudinal waves to propagate from the point of generation. When the longitudinal waves reach a free surface, longitudinal and shear waves can be reflected. The potentials corresponding to the surface center of expansion are found by summing the incident and reflected potentials after taking the limit as the source depth z_0 approaches zero. Pao gives the form of the Hankel Laplace transform of the scalar potentials as in Eqs. 95 and 96. The reflected potentials are determined by multiplying the incident potential by the appropriate reflection coefficient as shown in Eqs. 97 and 98. Here, $\hat{\phi}_r$ corresponds to the reflected longitudinal wave, denoted as LL in Figure 34 and $\hat{\psi}_r$ corresponds to the reflected shear wave denoted by LS.

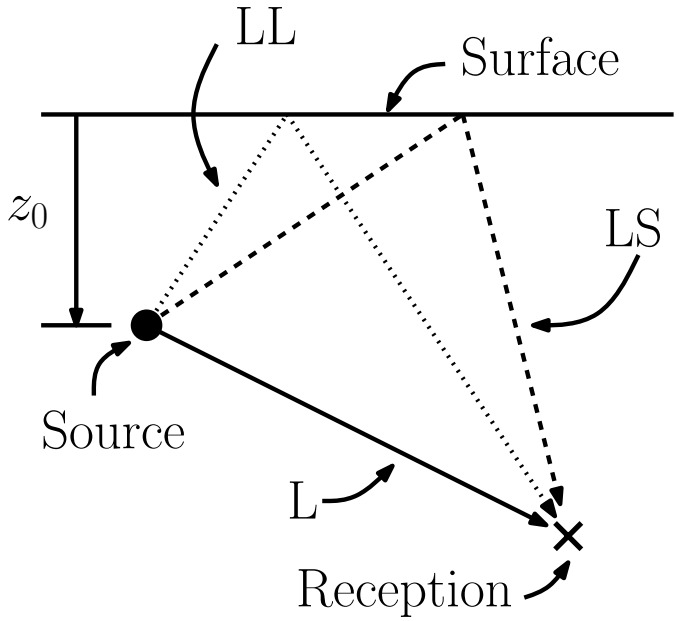

Figure 34: Configuration used for derivation of thermoelastic source

$$\hat{\phi}_0(\xi, z, s) = \frac{\bar{f}(s)}{4\pi C_L^2 s}\frac{1}{\eta}e^{-s\eta|z-z_0|} \tag{95}$$

$$\hat{\psi}_0(\xi, z, s) = 0 \tag{96}$$

$$\hat{\phi}_r = \frac{\bar{f}(s)}{4\pi C_L^2 s}\frac{1}{\eta}R^{PP}e^{-s\eta(z+z_0)} \tag{97}$$

$$\hat{\psi}_r = \frac{\bar{f}(s)}{4\pi C_L^2 s}\frac{1}{\eta}R^{PS}e^{-s\eta z_0 - s\zeta z} \tag{98}$$

Since the thermoelastic source occurs at the surface, the potentials that correspond to this source can be found by adding the incident and reflected potentials and taking the limit as the source depth z_0 approaches zero. This results in the potentials in Eqs. 99 and 100.

$$\hat{\phi} = \frac{\bar{f}(s)}{4\pi C_L^2 s}\frac{1}{\eta}\left(1 + R^{PP}\right)e^{-s\eta z} \tag{99}$$

$$\hat{\psi} = \frac{\bar{f}(s)}{4\pi C_L^2 s}\frac{1}{\eta}R^{PS}e^{-s\zeta z} \tag{100}$$

Expanding the reflection coefficients and simplifying the result yields Eqs. 101 and 102.

$$\hat{\phi} = \frac{\bar{f}(s)}{4\pi C_L^2 s} \frac{8\zeta\xi^2}{\Delta_r} e^{-s\eta z} \tag{101}$$

$$\hat{\psi} = -\frac{\bar{f}(s)}{4\pi C_L^2 s} \frac{4\xi\left(\xi^2+\zeta^2\right)}{\Delta_r} e^{-s\zeta z} \tag{102}$$

The function $\bar{F}(s)$ is the same as used for the buried center of expansion (presented in Table 1), repeated here in Eq. 103

$$\bar{F}(s) = \frac{\bar{f}(s)}{4\pi C_L^2 s} \tag{103}$$

The source functions for the surface center of expansion acoustic source can then be found by inspection, resulting in the functions shown in Eqs. 104 and 105.

$$S_P = \frac{8\zeta\xi^2}{\Delta_r} \tag{104}$$

$$S_V = \frac{-4\xi\left(\xi^2+\zeta^2\right)}{\Delta_r} \tag{105}$$

With the surface center of expansion source functions derived, calculation of the displacement of the medium to a thermoelastic source can be performed.

4.2.3 Calculation of displacements due to laser generated ultrasound

As described in the introduction, the ablative ultrasonic source generates ultrasound through two mechanisms. First, as in thermoelastic generation, the surface is heated because of the absorption of the incident laser light. Secondly, the vaporized material exerts a normal reaction force downward onto the surface as the local pressure of the vaporized material increases rapidly. The temperature rise at the surface due to the incident laser light was studied by Scruby. When a short laser pulse is incident upon the sample surface, the temperature increases quickly and then decreases as the heat diffuses into the sample. The temperature at the surface due to a laser pulse with Gaussian time dependency is shown in Eq. 106. K is the thermal conductivity (240 W m^{-1} K^{-1} for mild steel), κ is thermal diffusivity (1.5e-5 m^2 s^{-1} for mild steel), I_1 is the maximum power density, and τ is the full duration at half maximum for the

Gaussian pulse. The normal force caused by ablation is typically given a Gaussian distribution as shown in Eq. 107 [35]. The normalized time dependencies of the normal force and temperature for $\tau = 10$ ns are shown below in Figure 35 where .

$$T(t) = \frac{\kappa^{1/2}}{K\pi^{1/2}} I_1 e^{-2.7726\frac{t^2}{\tau^2}} * t^{-1/2} \tag{106}$$

$$p(t) = P_1 e^{-2.7726\frac{t^2}{\tau^2}} \tag{107}$$

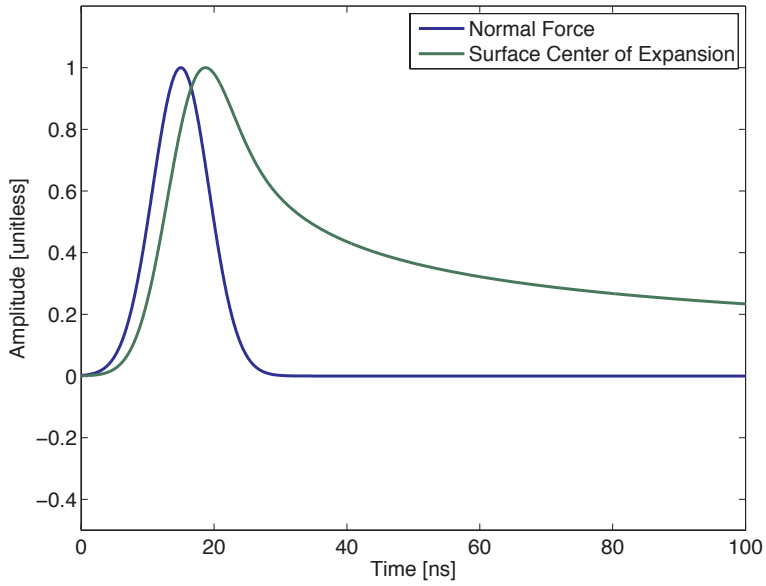

Figure 35: Time dependencies of normal force and surface center of expansion acoustic sources

These time dependencies and the appropriate source functions are used to calculate the displacement of a plate in response to normal force and SCOE sources. The full width half maximum of the temporal distribution of the laser pulse is 10 ns. Figures 36 and 37 show the calculated displacements due to a normal point force and surface center of expansion at a radial distance of 60 mm on the bottom surface of a 12.6 mm thick plate.

The displacements show the arrival of many waves, some of which are indicated in the figures. Both sources create displacements with low frequency components at $t =$

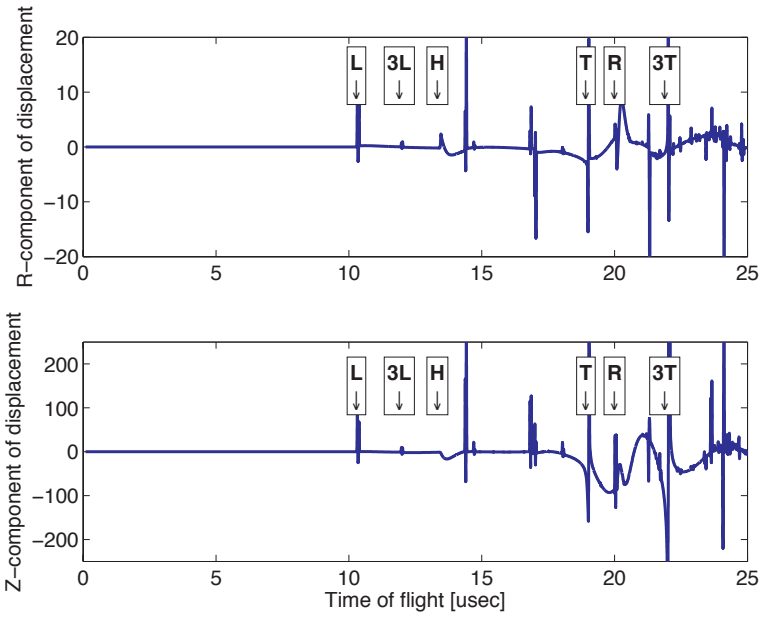

Figure 36: Displacements at $r = 60$ mm due to normal force. L - Longitudinal Wave, T - Shear Wave, H - Head Wave, R - Rayleigh Wave, 3L - Three Segment Longitudinal Wave, 3T - Three Segment Shear Wave

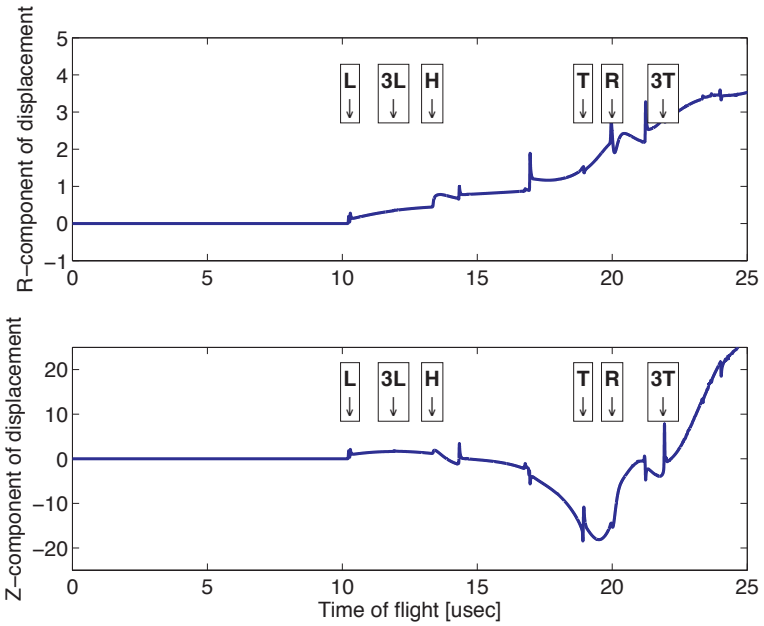

Figure 37: Displacements at $r = 60$ mm due to surface center of expansion. L - Longitudinal Wave, T - Shear Wave, H - Head Wave, R - Rayleigh Wave, 3L - Three Segment Longitudinal Wave, 3T - Three Segment Shear Wave

20 μs. These low frequency components correspond to the arrival of the Rayleigh wave as determined experimentally. The ablative ultrasonic source can be modeled as the

combination of a surface center of expansion and normal force. Figure 38 compares the displacement recorded by the laser interferometer and the calculated displacements due to surface center of expansion and normal force sources. The displacements of the two sources are weighted and summed to produce the ablative source displacement. The weights are determined via a least squares fit to the experimental data. The calculated displacement correlates very well with the experimentally obtained displacement and shows the arrivals of the various waves and the overall trends of the displacement, including the low frequency component that corresponds to the Rayleigh wave.

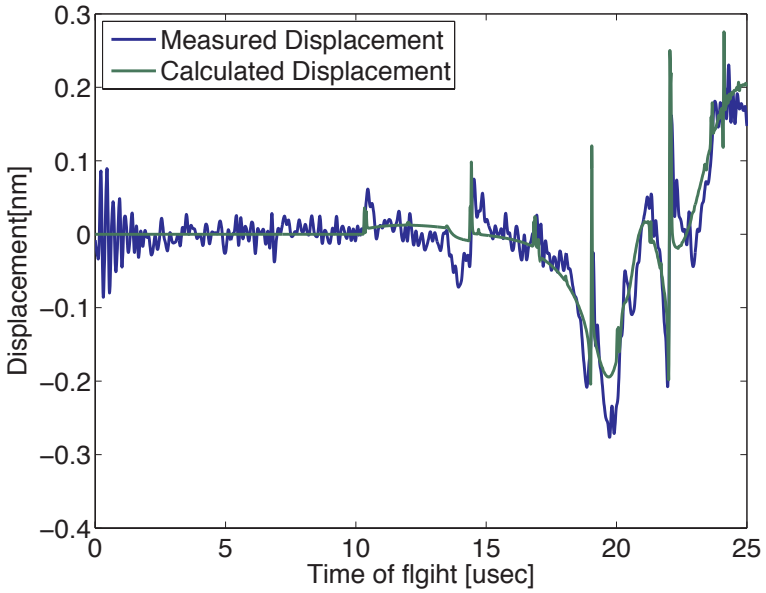

Figure 38: Comparison of measured and calculated displacements

As mentioned in the introduction, the generalized ray formulation is used not only because it is capable of modeling ultrasound propagation in plates, but also because the separation of displacements due to the various rays is inherent to the model. This permits analysis of the various components without the effects of other received rays. In addition, the computation time required to calculate the displacements corresponding to the many rays can be quite large. For the example shown in Figure 38, the displacement of 628 rays were calculated. Had the time range been increased

further beyond 25 μs, a minimum of 2048 additional rays would need to be included in the calculation.

The model was used to calculate the displacement at the bottom of a 12.6 mm thick plate due to the direct rays for radial distances ranging from 0 to 80 mm. Figures 39 and 40 show the calculated z- and r-components of the displacements for an ablative source.

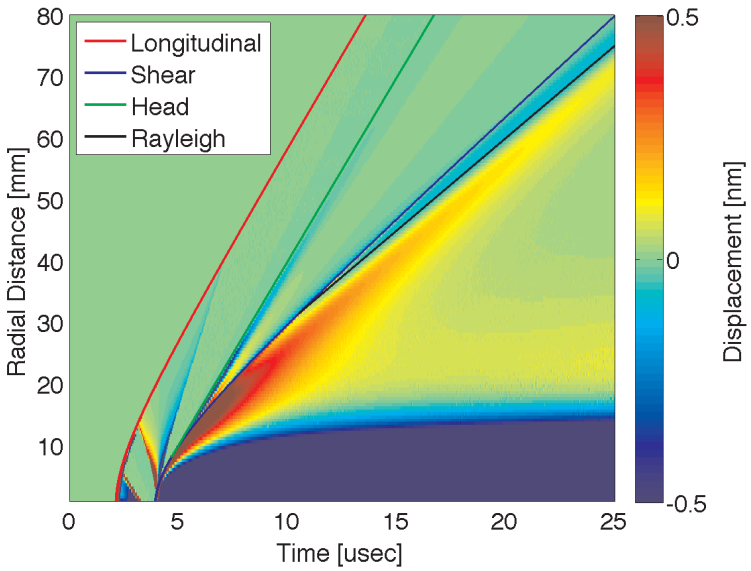

Figure 39: z-components of the displacements for an ablative source

The displacements calculated using the generalized ray theory model show the longitudinal, shear, head, and Rayleigh waves. This shows that the presence of the Rayleigh wave can be attributed to the direct rays. Therefore, the displacements calculated for the direct rays can be used to analyze the wave and provide insight into the means through which the Rayleigh wave is present on the bottom surface of the plate. In addition, the dominant frequency of the Rayleigh waves can be calculated for various thicknesses to permit optimal transducer selection. First, however, the means through which the Rayleigh wave reaches the bottom surface of the plate is investigated.

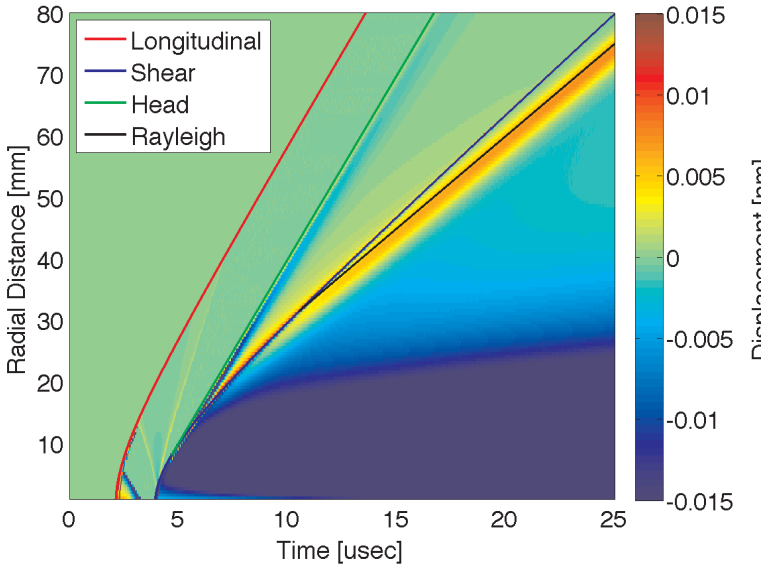

Figure 40: r-components of the displacements for an ablative source

4.3 Analysis of Rayleigh Wave Propagation

In order to determine the means through which the Rayleigh wave reaches the bottom surface of the plate, the generalized ray theory model was used to calculate the displacement due to an ablative laser source. A Gaussian time dependency was again used for the normal force and the time dependency in Eq. 35 for the surface center of expansion with $\tau = 10$ ns. Only the direct rays are considered in order to simplify analysis and show the motions of the plate due to only the incident wave, not the multiple reflections that will be present in the actual plate. Figures 41 through 43 show the magnitude of the displacement for 6.5, 12.8, and 17.0 μs elapsed time, respectively. In Figure 41 the shear wave front is clearly visible and the Rayleigh wave is shown behind the shear wave up to 8 mm below the surface. Figure 42 shows the Rayleigh wave penetrating to the bottom of the plate with the shear wave and Rayleigh wave overlapping at 12.8 μs. At 17.0 μs the Rayleigh wavefront separates from the shear wavefront. The amplitude of the Rayleigh is much lower for larger distances below the surface.

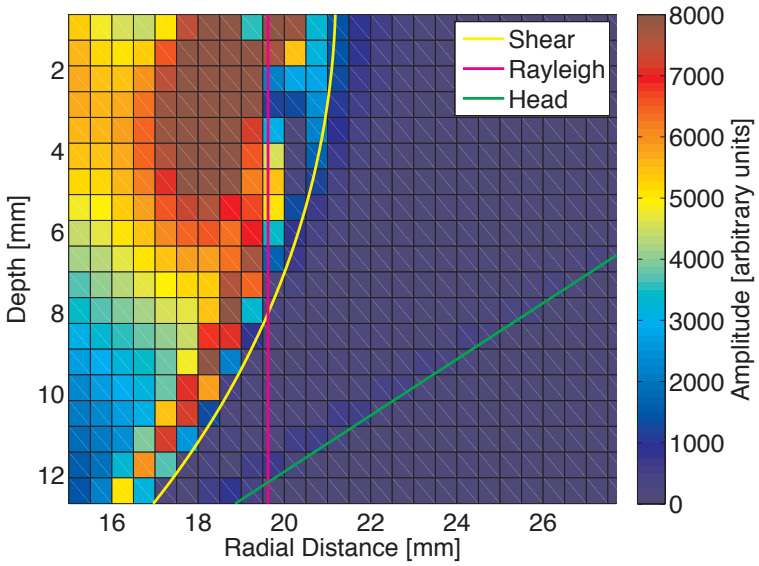

Figure 41: Displacement amplitude at $6.5\mu s$ elapsed time

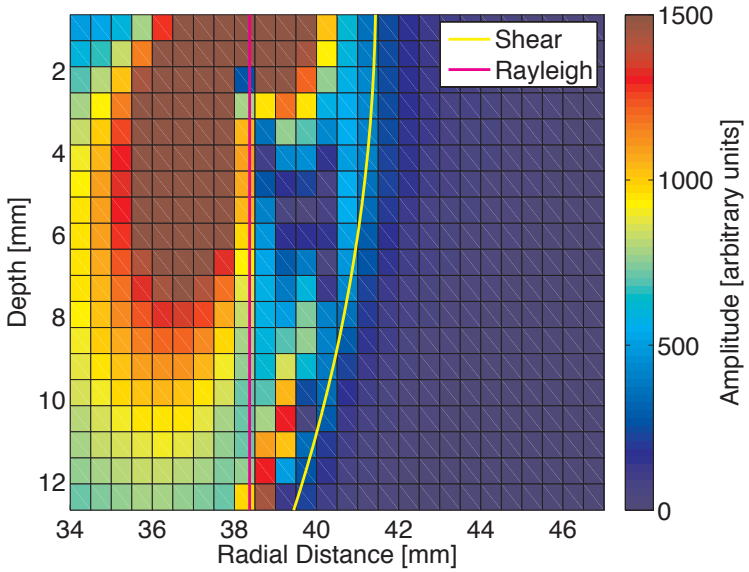

Figure 42: Displacement amplitude at $12.8\mu s$ elapsed time

From the calculated displacements, it is clear that the Rayleigh wave is present deep into the plate. Therefore, the assumption that the Rayleigh wave is the result of mode conversion of bulk waves is incorrect. Rather, the Rayleigh wave propagates through the plate with a cylindrical wavefront with axis of symmetry collinear with the z-axis. The calculated displacements confirm that the Rayleigh wave observed

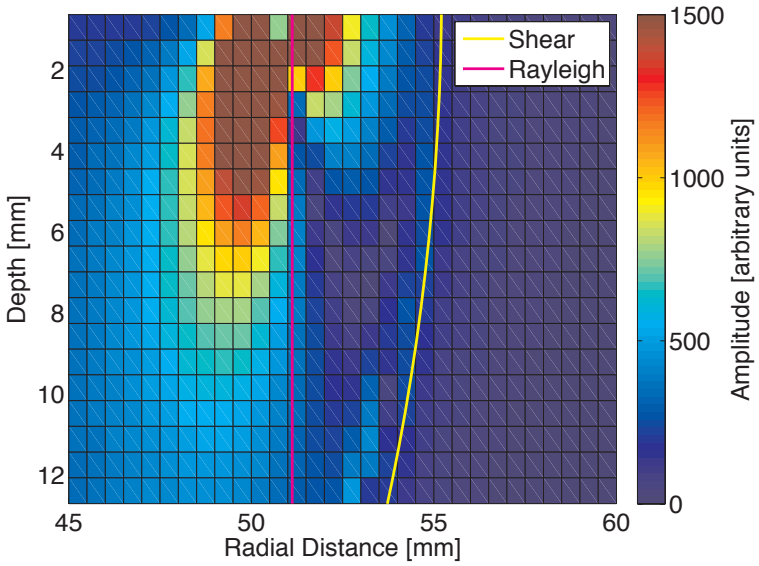

Figure 43: Displacement amplitude at 17.0μs elapsed time

on the bottom surface of the plate is not due to mode conversion of bulk waves, but rather due to the penetration of the wave through the thickness of the plate. Now that the means through which the Rayleigh wave reaches the bottom surface is understood, it is necessary to determine the frequency content of the wave.

4.4 Frequency Content of Laser Generated Rayleigh Waves

As mentioned in the introduction, the frequency content of the Rayleigh wave traveling on the bottom surface of a plate will depend on the thickness of the plate. As thickness increases, the higher frequency components are greatly reduced. It is necessary to know the dominant frequency of the Rayleigh wave in order to appropriately specify the inspection equipment such as transducers, filters, and amplifiers. In this section, experimentally obtained ultrasonic signals and displacements calculated by the generalized ray theory model are analyzed to determine the frequency content of the Rayleigh wave as a function of plate thickness.

Rayleigh waves were observed in plates of thicknesses equal to 3.3, 4.8, 6.3, 9.5, 12.6, 15.1, 19.0 and 25.4 mm. Each plate is placed in turn in a fixture on an automated

positioning system. A Continuum Inlite III laser was used to generate ultrasound in the sample via ablation. The laser was configured to emit 60 mJ of energy per pulse, with the laser light focused to a spot 0.5 mm in diameter. A sensor was placed to receive ultrasound on the opposite side of the plate from the generation location. Two different sensors were used: the custom built LURL EMAT (bandwidth 200 kHz to 2 MHz) and a Olympus NDT model C546-SM PZT with wedge designed to receive Rayleigh waves in steel (bandwidth 1.9 to 4.5 MHz). The positioning system was configured to vary the radial distance from source to receiver from 0 to 160 mm in 1.0 mm increments. At each measurement location, the laser was fired 64 times and the signals are recorded and averaged. The laser incident location and sensor placement are shown schematically in Figure 44.

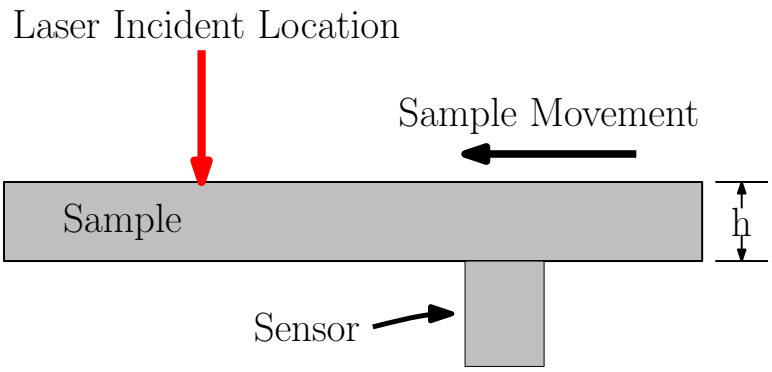

Figure 44: Laser generation and sensor placement for reception of ultrasound

The signals received by the EMAT and PZT are shown in Figures 45 - 46 and Figures 47 - 48, respectively. The abscissa corresponds to time and the ordinate is the radial distance from the source to the receiver and gray scale represents signal voltage as shown in the color bar. The signals recorded by the EMAT in the 3.3 and 4.8 mm thick plates do not have a clear component that corresponds with the predicted Rayleigh time of flight. For the 6.3-19.0 mm thick plates, signals that correspond to the predicted Rayleigh time of flight are present with amplitude of the signals decreasing as plate thickness increases. The 25.4 mm thick plate does not show

a significant signal at the Rayleigh time of flight, most likely due to attenuation of the wave. Signals acquired by the PZT show a wave traveling at the Rayleigh speed for all plate thicknesses. The signals recorded in the thicker plates show distinct wavefronts due to the various waves that reach the receiver. For the thinner plates, distinct wavefronts are not clearly seen in the scans. Rather, the waves overlap and interfere with each other. As plate thickness decreases, the free surfaces of the plate cause the generated ultrasound to propagate as Lamb waves.

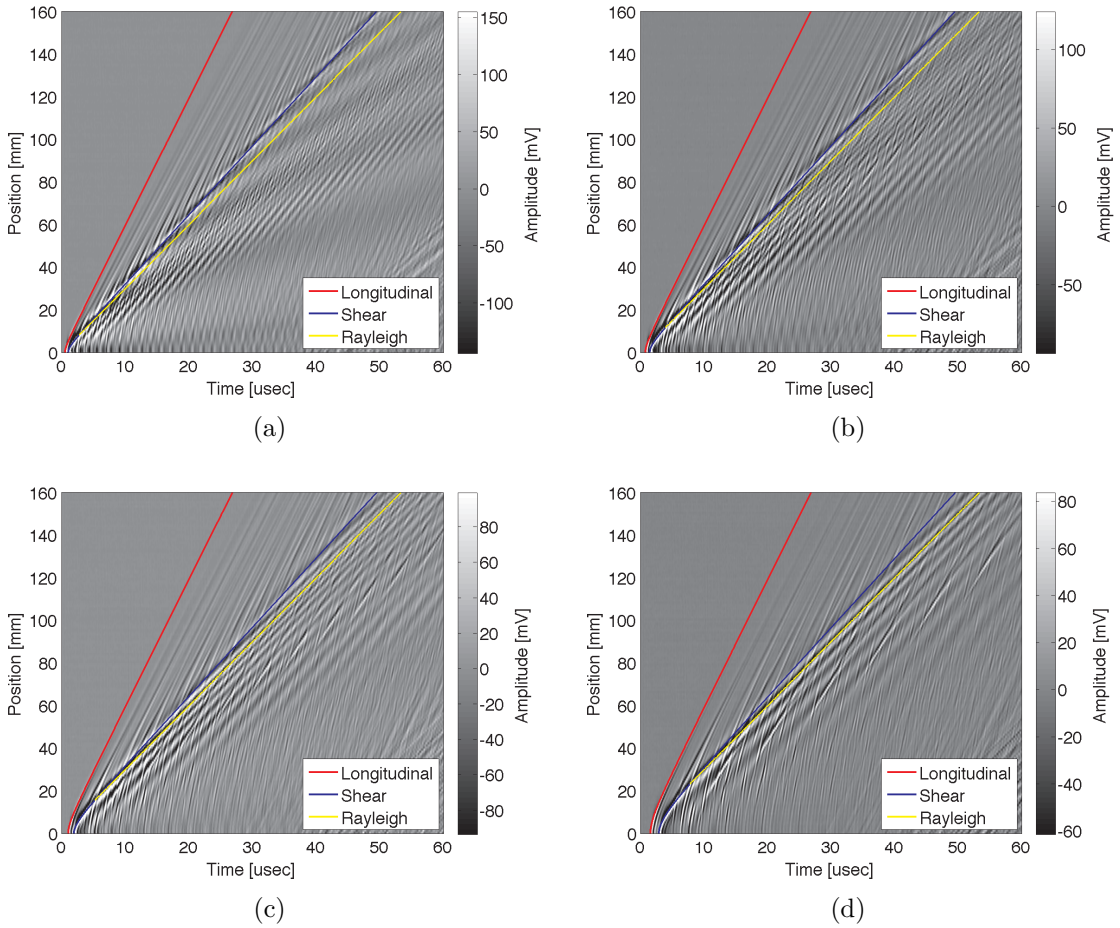

Figure 45: Signals recorded by LURL EMAT for (a) 3.3, (b) 4.8, (c) 6.3, (d) 9.5 mm thick steel plates

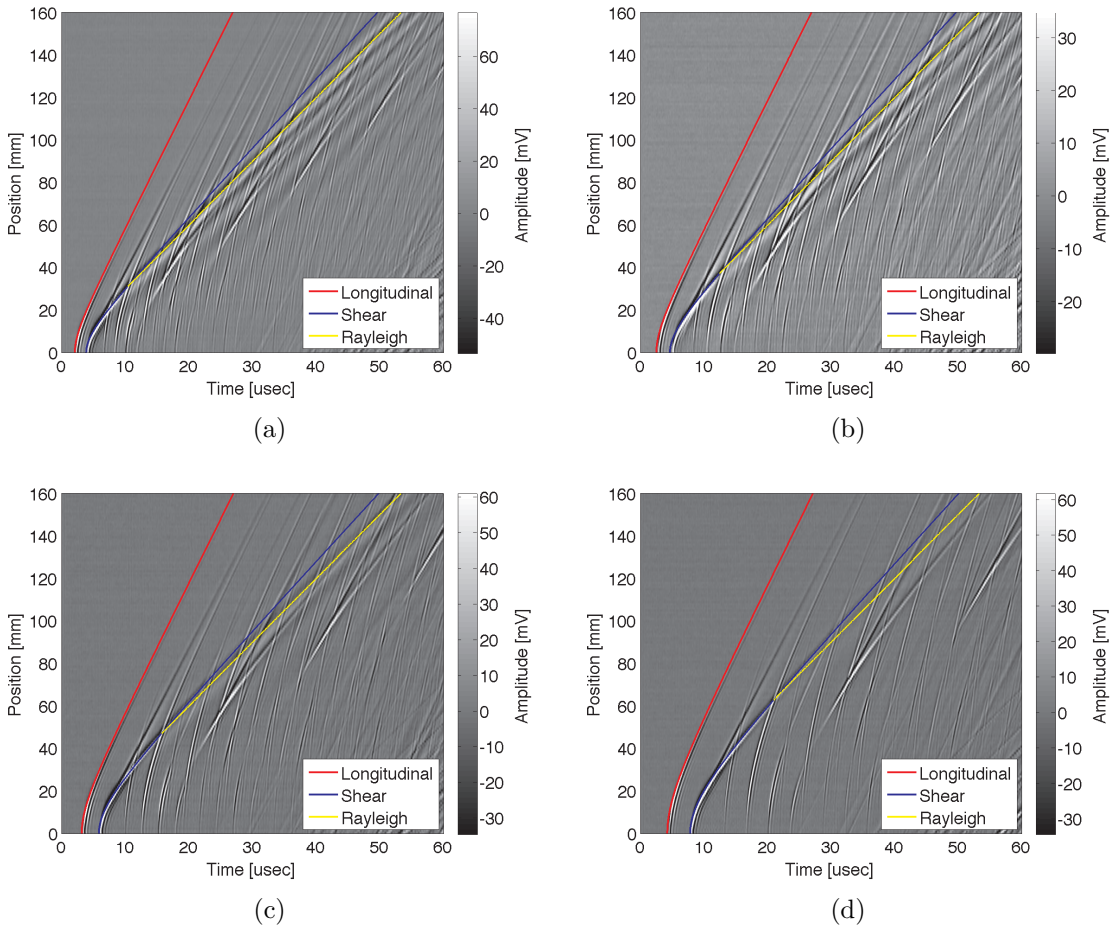

Figure 46: Signals recorded by LURL EMAT for (a) 12.6, (b) 15.1, (c) 19.0 and (d) 25.4 mm thick steel plates

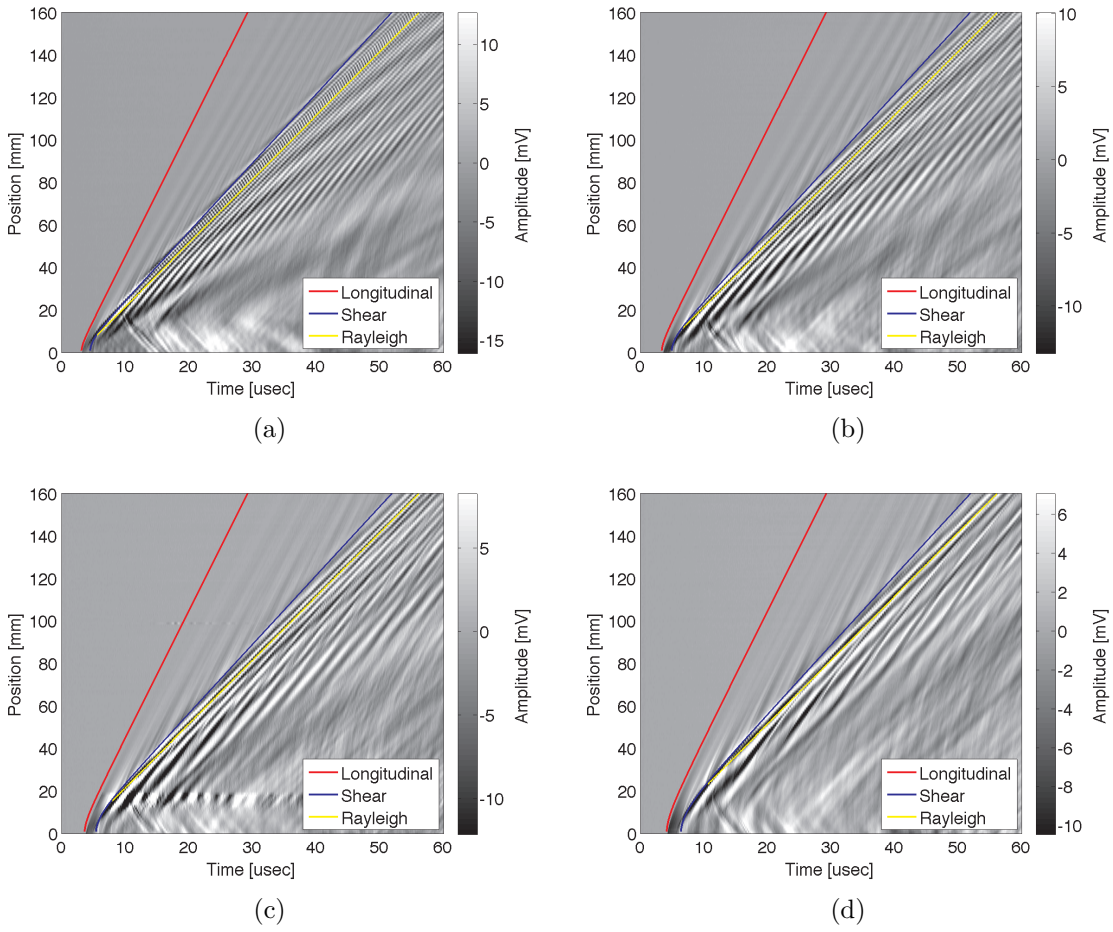

Figure 47: Signals recorded by PZT for (a) 3.3, (b) 4.8, (c) 6.3, (d) 9.5 mm thick steel plates

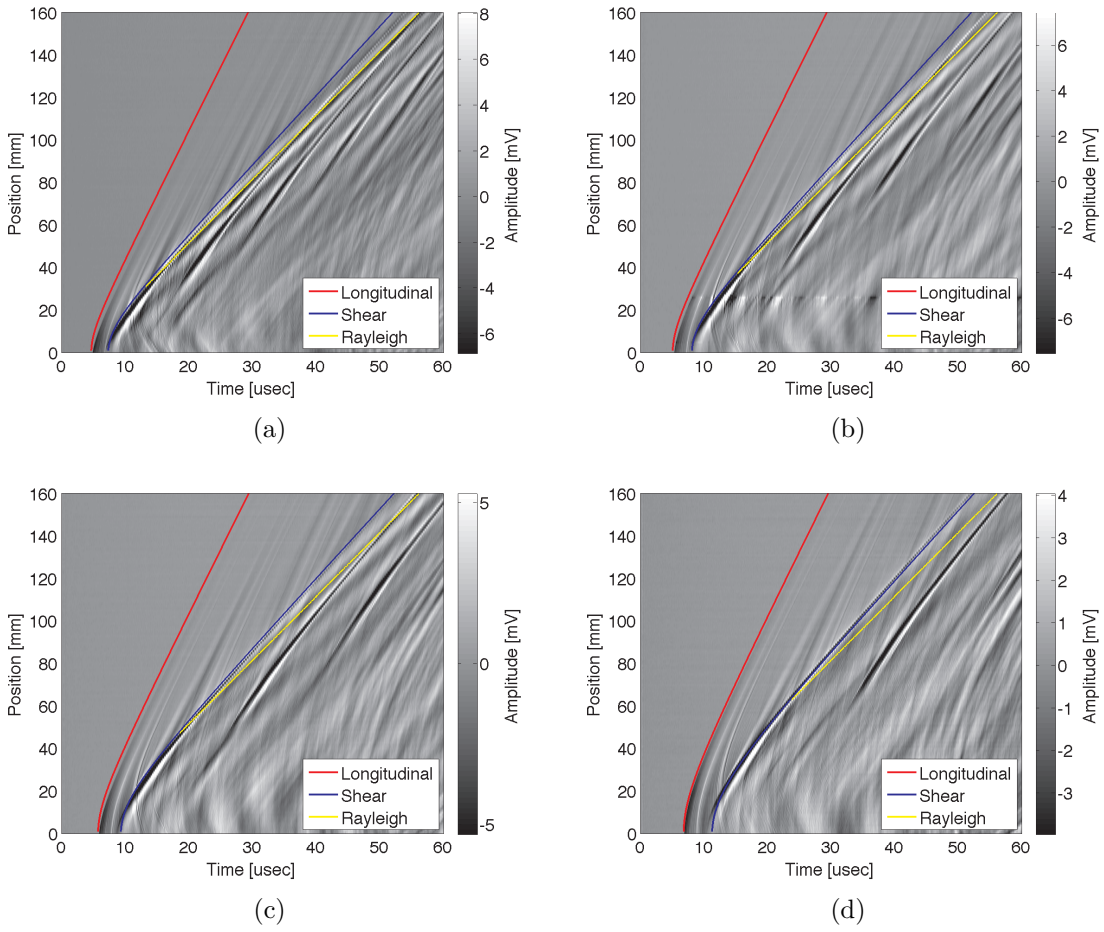

Figure 48: Signals recorded by PZT for (a) 12.6, (b) 15.1, (c) 19.0 and (d) 25.4 mm thick steel plates

Lamb waves are the result of the multitude of bulk waves reflecting at the free surfaces of a plate interfering with each other. Many wave modes may be created by a laser ultrasonic source. They are classified as either symmetric or antisymmetric modes where the displacement of the plate is either symmetric or antisymmetric about the mid-plane of the plate. The modes are dispersive, meaning that the phase velocity can vary with frequency. The phase velocities of the fundamental symmetric and antisymmetric modes S_0 and A_0 are shown in Figure 49 as a function of frequency for 3.3 and 12.6 mm thick steel plates.

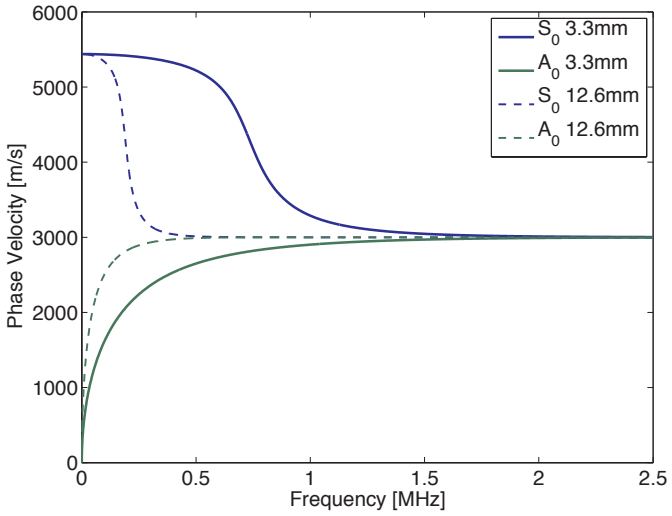

Figure 49: S_0 and A_0 phase velocity versus frequency for 3.3 and 12.6 mm thick steel plates

The phase velocity of the two modes changes as frequency increases from zero. At higher frequencies, the phase velocity approaches the Rayleigh wave speed and the modes become non-dispersive. The frequency at which the mode transitions to non-dispersive propagation depends on thickness. As plate thickness increases, this transition frequency decreases. This explains why the EMAT is unable to receive the non-dispersive wave in the 3.3 and 4.8 mm plates. The non-dispersive portions of the waves traveling in these plates exist at higher frequencies than the EMAT is capable of receiving. The PZT is capable of receiving the Rayleigh wave in thin plates because it

is capable of receiving the frequency range at which the fundamental Lamb modes are non-dispersive. Viktorov studied the relationship between Rayleigh waves and Lamb waves from a guided wave perspective. This work showed that the nondispersive portions of the S_0 and A_0 modes are in phase and the combine to propagate with $r-$ and $z-$displacements nearly equal to those of a Rayleigh wave for propagation distances less than a threshold distance [60]. This threshold is dependent on plate thickness and ultrasound wavelength. As the plate thickness to wavelength ratio decreases, the threshold decreases. For propagation distances above this threshold, the small differences in phase and group velocity of the S_0 and A_0 modes cause the phase difference between the two modes to increase resulting in displacements that differ greatly from those of a Rayleigh wave. This effect was shown experimentally by Masserey and Fromme [38]. The authors showed that the energy transfers from the top to the bottom surface of the plate as the wave propagates over large distances. For a 12.6 mm thick steel plate, this effect will be pronounced for propagation distances above approxiately 250 mm.

In order to calculate the dominant frequency of the Rayleigh wave, it must be isolated from the complex recorded signals. To this end, the signals recorded at radial distances from 140 to 160 mm were translated in time and summed according to Eq. 44. This caused the phase of the components of the signals that have phase velocity equal to the Rayleigh wave speed to be aligned and constructively interfered, resulting in increased Rayleigh wave amplitude relative to the other waves received by the sensor. The resulting signals are presented in Figure 50 and 51. As mentioned, the EMAT was unable to receive Rayleigh waves in the 3.3 and 4.8 mm thick plates. Rayleigh waves were received by the PZT for all plate thicknesses. The generalized ray theory model was used to calculate the displacements due to the ablative source for thicknesses ranging from 1.3 to 25.4 mm and are shown in Figures 52. The isolated Rayleigh waves and calculated displacements exhibit rapidly decreasing amplitude

and frequency as plate thickness increases. In order to effectively use the Rayleigh wave, the dominant frequency of the wave must be determined to effectively specify inspection equipment.

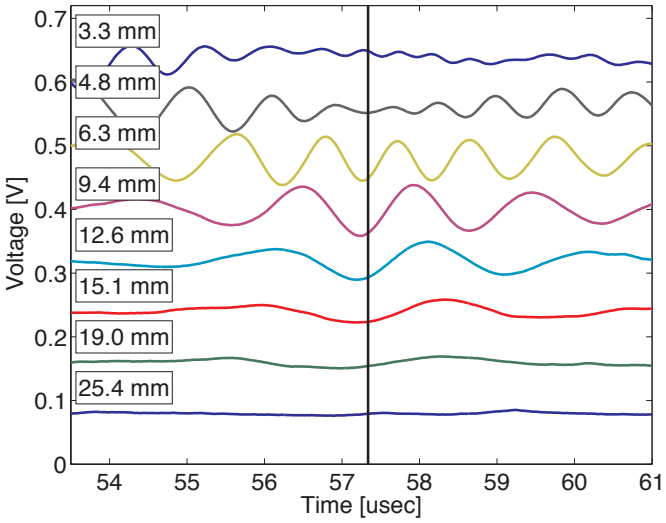

Figure 50: Isolated Rayleigh waves received by the EMAT

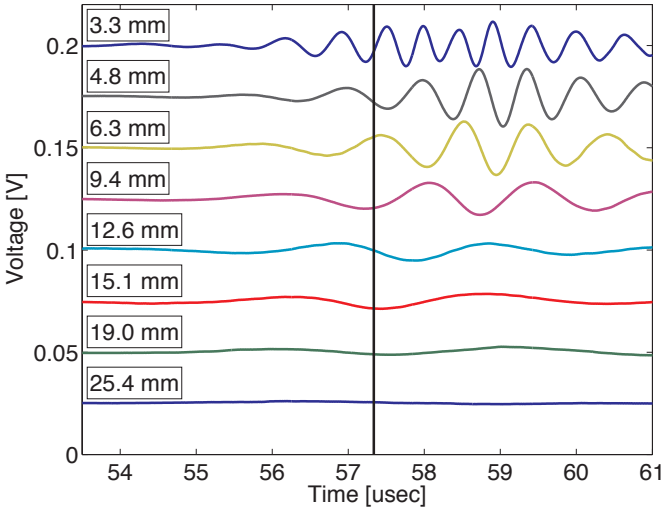

Figure 51: Isolated Rayleigh waves received by the PZT

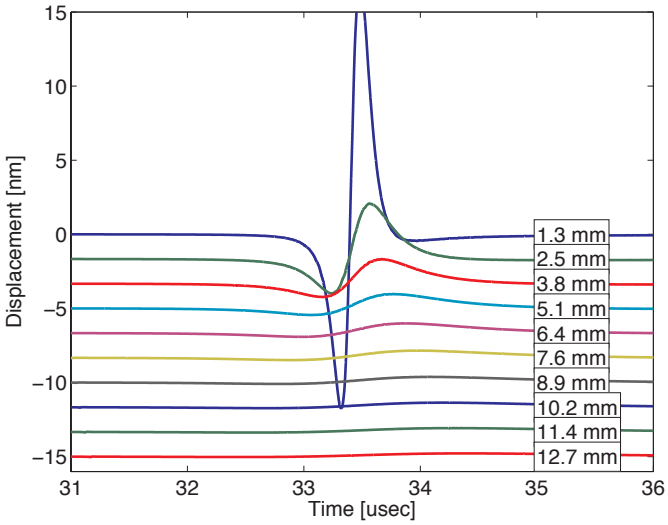

(a)

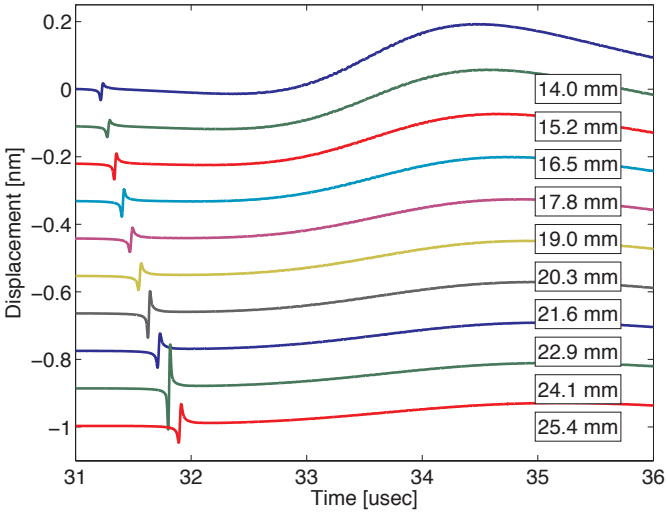

(b)

Figure 52: Displacements calculated by generalized ray theory

The Continuous Wavelet Transform (CWT) was used to transform the signals from the time domain to the time-frequency domain because of the non-stationary nature of the signals. The CWT of a signal is calculated by convolving the signal with the mother wavelet ψ after it has been dilated by the scale parameter a as shown below in Eq. 108 [37]. Here, WS is the continuous wavelet transform of function $s(t)$. When the CWT is performed on a sampled signal, the result is a set of values called wavelet coefficients for each scale and time pair used in the transformation.

$$WS(u,a) = \int_{-\infty}^{+\infty} s(t) \frac{1}{\sqrt{a}} \psi^* \left(\frac{t-u}{a} \right) dt \tag{108}$$

The complex Morlet mother wavelet, defined below in Eq. 109, was used in this work because of its oscillatory nature. The term f_b is a frequency bandwidth parameter and f_c is the center frequency of the mother wavelet. In this work, $f_c = 0.7985$ and $f_b = 0.75$ were used.

$$\psi(t) = \frac{1}{\sqrt{\pi f_b}} e^{2i\pi f_c t} e^{-\frac{t^2}{f_b}} \tag{109}$$

In order to obtain a time-frequency representation, scale can be related to frequency through the relationship shown in Eq. 110.

$$f \approx \frac{F_c}{aT} \tag{110}$$

Where F_c is the center frequency of the mother wavelet and T is the sampling period.

The absolute value of the wavelet coefficients for the isolated Rayleigh waves received by the EMAT and PZT are shown in Figures 53-56. The time of flight of the Rayleigh wave is 57.3 μs for all figures. The figures show the presence of the Rayleigh wave as a region of higher amplitude as indicated by the colorbar. As the plate thickness increases, the peak wavelet coefficient occurs at a lower frequency and the amplitude of the coefficients decreases. For example, the CWT of the Rayleigh

wave received by the EMAT in the 25.4 mm plate shows a peak amplitude comparable to the noise amplitude.

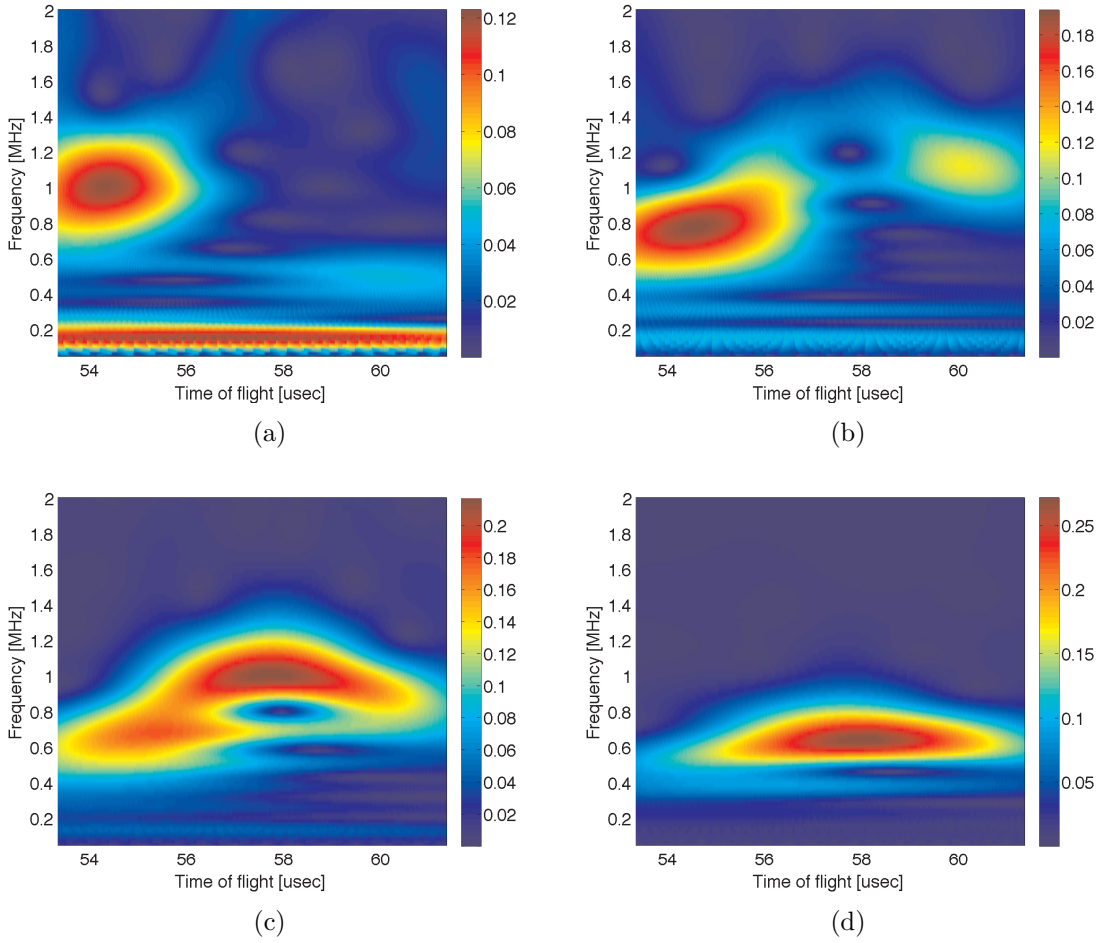

Figure 53: CWT of Rayleigh wave received by EMAT for (a) 3.3, (b) 4.8, (c) 6.3, (d) 9.5 mm thick steel plates

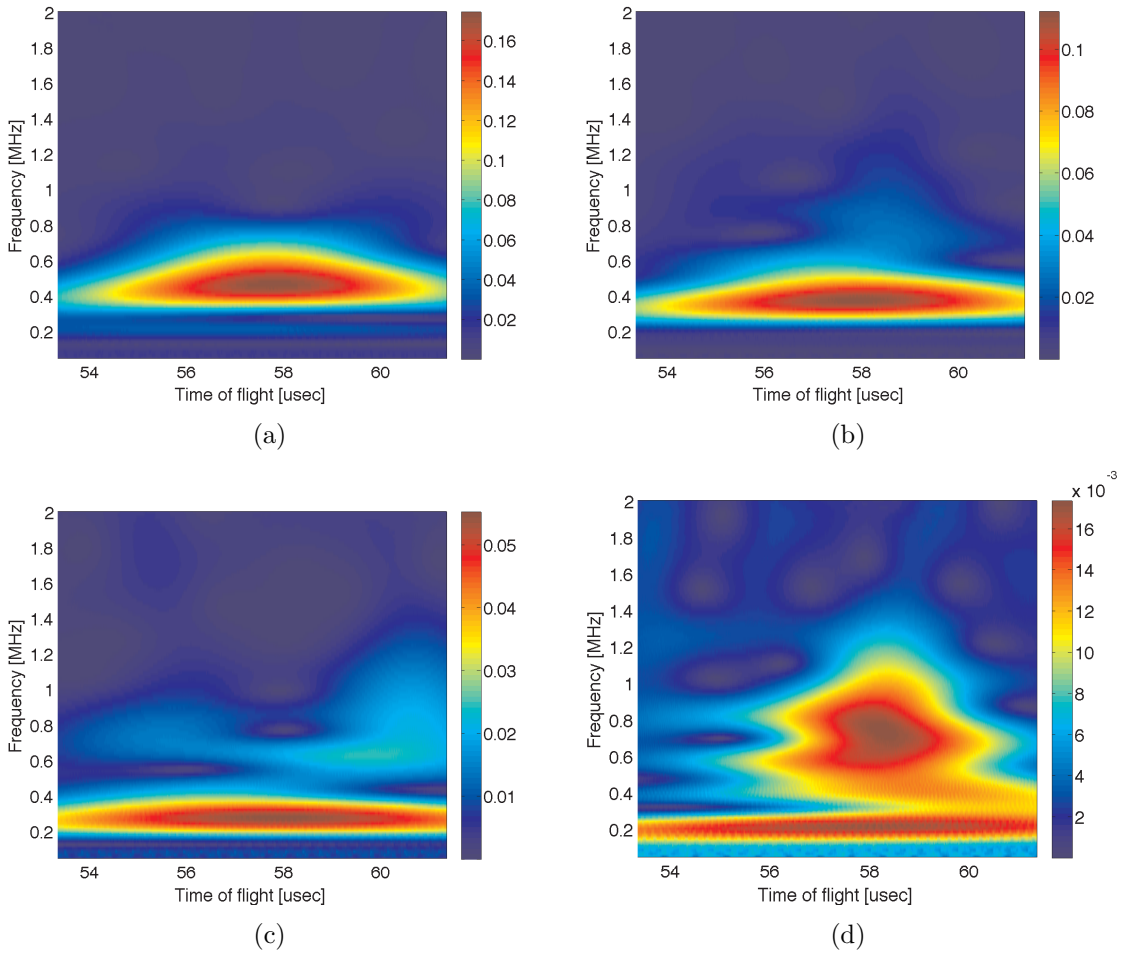

Figure 54: CWT of Rayleigh wave received by EMAT for (a) 12.6, (b) 15.1, (c) 19.0 and (d) 25.4 mm thick steel plates

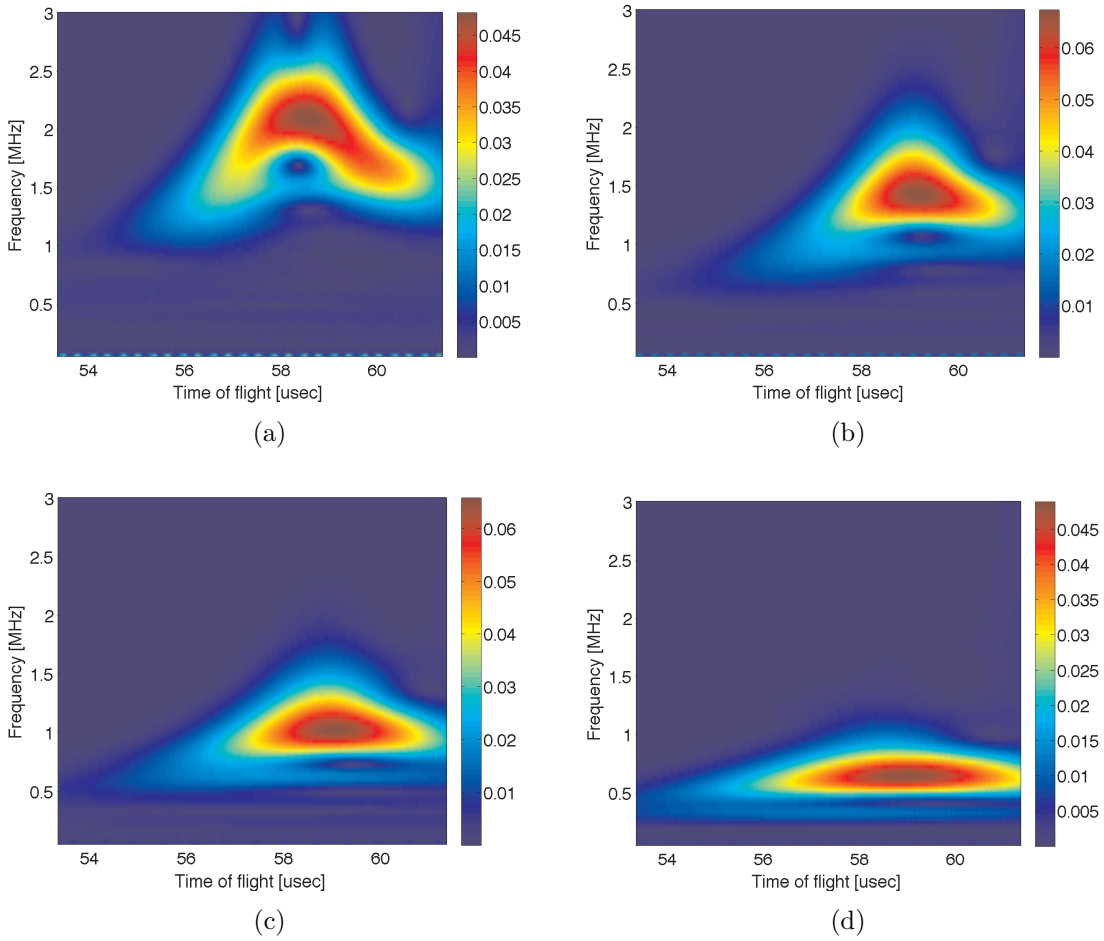

Figure 55: CWT of Rayleigh wave received by wedge transducer PZT for (a) 3.3, (b) 4.8, (c) 6.3, (d) 9.5 mm thick steel plates

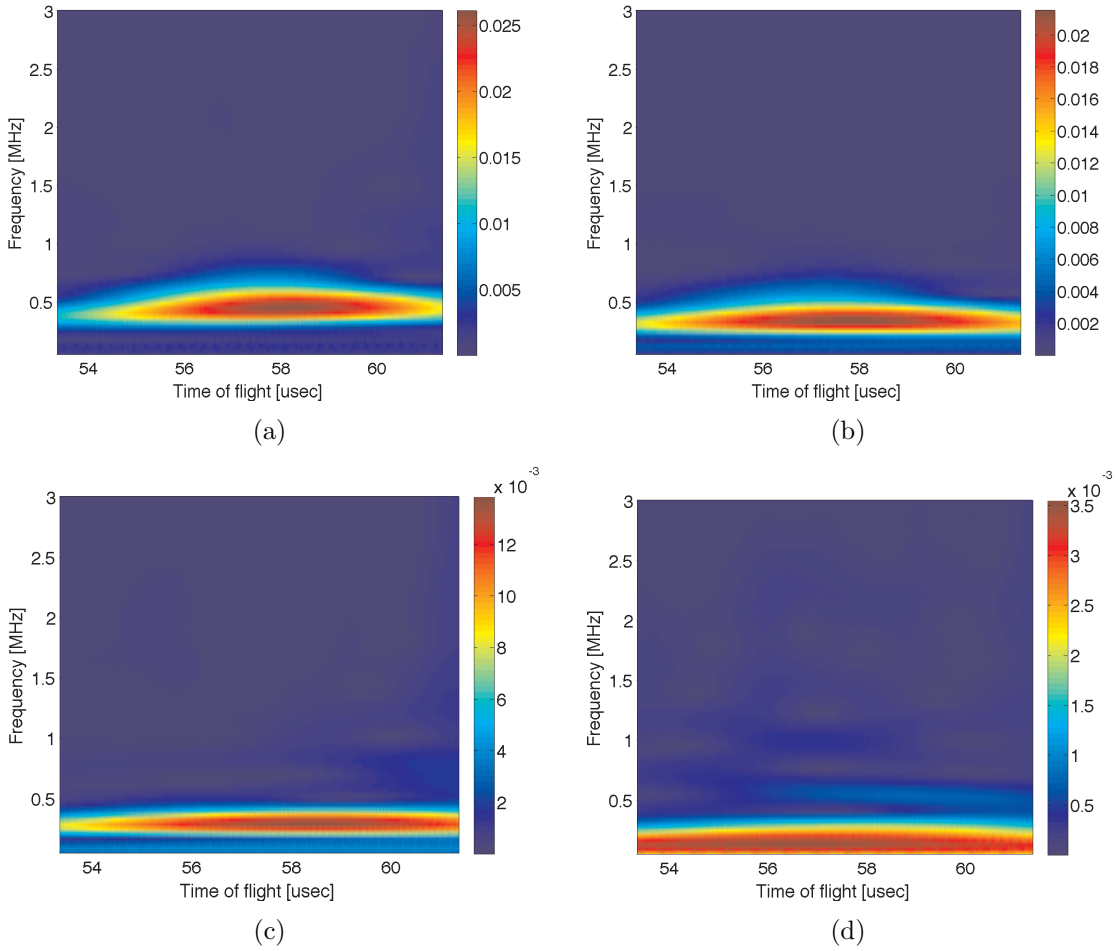

Figure 56: CWT of Rayleigh wave received by wedge transducer PZT for (a) 12.6, (b) 15.1, (c) 19.0 and (d) 25.4 mm thick steel plates

The dominant frequency of the Rayleigh wave is defined as the frequency at which the maximum CWT coefficient is found in the range 50 kHz to 3 MHz. The dominant frequency was calculated for Rayleigh waves present in the signals received by the EMAT, Wedge PZT and laser interferometer in addition to the calculated displacements for the ablative source. The dominant frequencies versus plate thickness are shown in Figure 57.

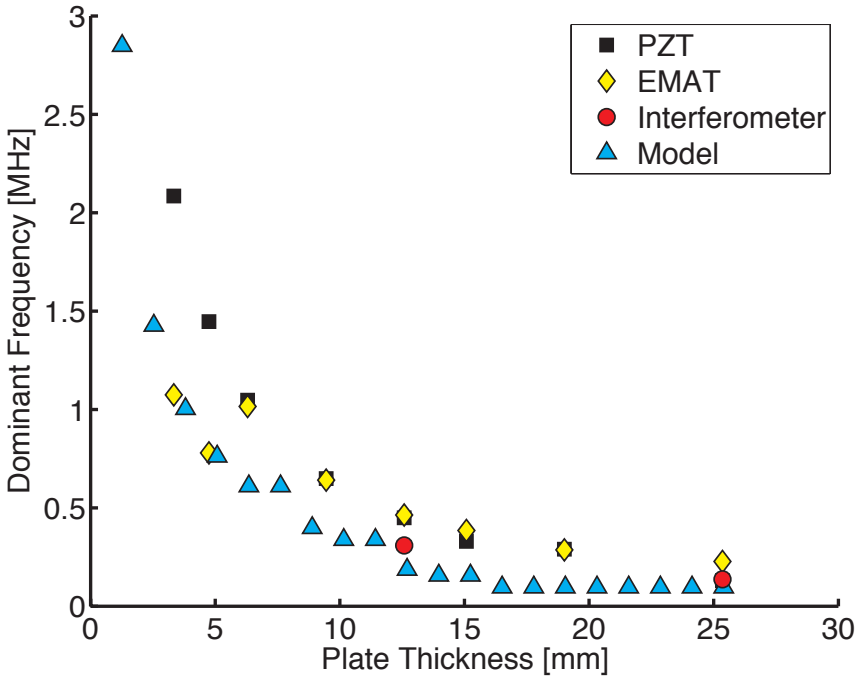

Figure 57: Dominant frequency versus plate thickness

The dominant frequencies in the signals recorded by the EMAT and PZT correlate for plate thicknesses from 6.3 mm to 25.4 mm. For the 3.3 and 4.8 mm thick plates, the signals received by the EMAT have a lower dominant frequency than those received by the PZT. This discrepancy is because of the lower upper cutoff frequency of the EMAT. Since the EMAT is unable to receive waves at frequencies above 2 MHz, the dominant frequency of the signals received by the EMAT will be lower than the dominant frequency of the signals received by the PZT. The dominant frequencies of the displacements calculated based on the generalized ray model are lower than

those corresponding to the PZT and EMAT. This may be caused by the low frequency cutoff of the transducers. The band pass nature of the transducers results in a reduced amplitude of frequencies below their low frequency cutoff. This affects the dominant frequency calculation, resulting in a higher dominant frequency. The dominant frequencies of the signals received by the laser interferometer correlate to those predicted by the model. This is because the interferometer has a low frequency cutoff much lower than the cutoff frequencies of the EMAT and PZT. This results in a lower dominant frequency.

The generalized ray theory has been shown to be an effective tool at predicting the frequency content of received Rayleigh waves on the bottom surface of plates. The distance at which the Rayleigh wave is first seen on the bottom surface of the plate was predicted by the model and validated by experimentally obtained ultrasonic signals. The dominant frequency of the Rayleigh wave has been shown to vary with plate thickness and was predicted by the model. Now that the RGLS Time of Flight technique is fully understood, the sensor placement is optimized to provide the largest signal amplitude.

CHAPTER V

OPTIMIZATION OF INSPECTION SYSTEM PARAMETERS

Effective application of ultrasonic time of flight based measurement techniques require optimal transducer placement. This is particularly important when the ultrasound is generated by a laser. The ultrasound generated by laser point and line sources is not focused. In addition, longitudinal, shear and Rayleigh waves are generated simultaneously, increasing the number of unwanted waves present in the sample. These waves may interfere with the wave used for measurement, resulting in error. In this chapter, a procedure for determining the optimal placement of sensors is presented and applied towards configuration of the ultrasonic penetration depth measurement system. First, the RGLS ToF technique is verified by using it to measure the penetration depth of a sample with varying penetration depth.

5.1 Verification of RGLS ToF Technique

In order to verify the RGLS ToF technique is capable of accurately measuring penetration depth, an experiment is performed. Two pieces of 1018 steel are welded in a butt weld configuration. The two pieces each measure 4 x 12 x 0.5 inches (101.5 x 302.5 x 12.6 mm) in size. The welding system was programmed to weld along an 8 inch (203 mm) long path. The arc voltage was set to a constant 25 V and the torch was held fixed 12.7 mm above the surface of the samples. The samples were placed on a fixture that moves below the torch at a velocity equal to 0.375 in/s (9.5 mm/s). The wire feed rate was varied while welding in a ramp profile starting at 300 in/min and ending at 600 in/min as shown in Figure 58. This profile was chosen in order to

create a sample with penetration depth that varies from approximately 2-4.5 mm.

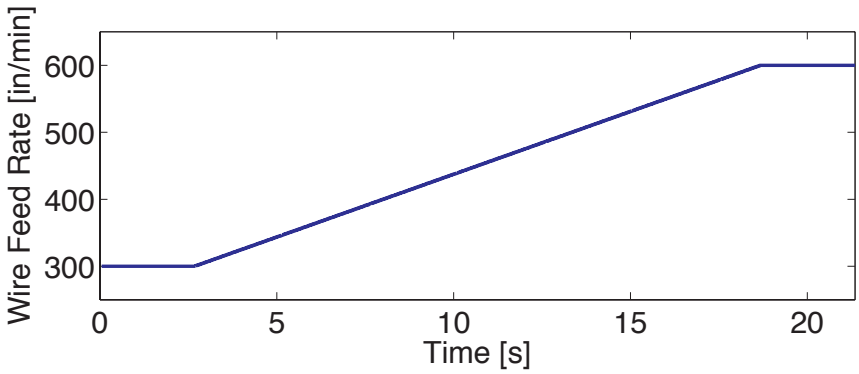

Figure 58: Wire feed rate commanded during welding

After cooling to room temperature, the sample was inspected using the automated inspection system. The laser was positioned 80 mm from the weld seam on one side of the weld. The EMAT is located 80 mm from the weld seam on the opposite side of the weld. This configuration was successfully used in previous works to apply the RGLS ToF technique. The setup used in this experiment is shown in Figure 59. The sample was supported off the table by means of shims located at the corners of the sample to prevent contact of the bottom surface of the samples and the positioning table. If the samples were placed directly on the table, the Rayleigh wave traveling along the bottom of the sample may be affected. The samples were inspected at locations spaced 0.476 mm apart. The system positioned the samples at a location, fired the laser 20 times, and recorded the data for each laser fire. The samples were then positioned at the next inspection location and the process was repeated. The 20 signals recorded at each location were averaged to increase the signal to noise ratio.

After inspection, the geometry of the weld was measured destructively by sectioning the weld. Material was removed up to the center plane, cutting the weld bead down the length of the sample and separating the two plates. The samples were cut approximately 2 mm to the side of the weld seam by a waterjet machine. The waterjet machine is favorable compared to using a bandsaw or other traditional metal cutting

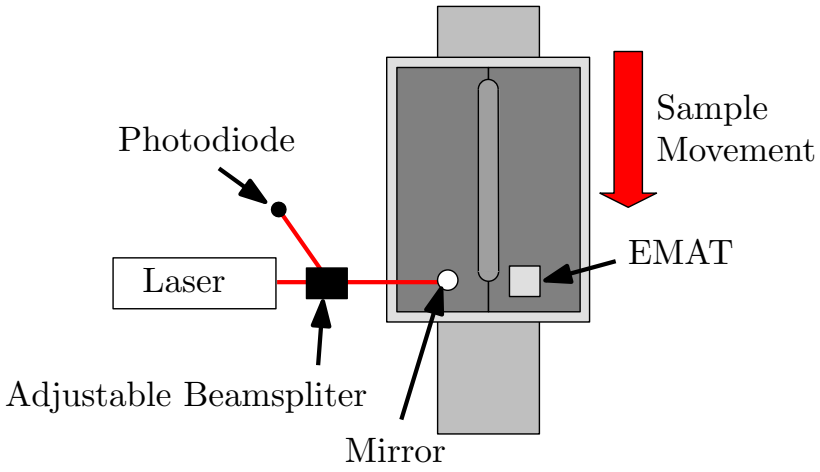

Figure 59: Experimental setup for offline inspection

tools because of the toughness of the weld bead. The remaining material was then machined to the weld seam using a carbide end mill. Because of the gap between the samples, the weld bead protrudes from the edge of the remaining sample a small amount (approximately 0.2 mm). The sample was then painted with black paint and approximately 0.08 mm are removed from the bead. This leaves a exposed weld bead and a painted background. The sample was then placed on a flatbed scanner and an image of the section obtained. The image obtained is shown below in Figure 60.

Figure 60: Image of weld section at weld seam

Custom MATLAB codes have been written that permit measurement of the weld penetration and reinforcement height based on the section image. The codes allow the user to specify the top edge of the sample to define the baseline for zero penetration and reinforcement. Then the user specifies the start and end of the weld. After thresholding the image, the program determines the extent of the weld bead, recording the distance from the baseline for each location along the weld. The code performs the measurement regardless of the orientation of sample in the image as long as the

orientation of the sample does not exceed 45 degrees measured to the horizontal. For this sample, the weld reinforcement width was also measured by removing the weld reinforcement and using the MATLAB program. The weld penetration depth and reinforcement width and height are shown in Figure 61. As desired, the penetration

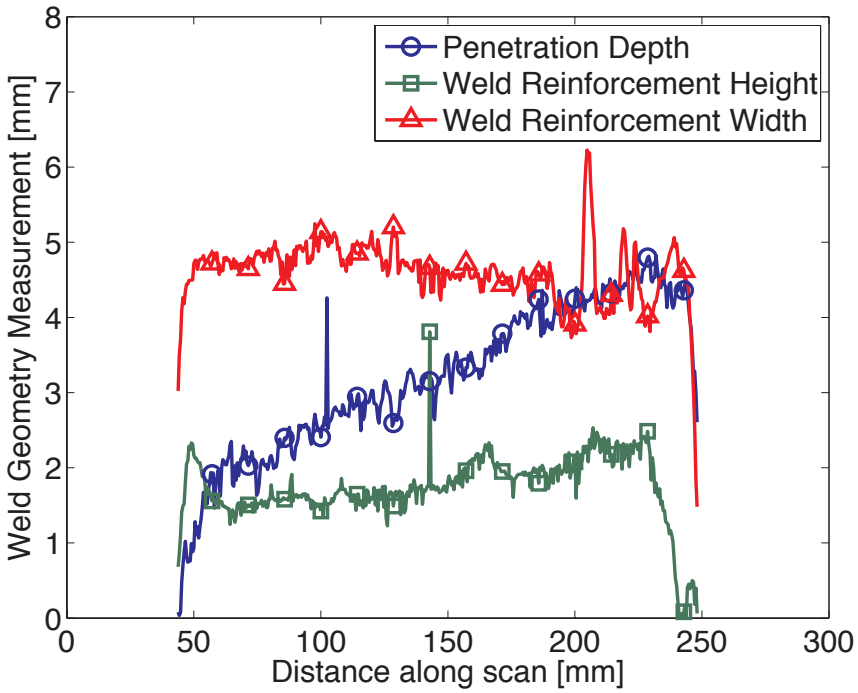

Figure 61: Weld Geometry Measurements Obtained via Destructive Means

depth increases from approximately 2 to 4.5 mm over the length of the weld. The reinforcement height and width fluctuate and are less sensitive to changes in wire feed rate. This is consistent with statements in the literature that say wire feed rate has minimal effect on reinforcement compared to the effect on penetration depth.

The ultrasonic signals obtained before cut checks were performed are shown in Figure 62. The abscissa represents time and the ordinate axis represents position along the scan. The grayscale value is related to signal voltage as shown in the color bar. Ridges in the signal indicating the arrival of a wave are present from 47.5 to 49 μs. The time of flight for these waves increases as penetration depth increases. Based on the measured penetration depth, the expected time of flight of the RGLS

wave for the measured penetration depth is calculated and shown by the red line in the figure. The ridge in the received signals does not correlate to the expected RGLS time of flight. The expected RGLS time of flight decreases as distance along the scan increases whereas the time of flight of the received wave increases with distance along the scan. In addition, the change in time of flight from the start to the end of the weld is less than that expected for the RGLS wave based on the destructively measured penetration depth. This indicates the waves present in this time range do not correspond to the RGLS path. The time of flight of the wave does vary with location along the weld, so it is expected that the time of flight of the wave is related to weld geometry.

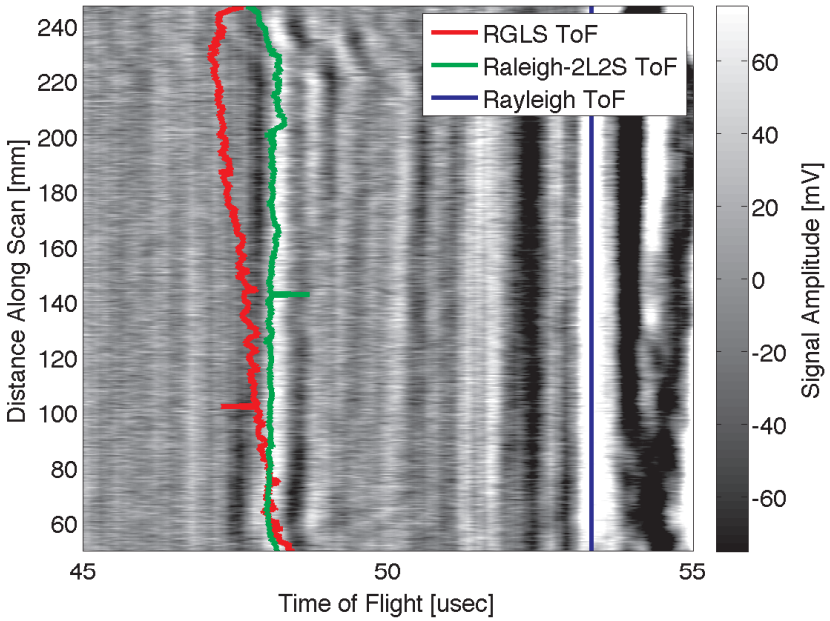

Figure 62: Comparison of RGLS Time of Flight and received signals

Figure 63 shows some of the possible paths from the source to the receiver. Here, the notation used to identify the wave paths is as follows: the letters before the "d" are the paths followed on the source side of the weld. The letters after the "d" stand for the segments followed on the receiver side of the weld. L stands for longitudinal,

S for Shear, and R for Rayleigh. For example, the LdLS path is that where the ultrasound travels as a longitudinal wave to the root of the weld bead, is diffracted to a longitudinal wave that then undergoes mode conversion on the bottom surface to a shear wave that is received by the EMAT. For the RdLS path, a Rayleigh wave traveling on the top surface of the plate reaches the edge of the weld bead and then is diffracted to a longitudinal wave the undergoes mode conversion and is received by the EMAT. It is possible that the Rayleigh wave diffracts at either either edge of the weld bead, before or after the weld seam. In these cases, the time of flight varies not with penetration depth, but with weld reinforcement geometry.

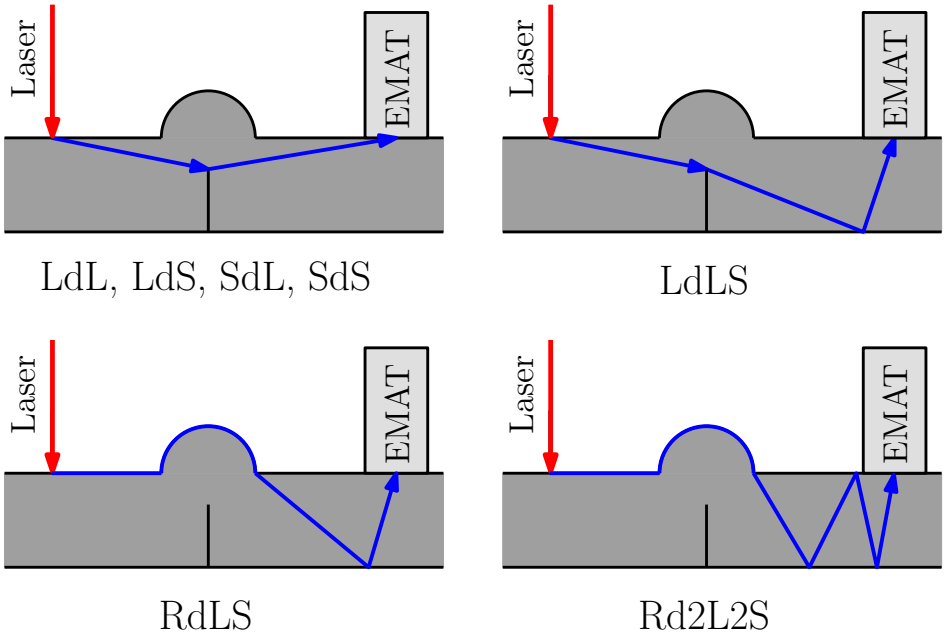

Figure 63: Possible paths from source to receiver

The times of flight of many wave paths were calculated based on the measured weld geometry. The weld reinforcement was assumed to be parabolic in shape with width and height equal to the respective destructive measurements. Of all paths, the time of flight of the Rd2L2S wave path correlates with the time of flight of the ridge present from 47.5 to 49 μs. While this wave path may prove useful for measuring the

weld reinforcement geometry, it does not depend on weld penetration depth. In order to determine if the RGLS wave reaches the receiver, an experiment was performed where the distance from the source to the weld is varied. In this way, the waves that travel as a Rayleigh wave on the source side of the weld can be identified. The source to weld distance was varied from 0 to 90 mm in 1 mm increments. At each location, 64 signals were recorded and averaged. The received signals were then compiled into the scan shown in Figure 64.

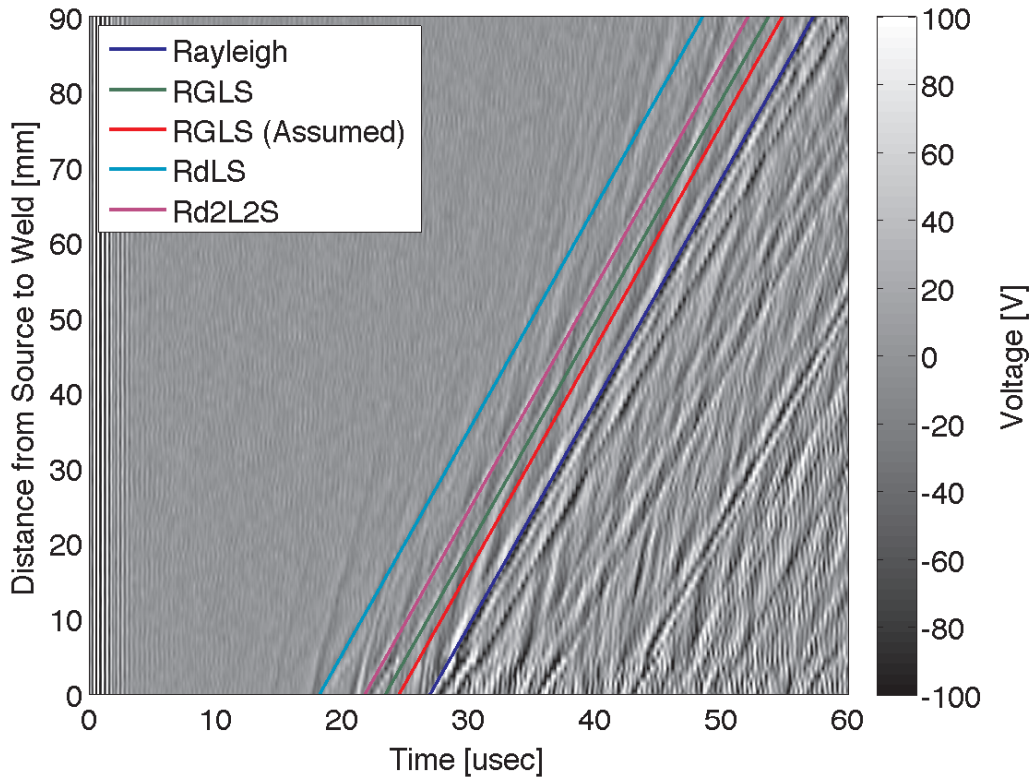

Figure 64: Signals received for various source to weld distances

The received signals show many waves that reach the receiver. Since the distance between the source and weld was varied, the slope of the ridge in the scan can help identify the mode of the wave on the source side of the weld. The waves that travel as a Rayleigh wave are shown by the ridges with a slope equal to the Rayleigh wave speed. The prominent ridges with this slope are identified by the overlain lines. The

Rayleigh wave that travels along the top surface from the source to receiver is clearly seen and correlates with the expected time of flight based on weld geometry. It is the strongest of all received waves. The time of flight of the RGLS wave is shown both for the time of flight-penetration depth relationship assumed in previous works and also when the propagation is as outlined in the previous chapter. This scan representation does not clearly show if waves are present at these times of flight. A better presentation is to shift the time domain signals as defined in Eq. 44 and plot them versus difference from the Rayleigh time of flight as in Figure 65.

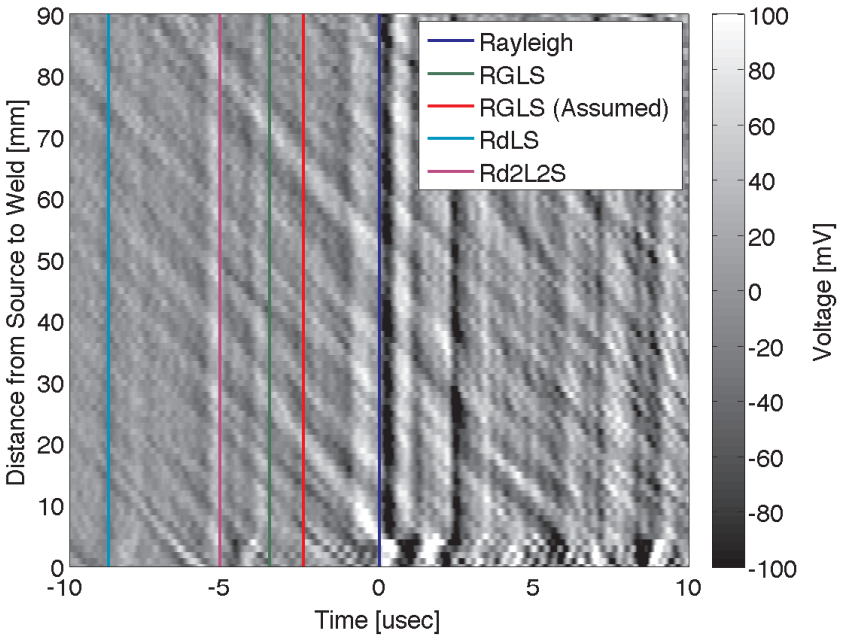

Figure 65: Comparison of RGLS Time of Flight and received signals

This representation clearly shows the waves that travel as a Rayleigh wave on the source side of the receiver as ridges with constant difference from the Rayleigh time of flight. The expected times of flight for the RGLS wave are again shown on the figure. No ridge in the signals correspond to these times of flight. In addition, the RGLS wave should only be seen when the distance from the source to receiver is above the critical distance r_{crit}, 31.3 mm for this plate thickness. Only at distances

above this critical distance can the Rayleigh wave reach the bottom surface. No ridges are present that exist only at distances greater than 31.3 mm. This shows no waves received by the EMAT involve a Rayleigh wave traveling on the bottom of the plate, indicating the RGLS wave is not received by the EMAT. It is possible the square corners of the samples reduce the amplitude of the wave as it travels along the bottom surface and up the weld seam towards the root of the weld bead. It is also possible the gap between the two plates prevents the Rayleigh wave from diffracting at the root of the weld. Both of these possibilities imply the technique may be highly susceptible to joint preparation and geometry. Given this result, a different path must be used. The process to select the best path for this weld configuration is now presented.

5.2 Wave Path Selection

Because the ultrasonic penetration depth method used should be able to work with various types of samples, including samples that have square corners, a different path is needed. In order to determine the dominant ray paths that can be used with this weld configuration, experiments were performed in which the placement of the laser source is varied. The penetration depth of the sample used in these experiments was 2.5 mm. Two configurations were considered. The first configuration places the laser incident location and EMAT on the same side of the weld. In the second configuration, the laser incident location and EMAT were placed on opposite sides of the weld. The first case is depicted in Figure 66. D_{SW} is the distance from the source to the weld and D_{WR} is the distance from the weld to the receiver. There are many paths the ultrasound may follow from the generation point to the receiver. Many of these paths are of no use for penetration depth measurement and only obscure the received signals of paths that may be of use. The paths that may be used to measure penetration depth include those where the wave travels left towards the weld, diffracts

at the crack tip and is received by the EMAT.

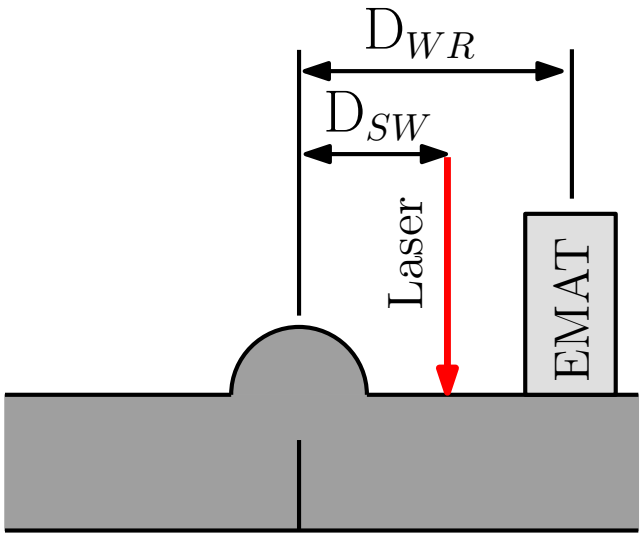

Figure 66: Component placement for experiment

An experiment is performed in which D_{SW} is varied from 5 to 30 mm in 1 mm increments. The distance from the weld to the EMAT is held constant at 51 mm. For each D_{SW}, 20 signals are recorded and averaged. The recorded signals are shown in Figure 67. The dominant waves are identified in Figure 67(b) as the Rayleigh and head waves, the longitudinal waves that are reflected from the bottom of the plate, and longitudinal waves that undergo mode conversion to shear waves. None of these waves interact with the weld and therefore cannot be used to measure penetration depth. Any waves present in the signal that interact with the weld seam must have times of flight that increase as the distance from the source to the weld increases. Waves that travel to the left are indicated by ridges in the scan with a positive slope. However, these waves are obscured by the other waves present in the plate, making time of flight measurements difficult. Therefore, they cannot be used to measure weld penetration depth. The use of a phased array could direct the ultrasound towards the weld root and would increase the amplitude of the wave used to measure penetration depth relative to the other waves present in the plate. However, when using a point

laser source, placing the source and receiver on the same side of the weld is not feasible.

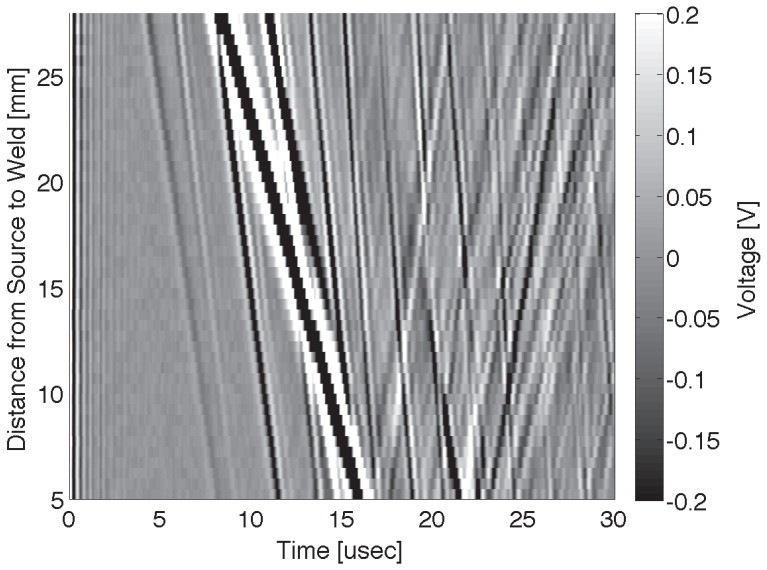

(a)

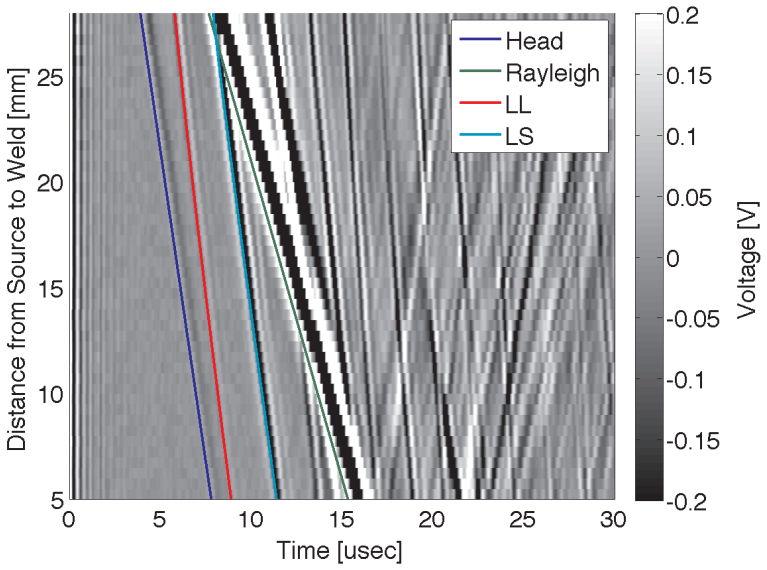

(b)

Figure 67: Signals recorded for various source to weld distances with source and receiver on same side of weld without (a) and with (b) times of flight for various ray paths

The second configuration considered places the laser incident location and EMAT on opposite sides of the weld. The configuration is depicted in Figure 68. The paths that may be used to measure weld penetration depth are those where the wave travels to the crack tip, is diffracted, and reaches the EMAT. An experiment is performed in which D_{SW} is varied from 5 to 40 mm in 1 mm increments. The distance from the weld to the EMAT is held constant at 51 mm.

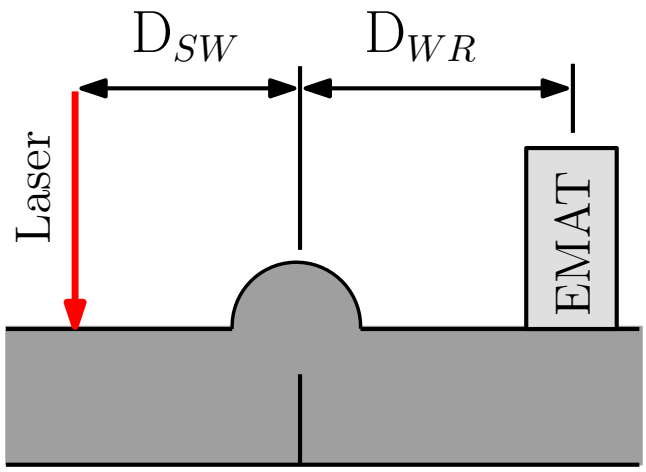

Figure 68: Component placement for experiment

The recorded signals are shown in Figure 69. The dominant waves are identified in Figure 69(b) using the notation described earlier.

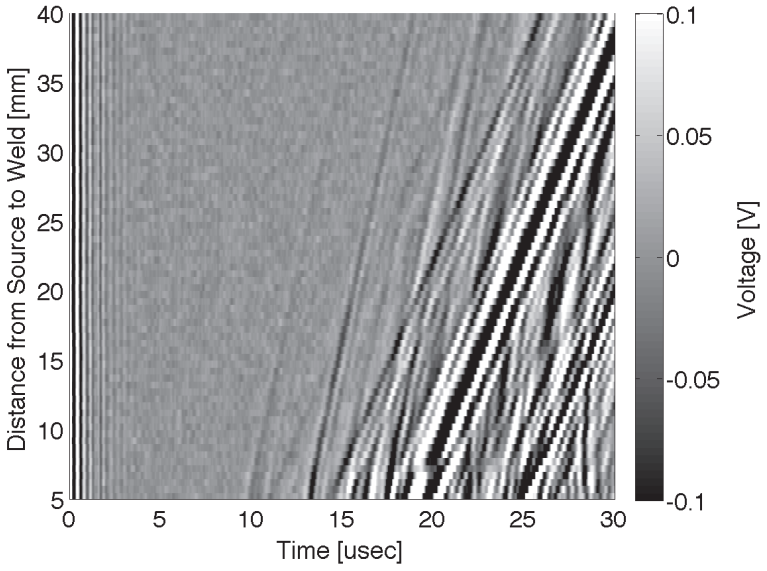

(a)

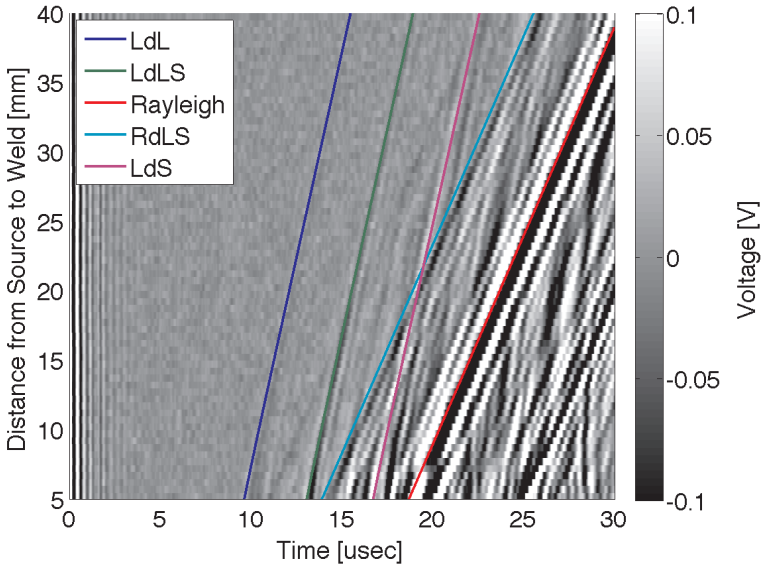

(b)

Figure 69: Signals recorded for various source to weld distances with source and receiver on opposite sides of weld without (a) and with (b) times of flight for various ray paths

Of the waves received by the EMAT, the LdL, LdLS and LdS waves are possible candidates since they are not obscured by other waves. Of these three, the LdLS wave has the largest amplitude and is the most viable candidate. The LdLS path is shown in Figure 70. The laser generates a longitudinal wave that reaches the root of the weld bead. The crack tip causes diffraction to occur and the diffracted longitudinal wave propagates to the bottom surface and undergoes mode conversion to a shear wave that is received by the EMAT.

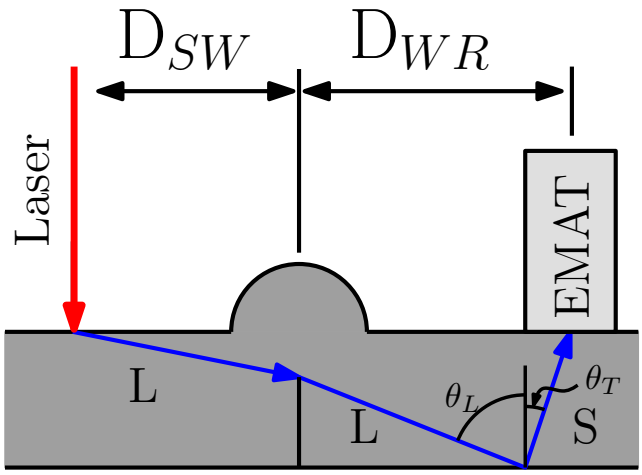

Figure 70: LdLS path chosen for ultrasonic penetration depth measurement

The ToF of the LdLS wave is given in Eq 111:

$$ToF_{LdLS} = \frac{\sqrt{D_{SW}^2 + PD^2}}{C_L} + \frac{T - PD}{C_L \cos\theta_L} + \frac{PD}{C_T \cos\theta_T} \tag{111}$$

$$D_{WR} = (T - PD)\tan\theta_L + PD\tan\theta_T \tag{112}$$

The angles θ_L and θ_T satisfy Snell's law (Eq. 15) and Eq. 112 and must be solved iteratively. In order to ensure the performance of the inspection system is maximized, the optimal placement of the laser incident location and EMAT must be determined to maximize the amplitude of the LdLS wave and to ensure that the wave is not obscured by other received waves.

5.3 Component Placement Optimization

Effective application of the Laser Ultrasonic weld penetration depth measurement system is dependent on proper placement of the various components. The primary concern is to ensure that other waves do not interfere with the LdLS wave. When other waves interfere with the LdLS wave, the time of flight measurement can be adversely affected, increasing the error in the penetration depth measurement. Given that the LdLS wave is received without interference, the second key concern is that the amplitude of the LdLS wave should be as large as possible. The larger the amplitude of the LdLS wave, the better the signal to noise ratio will be for a given noise amplitude. The larger the signal to noise ratio, the less the noise will affect the time of flight measurement.

5.3.1 Determination of Amplitude of Received Rays

The amplitude of laser generated ultrasound can be much weaker and less focused than that generated by PZTs. Therefore, careful consideration of amplitude of the received signal is necessary to maintain an acceptable signal to noise ratio. Amplitude of received ultrasound is dependent on many factors including: directivity of the laser source, directivity of waves diffracted from the crack tip, amplitude of reflection coefficients for any possible reflections in the ray path, attenuation of the wave because of propagation distance, and the directivity of the receiver. The final amplitude of the received signal can be determined by the product shown below in Eq. 113

$$A_f = A_0 \prod (R_i) A_{diff} A_{atten} A_{receiver} \tag{113}$$

where A_0 is the initial amplitude, $\prod(R_i)$ is the product of the reflection coefficients for all reflections in the ray path, A_{diff} is the amplitude of the diffracted wave, A_{atten} is the factor of attenuation (discussed in the next section), and $A_{receiver}$ is the directivity of the receiver. The initial amplitude is determined by the directivity of the laser

source. The directivities for thermoelastic and ablative generation for longitudinal and shear waves are given in Section 2.3. Reflection coefficients were discussed in Section 2.2.1. The directivity of the LURL EMAT used in this research when receiving shear waves is assumed to be proportional to the cosine of the incident angle. The attenuation of ultrasonic waves is strongly dependent on material preparation (cold working, heat treatment, etc.) and is best determined experimentally.

5.3.2 Experimental Measurement of Material Attenuation

As an ultrasonic wave propagates through an elastic medium, attenuation occurs because of energy transformation from mechanical to thermal energies and geometric effects due to spherical or cylindrical wavefront expansion [51]. Attenuation is modeled as an exponential decrease in amplitude as distance travelled increases. Eq. 114 shows this attenuation where A_0 is the initial amplitude, α is the attenuation coefficient, and r is the distance travelled. The parameter α is specified in Nepers per meter (Np/m) where Nepers are a dimensionless quantity.

$$A(r) = A_0 e^{-\alpha r} \tag{114}$$

The factor A_{atten} is then determined to be

$$A_{atten} = \frac{A(r)}{A_0} = e^{-\alpha r} \tag{115}$$

Since attenuation varies with material properties and the particular manufacturing process used to produce the sample, it is necessary to measure the attenuation parameter α in Eq. 113 experimentally. In addition, α is dependent on frequency. However, for this work it is sufficient to specify an overall attenuation coefficient since the frequency characteristics of the laser ultrasonic source are constant.

The experimental setup was as follows. Ultrasound was generated on the surface of four different plates via ablative generation. The laser was configured to output 45

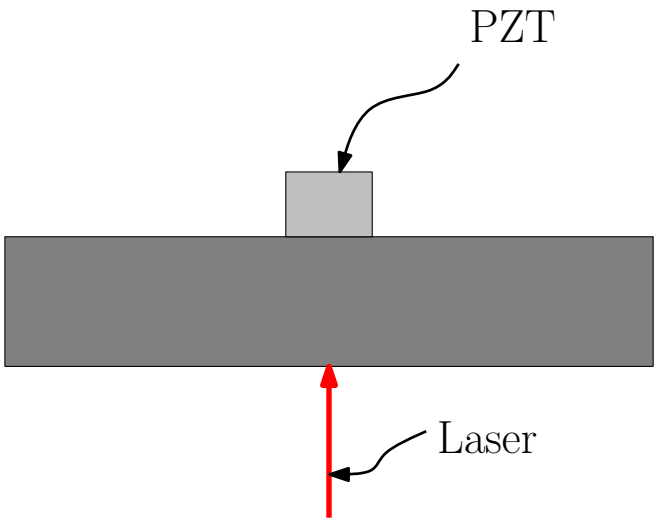

Figure 71: System configuration for measurement of material attenuation

mJ per pulse. The thicknesses of the plates were 12.6, 15.7, 19.0 and 25.4 mm. A PZT was placed on the opposing surface, coaxial with the source. The sound propagated and repeatedly reflected off the two surfaces of the plate, with each received signal lower in amplitude than the last. At normal incidence to a free surface, the reflection coefficient for longitudinal waves is equal to -1. Thus, the amplitude decrease was only due to material attenuation. The received signal for the 12.6 mm thick plate is shown below in Figure 72. The signal shows the multiple back wall reflections, each subsequent reflection having lower amplitude than the previous.

In order to determine the amplitude of each reflected wave, the longitudinal waves were isolated from the rest of the signal. A 2.8 μs long rectangular window was applied to the signal starting at the theoretical time of flight for each back wall reflection. The amplitudes of the resulting windowed signals were then calculated. The measured amplitudes and travel distances for all four samples were combined into one data set and an exponential fit was performed. The attenuation was determined to be 16.95 Np/m. Figure 73 shows the measured amplitudes versus distance traveled along with the exponential fit. The RMSE error for the fit is 0.0865 V.

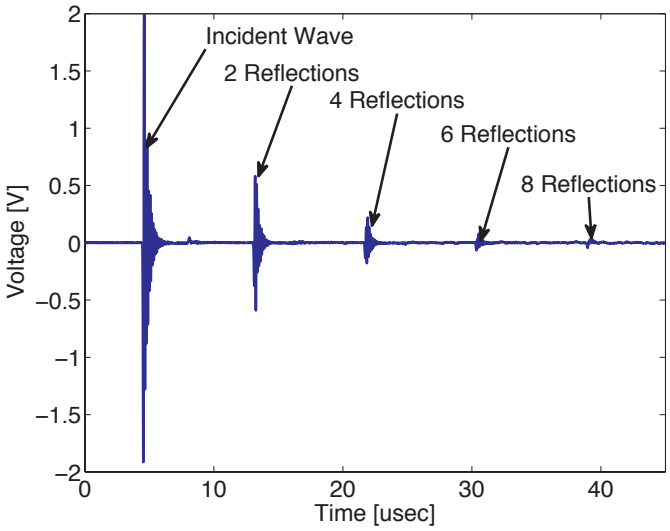

Figure 72: Signal recorded by PZT for measurement of material attenuation

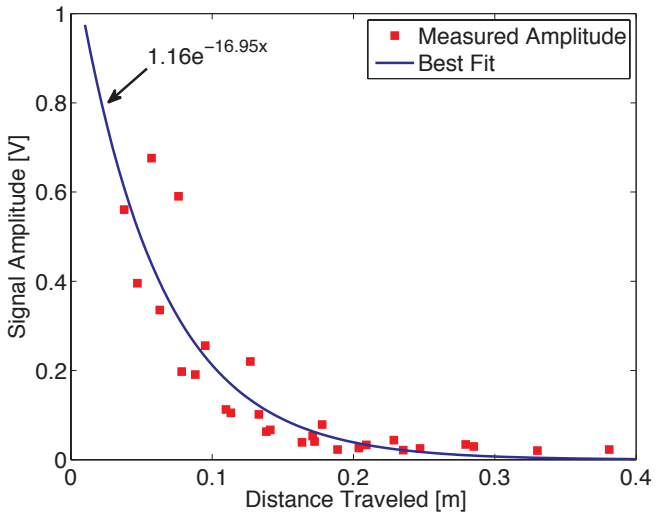

Figure 73: Measured amplitudes versus distance travelled

5.3.3 Experimental Verification of Diffraction Potentials

The diffraction of laser generated ultrasound by slots and fatigue cracks was considered by Ravenscroft et al. [50]. In this work, it was shown that the amplitude of diffracted wave potentials for plane harmonic waves closely approximate the amplitude of laser ultrasonic waves diffracted at slots and fatigue cracks. In order to verify the theoretical diffraction potentials presented in Section 2.2.3 accurately predict the amplitude of waves diffracted by the crack located at the root of the weld, an experiment was performed. A laser generated ultrasound 27.6 mm from the weld seam of a 12.6 mm thick welded specimen. An Olympus NDT C110-RM piezoelectric transducer with center frequency equal to 5 MHz and 12.6 mm element diameter was used to receive the ultrasound. The PZT was placed on the back surface on the opposite side of the specimen to receive the ultrasound diffracted from the crack at the weld seam. A schematic of the experimental setup is shown in Figure 74. The PZT was located at locations 9.5, 12.6, 14.5, 16.1, 17.6, 20.2, 22.0, 23.8, 25.8, 27.9, and 30.1 mm from the weld seam. For each location, 100 signals were acquired and averaged.

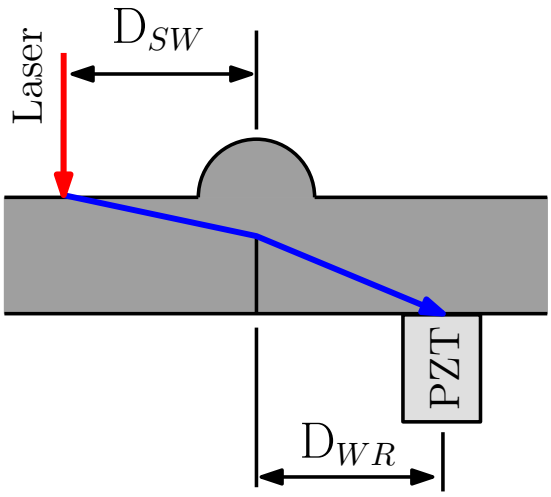

Figure 74: System configuration for crack diffraction validation

The signals received by the PZT are shown in Figure 75, where DC offsets have

been added to the signals for presentation. The amplitudes of the diffracted longitudinal waves were calculated and then multiplied by the cosine of the reception angle as a corrective factor to account for the directivity of the PZT.

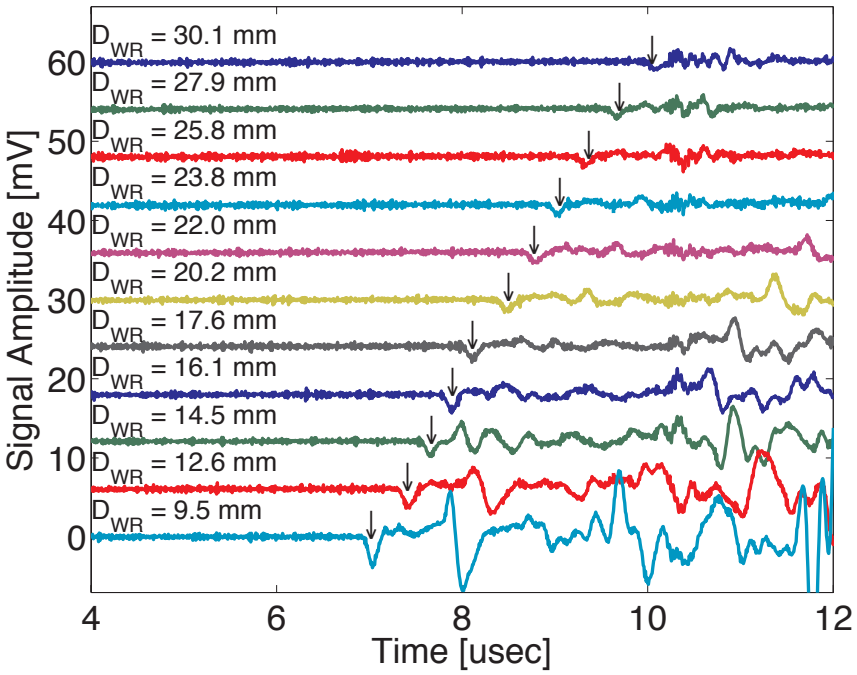

Figure 75: Signals received by the PZT. Arrows indicate the time of flight of the diffracted longitudinal waves.

The amplitude of the diffraction potential and the measured amplitudes are shown in Figure 76. The diffraction potential amplitude has been normalized to be comparable to the measured amplitudes. There is very good agreement between theoretical amplitude and the measured amplitudes and the RMSE is 0.118 mV. The results show that the diffraction potentials presented earlier sufficiently describe the amplitude of laser generated ultrasound diffracted by crack located at the root of the weld. The amplitude of received ultrasound may now be predicted by Eq. 113.

With the factors needed in Eq. 113 determined, the amplitude of the received ultrasound can be calculated for various source and receiver placements. The configuration that yields the largest amplitude without interference from other waves can

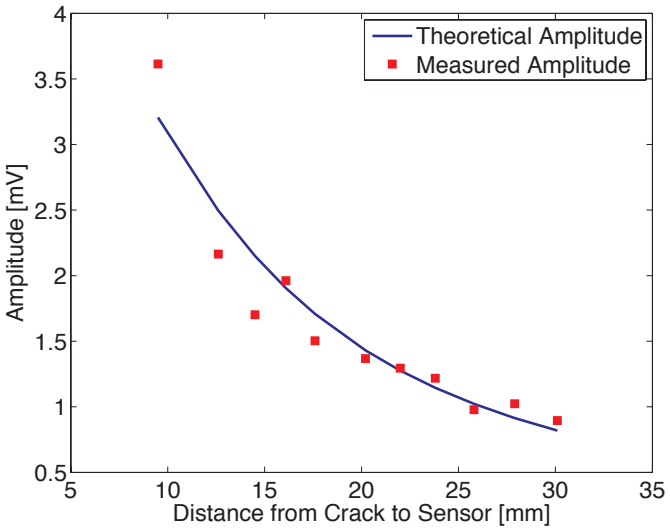

Figure 76: Measured and theoretical diffracted wave amplitude

be found.

5.3.4 Determination of Optimal System Component Placement

The amplitude of the received LdLS wave is calculated according to Eq. 113 for source to weld distances ranging from 20 to 40 mm, weld to receiver distances ranging from 20 to 40 mm, and penetration depth ranging from 0 to 6 mm. The initial amplitude is assumed to be unity. The source to weld and weld to receiver distances are so chosen because of placement restraints caused by weld reinforcement geometry and the size of the EMAT and beam delivery optics. A maximum penetration depth equal to 6 mm is used since the literature indicates that the maximum penetration depth obtainable by conventional GMAW equipment is approximately 5.7 mm [20]. For each combination, the times of flight of the LdLS and other waves are calculated. For some combinations of source and receiver placement, interference between the LdLS wave and other waves may occur. If the difference between the LdLS time of flight and the time of flight of any other wave is less than 1.2 μs, the D_{SW} and D_{WR} pair is deemed unacceptable. 1.2 μs is used based on experimentally measured signal duration. If the configuration is acceptable, the mean amplitude of the LdLS wave over the penetration depth range

0-6 mm is calculated. Figure 77 shows the normalized mean amplitude versus D_{SW} and D_{WR} as in the color bar. The region where no amplitude is shown corresponds to locations where interference occurs. There are two waves that interfere with the LdLS wave, the RdLL wave and the LS path. The RdLL wave will interfere with the LdLS wave when the distance from the source to the weld is too small. The LS wave will interfere with the LdLS wave when the crack no longer blocks the LS wave from reaching the receiver.

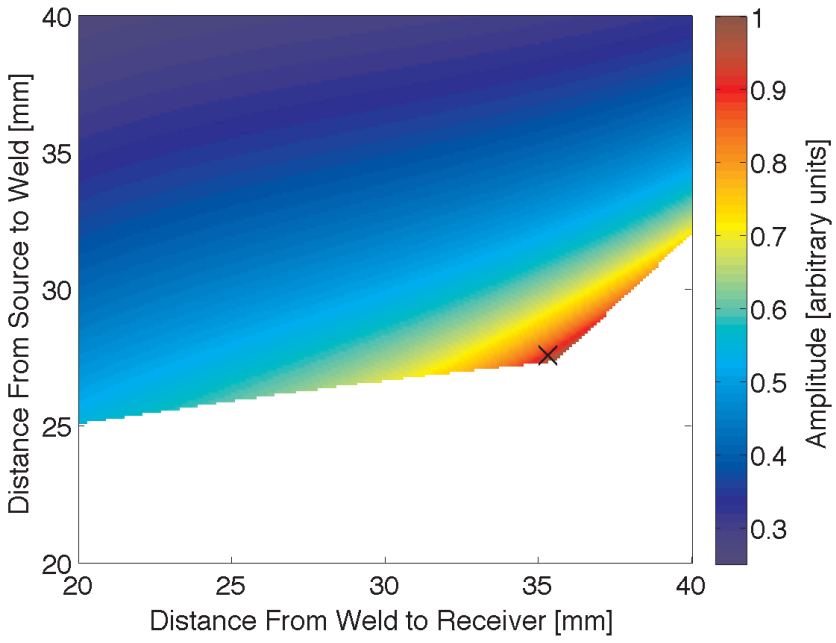

Figure 77: Amplitude versus D_{WR} and D_{SW}

The largest amplitude where no interference occurs is found for $D_{WR} = 35.3$ mm and $D_{SW} = 27.6$ mm. As stated earlier, the amplitude of the received wave is dependent on multiple factors. The dominating factor is the diffraction of the initial longitudinal wave at the crack tip located at the root of the weld. Figure 78 shows the amplitude of the diffraction potential for an incident longitudinal wave at 96.3° (corresponding to $D_{SW} = 27.6$ mm and penetration depth equal to 3 mm).

The diffraction potential is maximum diffracted angles 83.7° and 263.7°. The

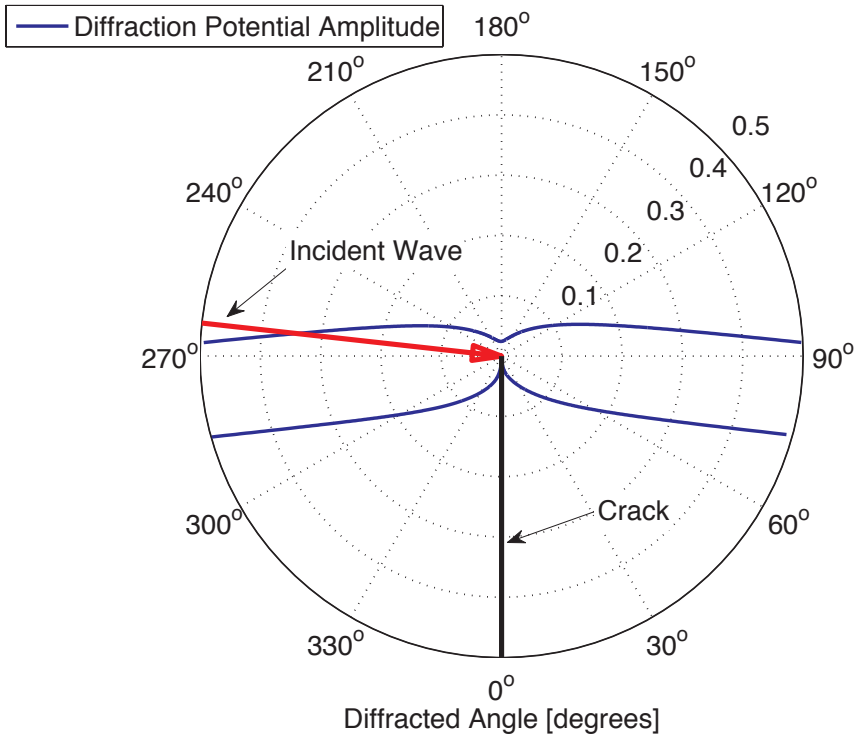

Figure 78: Amplitude of diffraction potential for incident and diffracted longitudinal waves 20 mm from the crack tip

diffracted longitudinal wave in the LdLS path travels down to the bottom surface of the plate. Therefore, the diffracted angle should be as close to 83.7° as possible while preventing other waves from interfering with the LdLS wave. This explains why the amplitude of the received wave is greater for larger weld to receiver distances.

In order to determine the performance of the weld penetration depth measurement technique, the inspection system was configured with the distances determined above and used to inspect a welded specimen. The specimen was created using the same wire feed rate input as earlier (see Figure 58). The recorded signals are shown below in Figure 79. The LdLS wave is indicated by the arrow in the figure. No interference occurs and the signal to noise ratio for for the LdLS wave is approximately 9.65 dB.

The penetration depth was measured by measuring the time of flight at each measurement location and determining the penetration depth from Eq. 111. The time

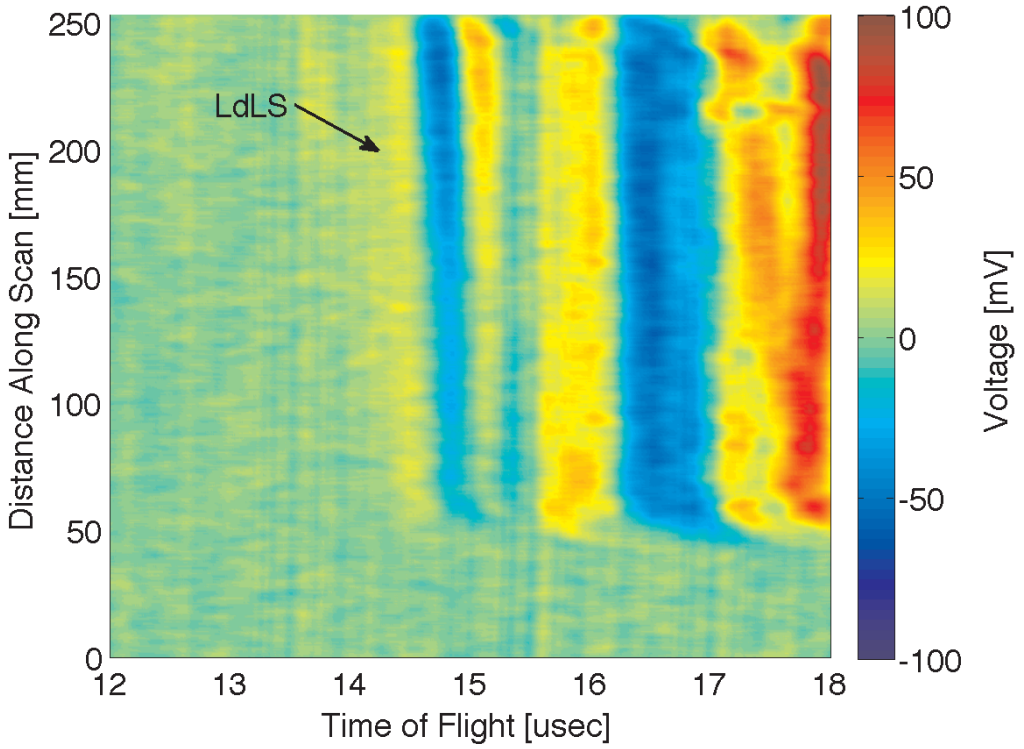

Figure 79: Signals recorded by the EMAT used to validate the LdLS time of flight technique

of flight was measured using the cross-correlation technique [5, 26, 40]. The biased cross-correlation of signal $x(t)$ and reference signal $x_{ref}(t)$ defined for $0 \leq t \leq T$ is $\hat{R}(\tau)$, as defined below in Eq. 116

$$\hat{R}(\tau) = \frac{1}{T - |\tau|} \int_0^{T-\tau} x_{ref}(t)x(t+\tau)dt \tag{116}$$

The time delay between the two signals is determined by locating the maximum of the cross-correlation. In this way, if the time of flight of the reference signal is known, the time of flight of the measured signal x is determined by adding the delay to the reference time of flight.

Penetration depth measured using the ultrasonic system is plotted versus the penetration depth obtained via destructive cut checks is shown in Figure 80. The

root mean square error (RMSE) of the ultrasonic measurement is 0.28 mm. The system performs well and is able to measure penetration depth at room temperature. However, to effectively operate during welding, the error caused by the thermal profile of the samples must be reduced as is discussed in the next chapter.

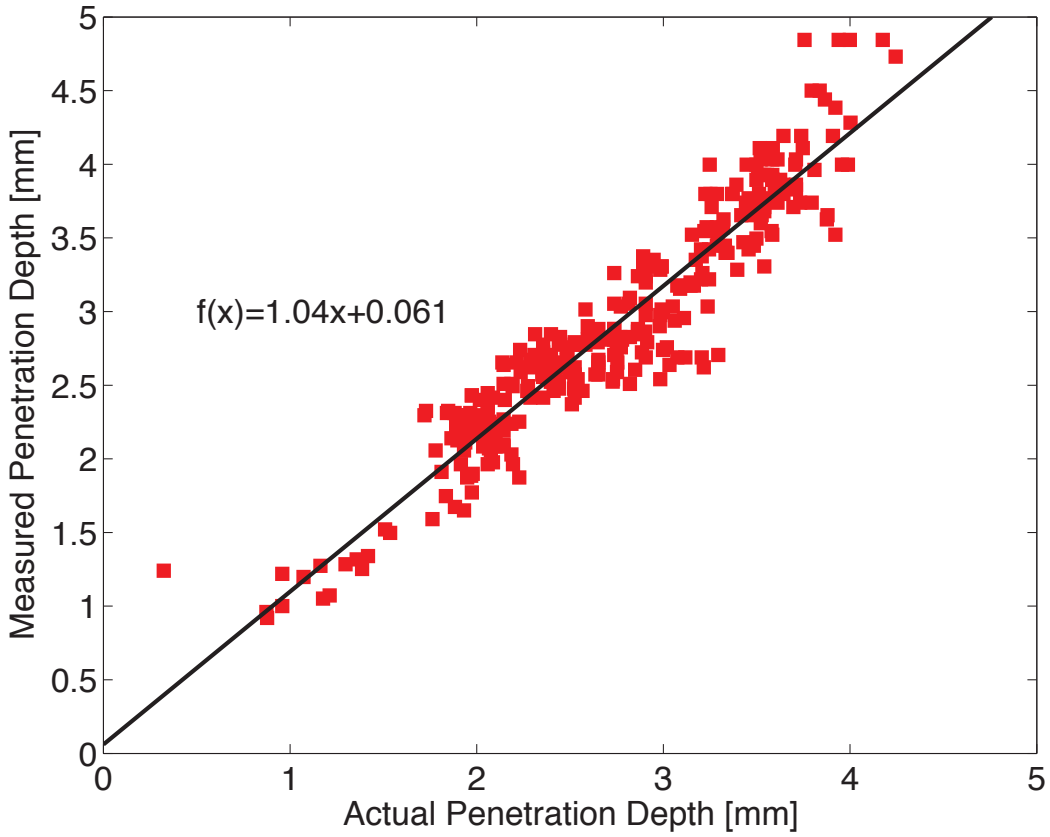

Figure 80: Penetration depths measured using ultrasonic inspection and cut checks

CHAPTER VI

NEURO-FUZZY MODELS FOR TEMPERATURE INDUCED ERROR COMPENSATION AND DESTRUCTIVE MEASUREMENT PREDICTION FOR IN-PROCESS WELD INSPECTION

Previous research has shown that ultrasonic techniques can measure penetration depth during welding. However, penetration depth measurement error is introduced by the presence of elevated temperatures and large thermal gradients during welding. The increased temperatures cause the wave speeds of the various wave modes to decrease. A nonuniform temperature field causes the path followed by the ultrasound to differ from the room temperature path according to Fermat's principle. This principle states that the ray path followed by ultrasound is the path that corresponds to a minimal time of flight. For nonuniform temperature fields, the path the ultrasound follows may be curved. Because of the changes in wave speed and path length, error is introduced when the penetration depth is calculated using a time of flight/penetration depth relationship that assumes the sample is at room temperature.

Previous works have determined the changes in time of flight due to the temperature field using a three dimensional ray tracing algorithm. The ray path from the source to the receiver was determined using temperature field data determined by a finite element model. The ray path was then determined using a shooting algorithm. The analysis was performed for constant welding parameters and showed good results. If the welding parameters are time-varying, as in the case of a controlled system, the temperature field may not be accurately determined by a constant parameter finite element model. The finite element model would have to be run concurrently during

welding using the actual welding parameters applied during the weld. Since such a model is very computationally intensive, a different approach is needed. In this chapter, a nonlinear dynamic modeling approach is investigated in which penetration depth is predicted by neuro-fuzzy inference systems using in-process time of flight measurements and input welding parameters.

6.1 In-Process Weld Penetration Depth Measurement

During welding, the torch transfers heat to a small region at the weld seam that travels with the torch. The temperature field due to this heat input varies with time. After the torch passes a given location, the heat present near the weld bead diffuses away from the seam. The distance from the torch to the sensor, D_{TS} affects the nature of temperature field through which the ultrasound travels. This torch to sensor distance is illustrated in Figure 81. If the inspection system is placed close to the torch, the temperature field the ultrasound propagates through has a large peak temperature with large temperatures near the weld bead. If the sensing system is placed further behind the torch, the peak temperature will be less and the heat will have propagated further from the weld bead.

Experiments were performed in which the weld was inspected during and after welding. During welding the wire feed rate was varied to change the penetration depth and temperature field. The sensing system was placed at five different torch to sensor distances: 32, 38.5, 45, 51 and 56 mm. At each torch to sensor distance, two samples were welded and inspected except for $D_{TS} = 38$ mm, where only one sample was inspected. Previous work showed the minimum torch to sensor distance at which ultrasound is able to pass through the solidified weld to be approximately 25 mm [39]. The system was configured as shown in Figure 82.

The Wire Feed Rate (WFR) was programmed to follow the sequence shown in Figure 83. This sequence consists of a constant 400 in/min followed by a 2 period

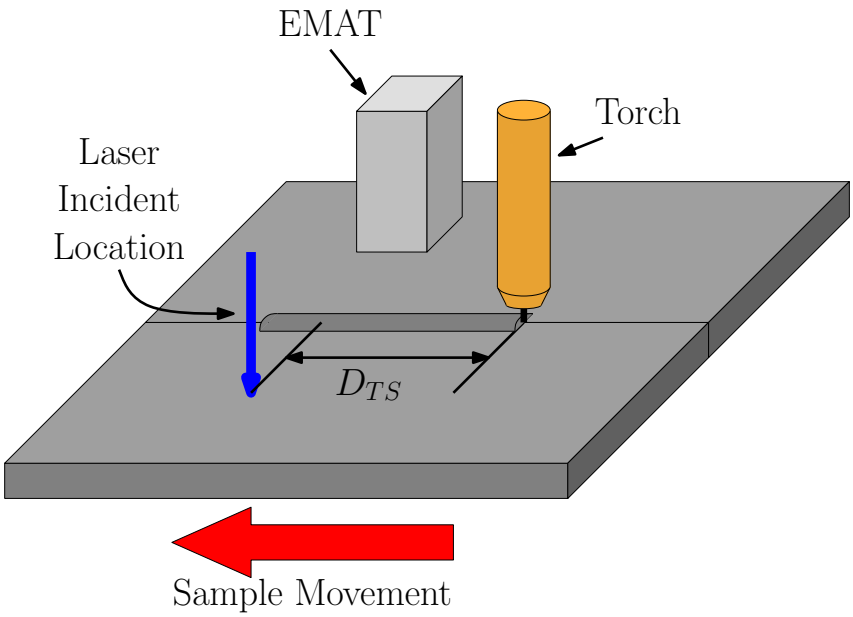

Figure 81: Definition of Torch to Sensor distance D_{TS}

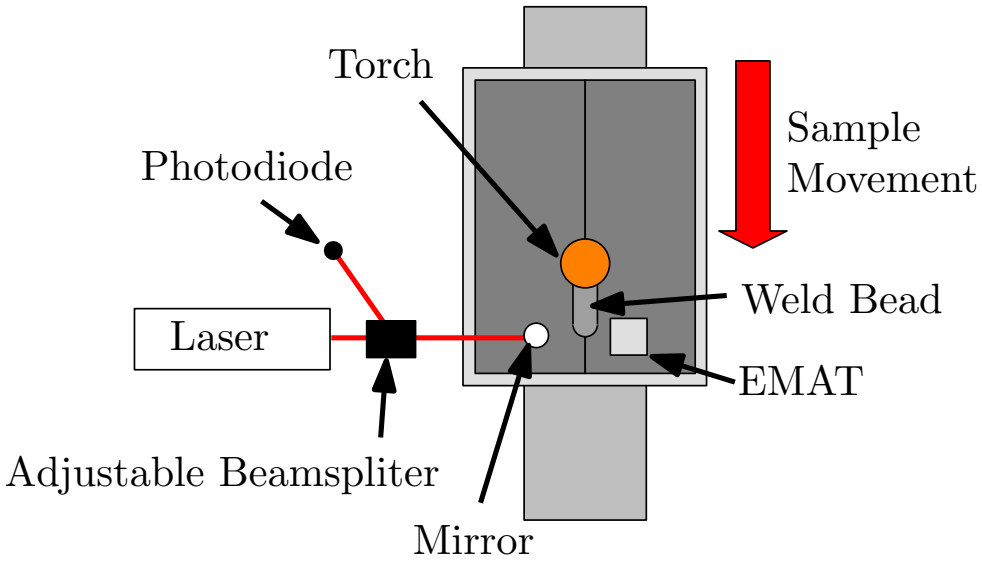

Figure 82: System configuration for in-process penetration depth measurement

sinusoid and a multi-level pseudo random sequence. The initial constant input was used to allow the system to reach equilibrium. The sinusoidal input was used to provide a way to estimate the oscillation in penetration depth during a slowly varying

input. The multi-level pseudo random sequence was used because it has been shown to be an effective input sequence for identification of nonlinear systems and useful for development of the error compensation model.

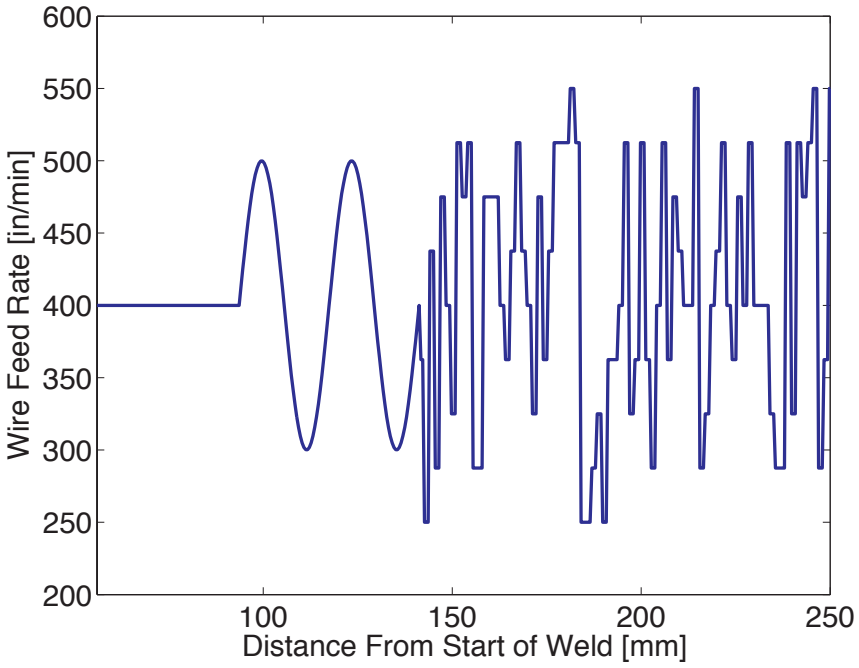

Figure 83: Commanded wire feed rate for compensator development

The penetration depth along the weld path was calculated for all samples using destructive cut checks as described in Chapter 5. The penetration depths are shown in Figure 84 where offsets have been added for presentation. The penetration depths are fairly consistent, but vary from sample to sample. This can be explained by variation in the welding process due to the age of the welding equipment.

While welding occurs, ultrasonic data is recorded each time the laser was fired. The laser was fired with a 20 Hz repetition rate and was synchronized with the actuation signal. After welding, the sample was allowed to cool to room temperature. The system then scanned the sample at the same locations as were measured during welding. At each location, the laser was fired 20 times and the signals averaged to increase the signal to noise ratio. In order to reduce the influence of noise on the

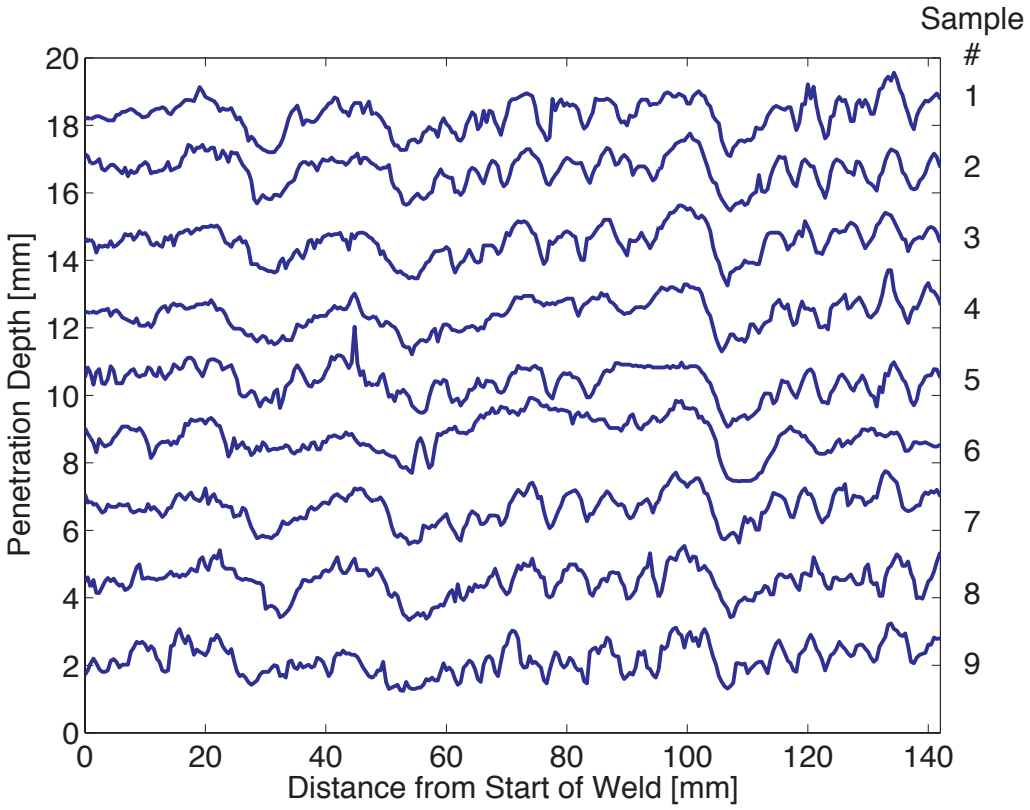

Figure 84: Weld penetration depth measured destructively (offsets added for presentation)

ToF measurement, the signals were filtered in software by a band pass FIR equiripple filter. Since the filter is linear phase, the group delay of the filter is constant and was compensated in software and does not affect the ToF measurement. The filter was created using the MATLAB fdatool filter design tool with the following parameters: first stop frequency = 0.4 MHz, first pass frequency = 0.6 MHz, second pass frequency = 2.0 MHz, and second stop frequency = 2.3 MHz. 6% ripple is specified for the pass band. The filter frequency response is shown below in Figure 85(a) and an unfiltered and filtered signals are shown in Figure 85(b).

The pass and stop frequencies were determined by matching the frequency characteristics of the received ultrasound. In this way, the amplitude of the received

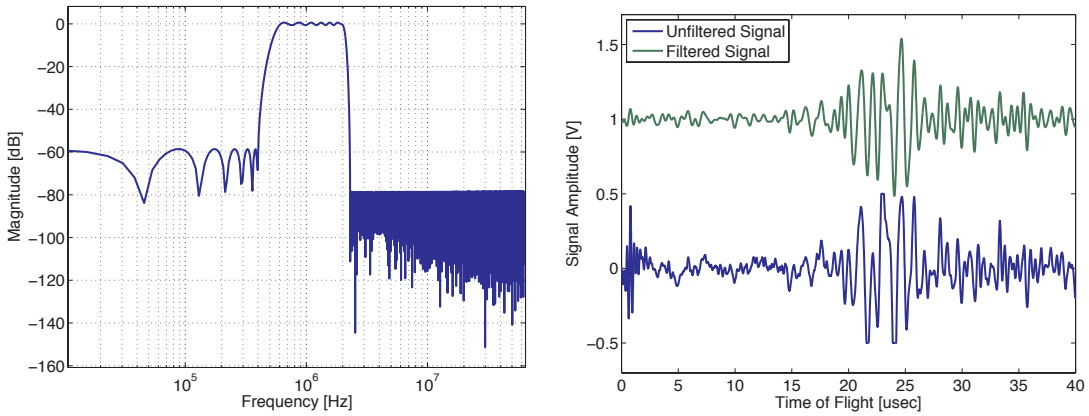

(a) (b)

Figure 85: (a) FIR equiripple filter frequency response and (b) unfiltered and filtered signals

ultrasound is minimally affected and the noise amplitude is reduced. The filtered in-process and offline data recorded for $D_{TS} = 56$ mm behind the torch are presented in Figures 86 and 87, respectively. In the figures, the abscissa represents time of flight, the ordinate is the distance from the start of the scan, and color indicates signal voltage as shown in the color bar.

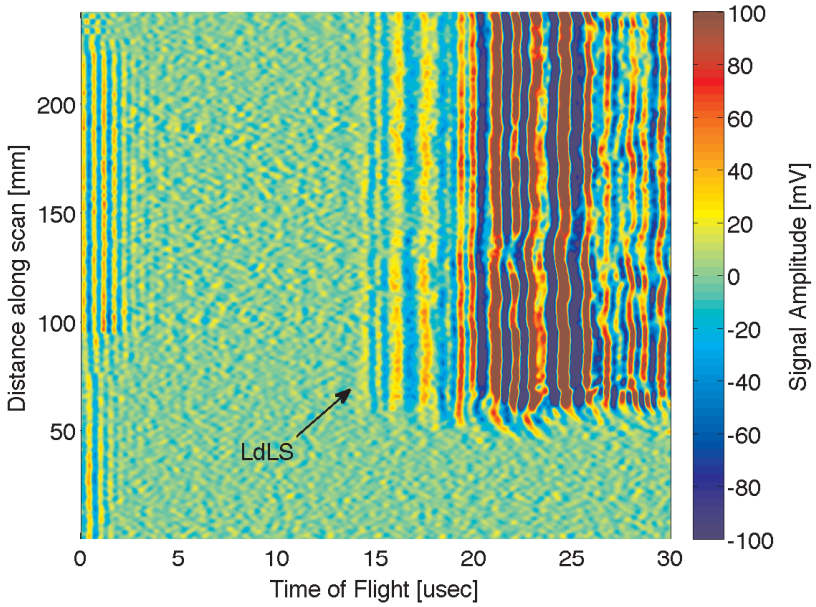

Figure 86: Filtered signals recorded during welding, $D_{TS} = 56$ mm

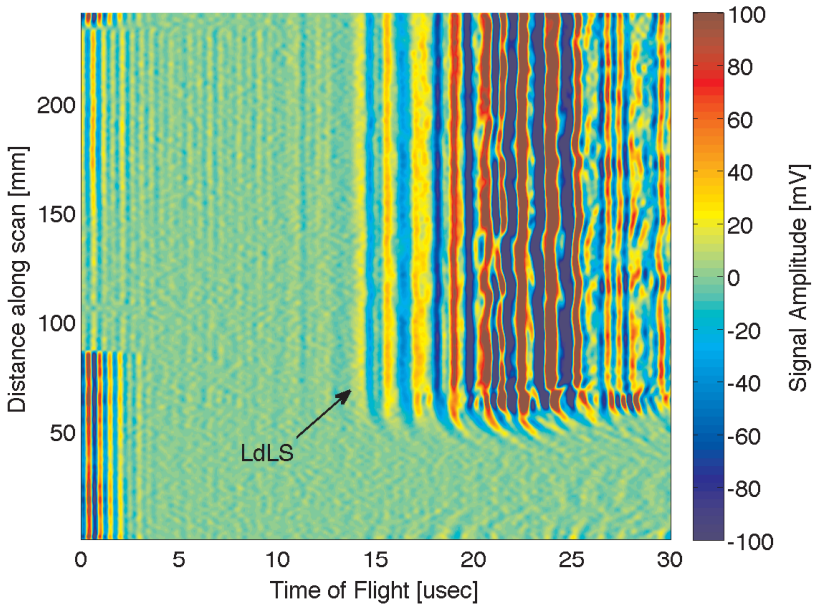

Figure 87: Filtered signals recorded at room temperature, $D_{TS} = 56$ mm

The signals recorded during welding have a significantly larger noise amplitude and the various waves arrive later than those recorded at room temperature. This is due to the decrease in wave velocity as temperature increases. Scruby measured the longitudinal and shear wave velocities for mild steel over a temperature range of 17-1200 C. Over this temperature range, the longitudinal wave speed varies by up to 17% from 5923 to 4913 m/s and the shear wave velocity differs by up to 28% from 3190 to 2290 m/s [55]. The measured wave speeds are monotonically decreasing with increasing temperature. These changes in wave speed affect the relationship between measured ToF and penetration depth, introducing an error in the measured penetration depth if the relationship in Eq. 111 is used.

The signals recorded during and after welding at 72 mm into the path for $D_{TS} = 56$ mm are shown in Figure 88. The dashed and solid vertical lines indicate the time of flight of the LdLS wave recorded after the sample cools down to room temperature and recorded during welding, equal to 14.36 and 14.24 μs respectively. The change

in time of flight is relatively small. However, small changes in time of flight will introduce large errors in penetration depth measurement.

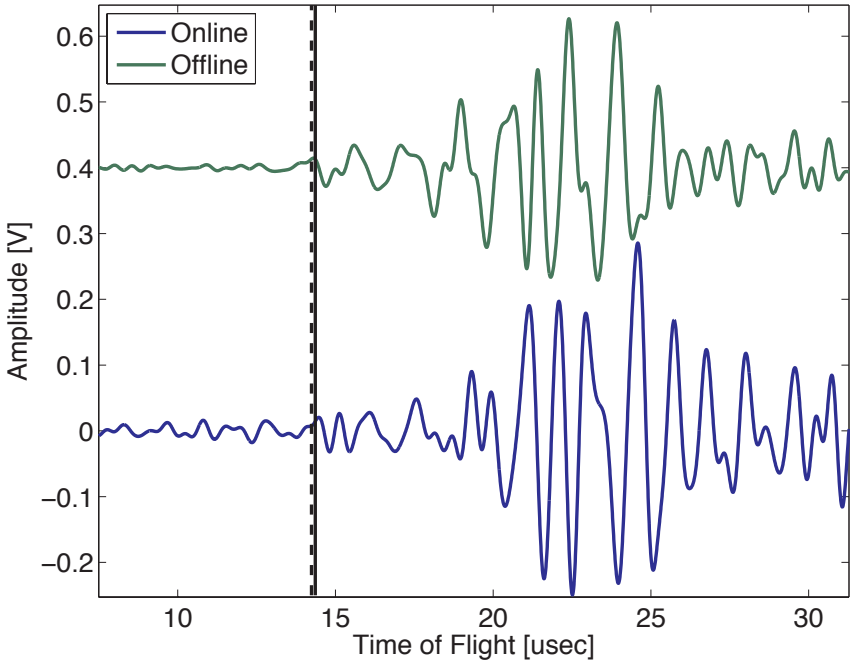

Figure 88: Signals recorded at 72 mm along the scan during and after welding. Dashed and solid vertical lines indicate offline and in-process time of flight, respectively.

The Root Mean Square (RMS) differences in time of flight for the entire length of the weld were calculated for the five torch to sensor distances. Figure 89 shows the RMS difference versus D_{TS}. The RMS difference in time of flight tends to decrease as the torch to sensor distance increases. This is corroborated by previous research. For the sample inspected with $D_{TS} = 38$ mm, the difference is lower than any other distance. This is because of a larger noise amplitude for these received signals that reduces the performance of the time of flight measurement.

As described earlier, the differences in time of flight affect the penetration depth measurement. The RMS offline and in-process times of flight for a sample inspected with $D_{TS} = 56$ mm are 14.26 and 14.40 μs, respectively. If the penetration depth is calculated based on the in-process time of flight, the result is -2.45 mm. Thus, the

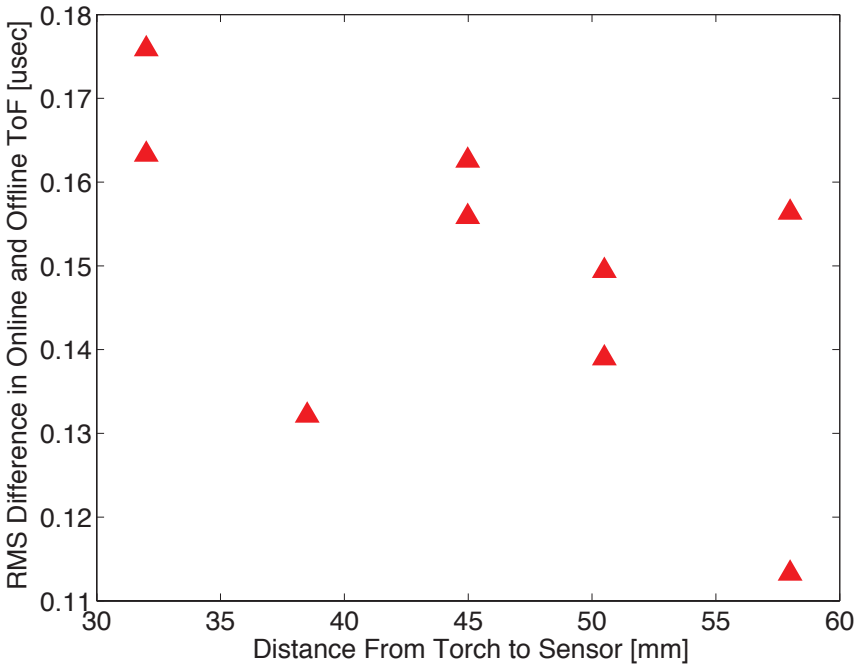

Figure 89: RMS difference in times of flight recorded during and after welding

amplitude of the change in time of flight due to the temperature field is too large to allow this torch to sensor distance to be used for in-process weld inspection without compensating for the change in time of flight.

The difference in time of flight can be decreased by increasing D_{TS}. However, the increased distance causes a larger time delay between actuation by the torch and measurement by the sensing system. For control systems, increasing delay between actuation and measurement may reduce the stability margin of the controlled system. For the ultrasonic penetration depth measurement technique to be applied to weld quality control, the delay should be minimized while at the same time minimizing the measurement error. In order to accomplish this, models were developed to predict penetration depth based on in-process measurements.

6.2 Neuro-Fuzzy Penetration Depth Prediction Models

In order to accurately model the error in time of flight due to the temperature field present during welding, a data driven nonlinear modeling approach was taken. Such approaches are commonly referred to as "black box" models. The data that is available for model development dictates the modeling process. In practice, two scenarios are of interest. In the first scenario, destructive penetration depth measurements are not possible. In this case, the automatic weld inspection system is used during welding to obtain an in-process time of flight measurement and then the system inspects the weld again after it has cooled to room temperature. The recorded times of flight can be used to model the error introduced by the temperature field present during welding. The predicted error can be subtracted from the in-process time of flight and the penetration depth can then be calculated using Eq. 111. In this scenario, any penetration depth error present in the offline measurement will not be removed by the model. Alternatively, if destructive penetration depth measurements are available, the model can be trained to output the penetration depth directly from the in-process time of flight and the welding input parameters. This may be possible when inspection is performed in an assembly line setting where parts are pulled from the line for destructive off-line inspection. Both of these scenarios are now considered.

6.2.1 ToF Error Compensation Model

Since the temperature field within the sample is dependent on the welding parameters, a model was developed that relates the time history of the welding input parameters and the measured time of flight to the error introduced by the temperature field. The error compensation scheme is shown schematically in Figure 90.

The time of flight error produced by the model was then subtracted from the in-process ToF measurement to yield the model ToF. Eq. 111 was then used to calculate the model penetration depth. The goal of the error compensation model is

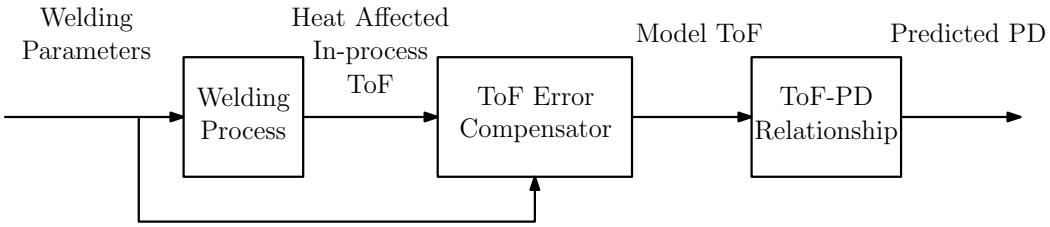

Figure 90: Temperature induced error compensation block diagram

to produce an in-process measurement with performance that is comparable to the offline ultrasonic penetration depth measurement.

In order to capture the effects of the welding parameters on the error, the WFR was included as input to the model. However, since the WFR at a particular point in the welding path contributes to the temperature at locations both before and after the torch, the wire feed rate was preprocessed by filtering it with a moving average filter. Thus, the model takes in the average of the wire feed rate at a particular location and 10 neighbors to either side (a total length of 9.5 mm) as given in Eq. 117. This length of filter was used to emulate the distribution of heat input below the torch. Note that causality is ensured even though this includes the WFR at points later in the weld because of the delay introduced by placing the sensor behind the torch.

$$WFR_{avg}(k) = \frac{1}{21}\sum_{k-10}^{k+10} WFR(k) \tag{117}$$

Where:

WFR	Wire feed rate
WFR_{avg}	Averaged wire feed rate
k	Time step index

To train the model, the ANFIS routine included in the MATLAB Fuzzy Logic

Toolbox was used. The hybrid training algorithm was used because of its computational efficiency. For a description of ANFIS, see [28]. First, the difference in ToF between the offline and in-process ToF measurements was calculated as defined in Eq. 118 and used as the neuro-fuzzy system target output. This difference will be negative because the in-process ToF measurement will be larger than the offline ToF measurement.

$$\Delta ToF = ToF_{offline} - ToF_{in-process} \tag{118}$$

Neuro-fuzzy systems can have many inputs and outputs. However, ANFIS is limited to systems with a maximum of four inputs and one output. The ability of the system to accurately model the process is affected by the number of inputs and membership functions. Therefore, it was necessary to determine the inputs that maximized performance and the number of membership functions per input. The in-process ToF measurement was included as an input to the model for all the cases. The other inputs were selected from six possible choices: the averaged wire feed rate for 0, 0.25, 0.5, 0.75, 1.0, and 1.25 s earlier in the welding process i.e. $WFR_{avg}(t), WFR_{avg}(t-0.25), WFR_{avg}(t-0.5), ..., WFR_{avg}(t-1.25)$. These quantities correspond to measurement locations 0.0, 2.4, 4.8, 7.14, 9.5 and 11.9 mm before the current measurement location.

In order to determine the most appropriate inputs, a search was performed in which the model is trained for combinations of inputs so that the in-process ToF measurement is included as the first input and no inputs are repeated. The cases of two and three inputs are considered. When two inputs are used, the system can be considered quasi-steady state since one time instance of the wire feed rate is included. Quasi-steady state thermal models of the welding process have been used by other researchers with good results. It is possible that a quasi steady state model may be sufficient to model the difference in ToF due to the temperature field. However, a dynamic model may yield better performance. Dynamic models were created by

increasing the number of inputs to include additional delayed WFR values.

Two through four generalized bell membership functions are used for all inputs. The number of rules increases exponentially with the number of inputs and is calculated by raising the number of membership functions to a power equal to the number of inputs. Each rule has an associated output function with a number of parameters one more than the number of inputs. Clearly, as the number of inputs and membership functions increase, the number of parameters that must be determined increases rapidly.

For each structure and sample, the FIS was trained using experimentally obtained data. In order to ensure the model is not over fit to the data, the model was used to predict the difference in ToF for an additional sample with the same D_{TS} at each training iteration. The data corresponding to this additional sample is called the checking data. This provides a means to validate the model and ensure the model represents the physical process that causes the ToF error rather than noise or other disturbances present in the training data set. The exception is the one sample with $D_{TS} = 38$ mm. Because there is no other sample with this torch to sensor distance, no checking data was used. The hybrid training algorithm was applied to the FIS iteratively. Each iteration is called an epoch. At each epoch, the model RMS training and checking errors were calculated for the training and checking data. The set of parameters that produced the lowest checking RMSE was selected. Figure 91 shows the training and checking RMSE for Sample 1 for 1-400 training epochs where Sample 2 is used as checking data. The training RMSE dropped slowly as training progressed, but the checking RMSE increased drastically. This indicates the model is training to the noise present in the data set rather than the physical process.

The RMS training and checking errors were calculated for each sample and combination of inputs and number of membership functions. Figure 92 shows the error for each combination organized by structure. The errors for the nine samples are stacked

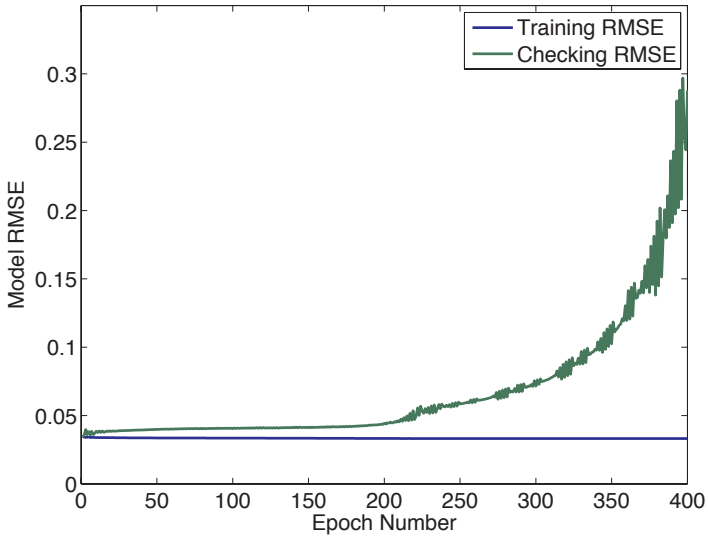

Figure 91: Model RMSE versus training epoch for Sample 1

to show the total error for each structure. The training errors are comparable between the different structures with the best performing structure having three inputs and four membership functions. However, this same structure was found to have the largest checking error of all structures. This is most likely because of the large number of parameters in this structure when compared with the others. This structure has 64 rules, each with four parameters and twelve membership functions, each with three parameters for a total of 292 parameters. The best performing structure has three inputs and two membership functions where the sum of the training and checking errors was the lowest of all structures. This structure only has 50 parameters. The large number of parameters for the models with more membership functions may cause the large checking error.

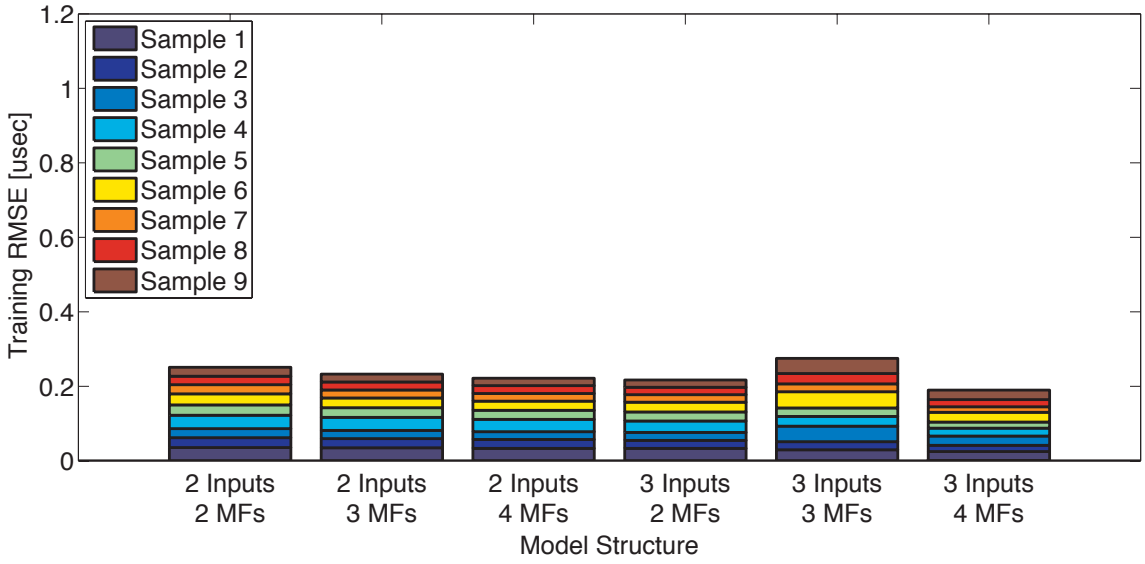

(a)

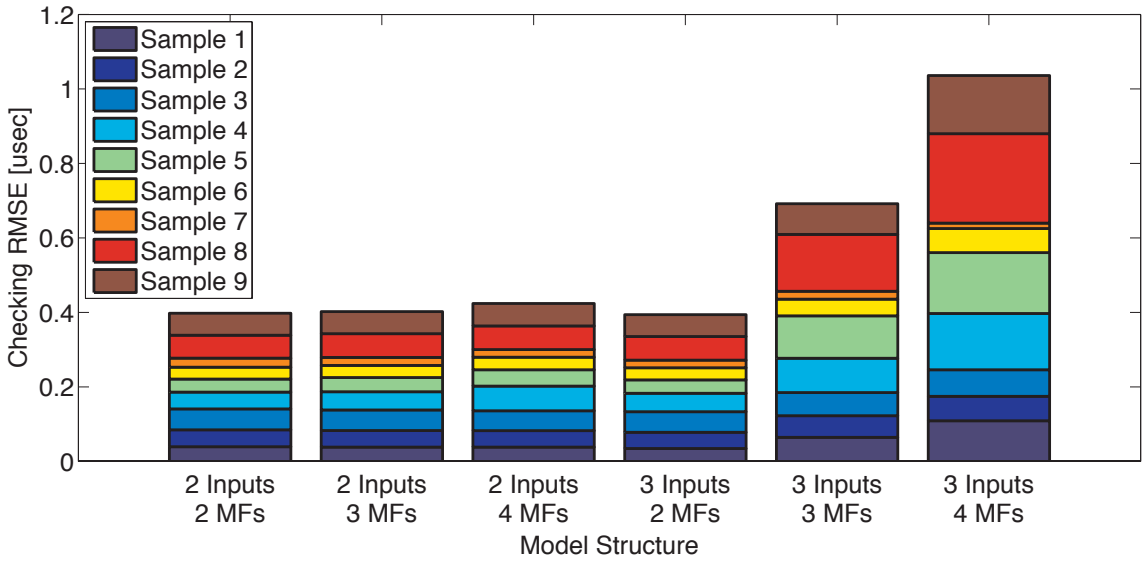

(b)

Figure 92: ToF error compensation model performance for (a) training and (b) checking data

In order to determine the structure with the least overall RMSE, the sum of all training and checking RMSE for each structure was calculated. The structure with the lowest sum was selected. In this case, the structure with three inputs and two membership functions produced the least total error and was selected as the best structure. For this structure, the inputs are the in-process time of flight and two wire feed rate signals delayed by 0.25 and 1.25 s. It was expected that different torch to sensor distances would result in different inputs for each trained model. However, the sum of the RMSE for both the training and checking data for all samples was minimized when the preprocessed wire feed rate at 0.25 and 1.25 s (2.4 mm and 11.9 mm) earlier in the weld were used. Figure 93 shows the offline and model times of flight for Sample 2 (D_{TS} = 56 mm). The RMSE for this sample was reduced by 85.1% from 0.153 μs to 0.023 μs by using the error compensator. The offline and model times of flight for all nine samples are shown versus distance along the weld in Figure 94.

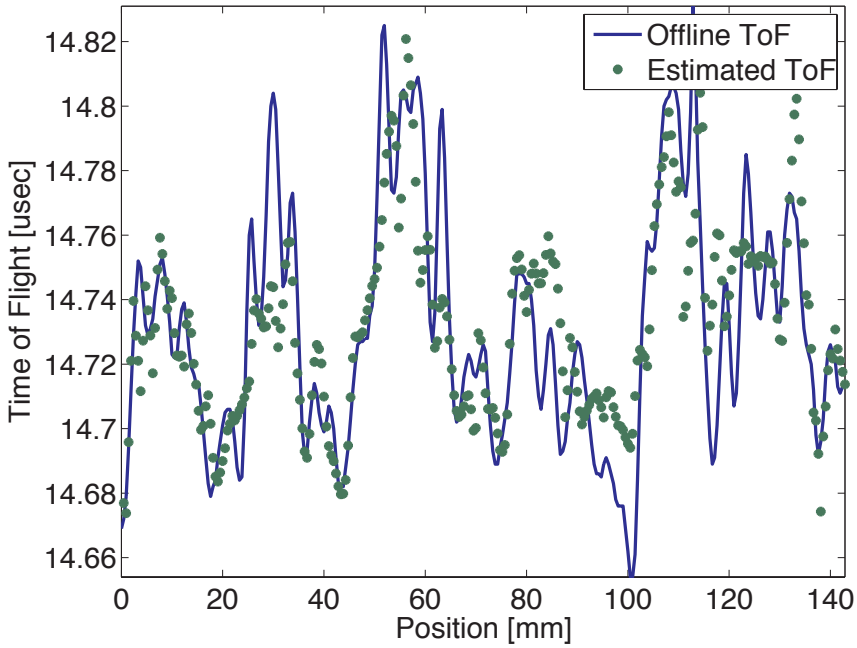

Figure 93: Times of flight measured offline and estimated using the ToF error compensation model for sample 2 ($D_{TS} = 32$ mm)

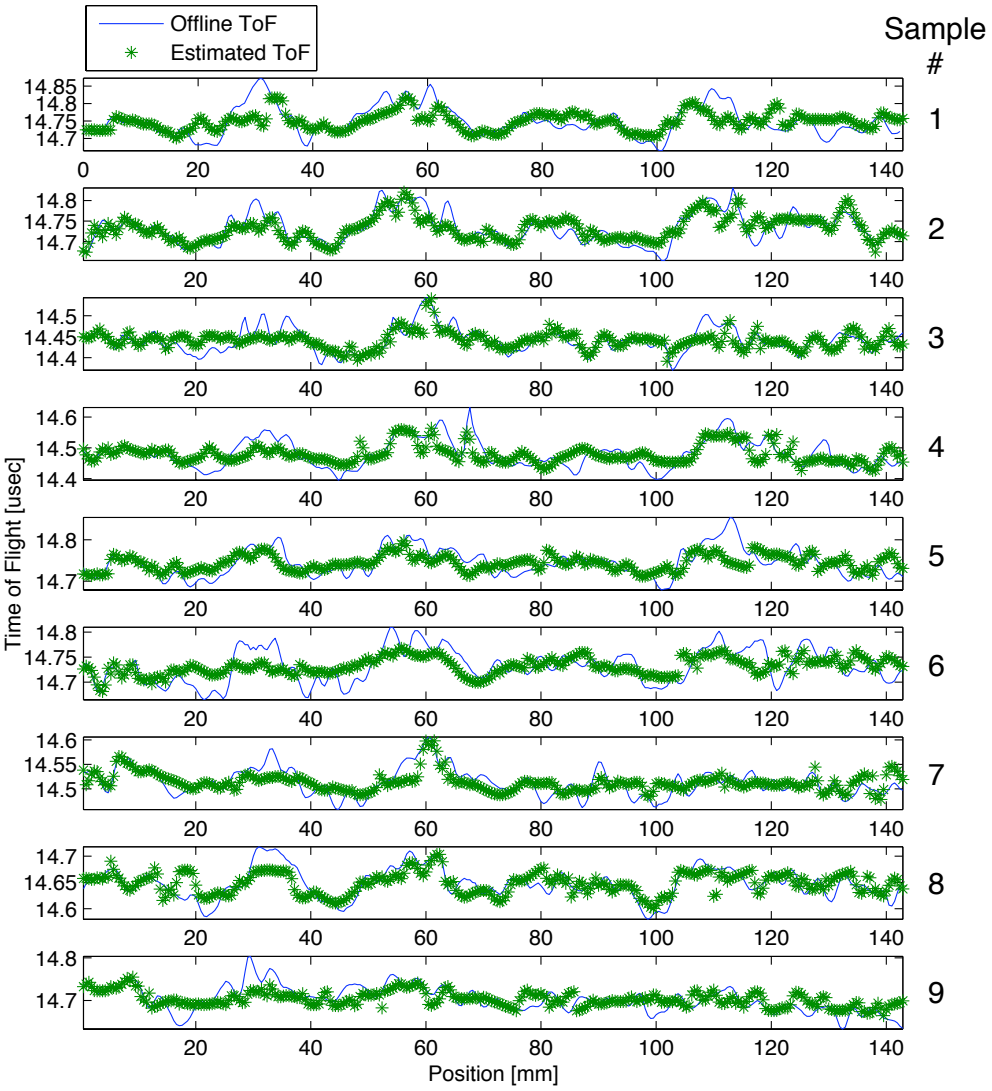

Figure 94: Measured and model times of flight

The RMS model error for the nine samples is presented in Table 3. The maximum RMSE for the training data is 0.035 μs and the maximum checking RMSE is 0.065 μs. The percent reduction in RMSE is also shown, with a minimum of 68.6% and a maximum of 88.5%. The compensator clearly reduced the difference in time of flight for both the training data and the checking data, showing that the system is capable of modeling the process.

Table 3: RMS difference of uncompensated and compensated in-process and offline ToF measurements

Sample	D_{TS} [mm]	Uncompensated RMSE [μs]	Compensated RMSE [μs]	% Reduction	Checking RMSE [μs]
1	56	0.115	0.035	68.8%	0.034
2	56	0.153	0.023	85.1%	0.044
5	51	0.147	0.021	85.4%	0.056
3	51	0.138	0.036	74.1%	0.050
6	45	0.154	0.028	81.9%	0.037
4	45	0.168	0.029	82.9%	0.033
7	38	0.138	0.021	85.2%	N/A
8	32	0.147	0.024	88.5%	0.063
9	32	0.138	0.020	85.0%	0.065

For each sample, the model ToF was used to calculate the penetration depth by using Eq. 111. The actual penetration depth was measured destructively by cutting the sample along the weld seam and capturing an image of the weld bead using a flatbed scanner with a resolution of 1200 dpi. The penetration depth was then calculated using image processing software. The destructively measured penetration depth, offline ultrasonic penetration depth measurement and in-process ToF error compensation model penetration depth for Sample 8 (D_{TS} = 32 mm) are presented in Figure 95.

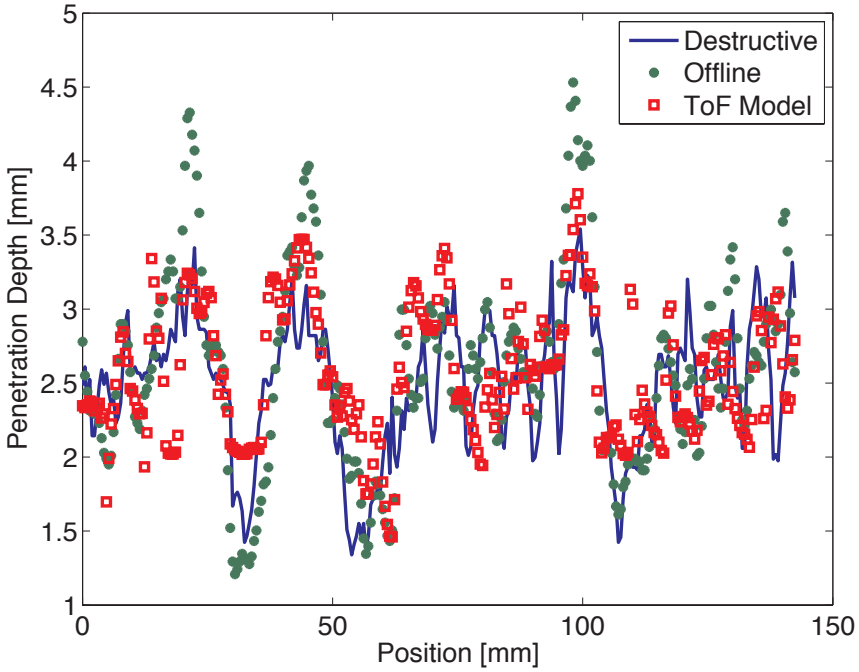

Figure 95: Penetration depths measured destructively, offline after welding and in-process using the ToF error compensation model

The RMSE for the offline measurement and in-process measurement are 0.47 and 0.45 mm, respectively. The model penetration depth has a lower RMSE because the measured penetration depth does not overshoot the actual penetration depth as the offline measurement does. When the penetration depth is not constant throughout the length of the weld, error may be introduced. The laser generates waves that

diffract at locations in the region of the measurement location and then propagate to the EMAT. These waves interfere with the LdLS wave and introduce time of flight measurement error. The amplitude of this error is dependent on the amplitude of the diffracted waves. As discussed in Section 2.2.3, the amplitudes of the diffracted waves depend on the incident and diffraction angles which are in turn dependent on penetration depth. Therefore, the amplitude of the time of flight error is dependent on the penetration depth in the region of the measurement location. The measured penetration depths for all nine samples are shown in Figures 96-98.

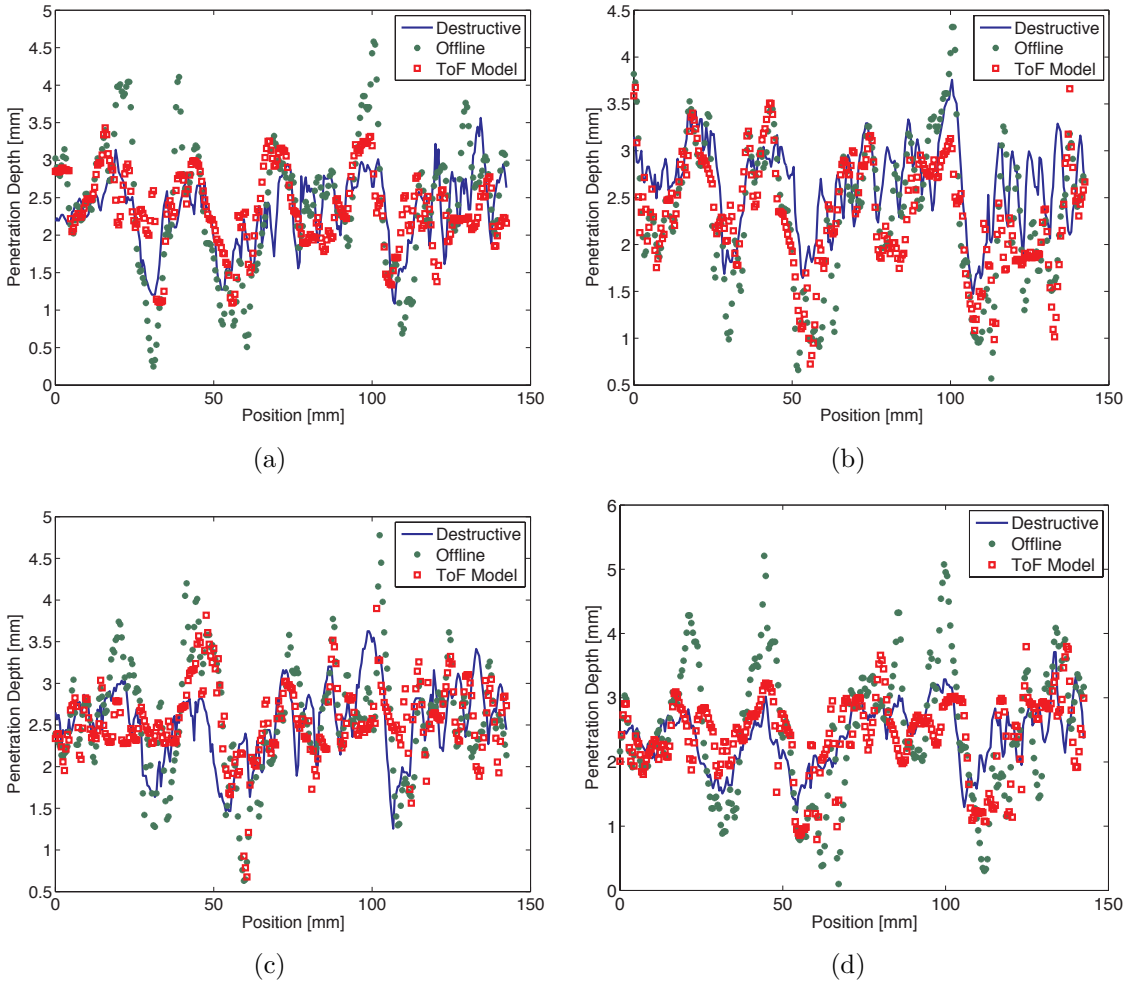

Figure 96: Penetration depths measured destructively, offline after welding and in-process using the ToF error compensation model. Figures 96(a)-96(d) correspond to samples 1-4

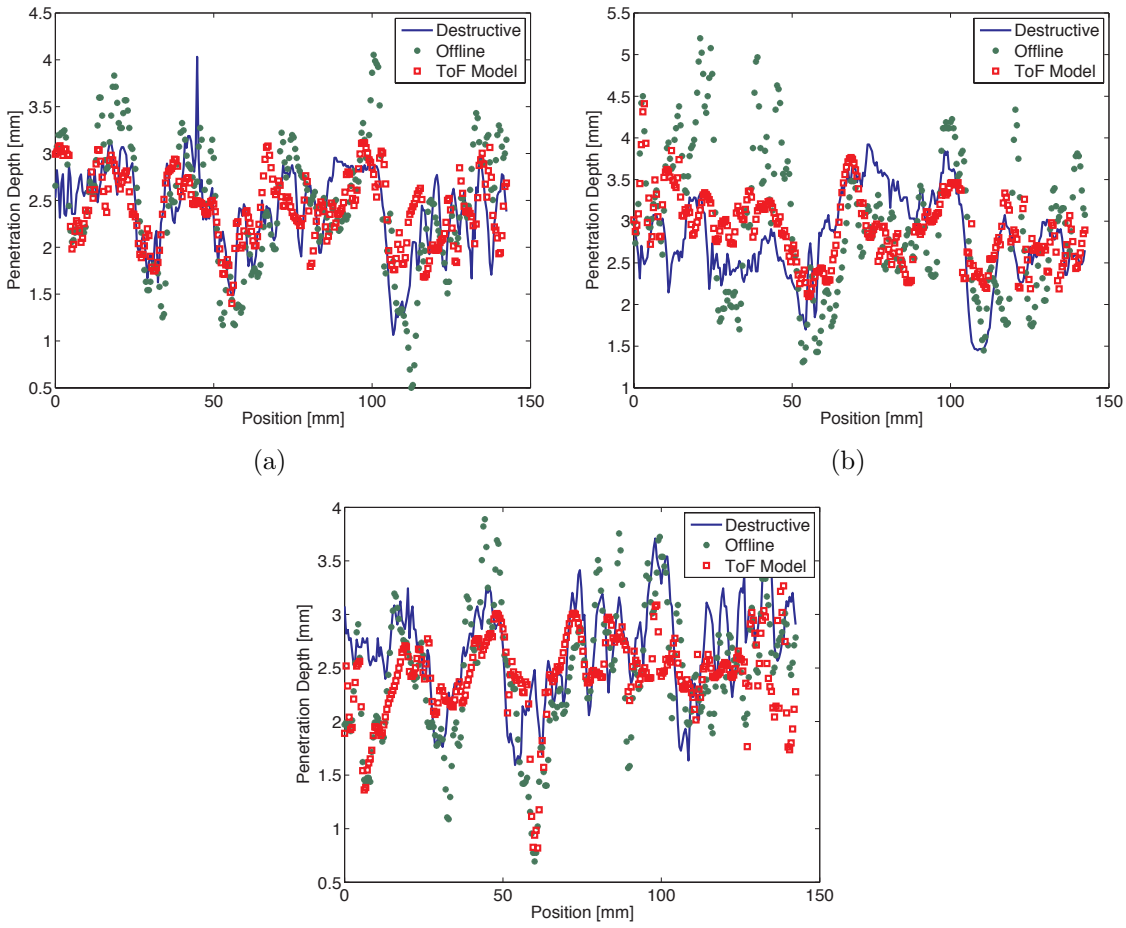

Figure 97: Penetration depths measured destructively, offline after welding and in-process using the ToF error compensation model. Figures 97(a)-97(c) correspond to samples 5-7

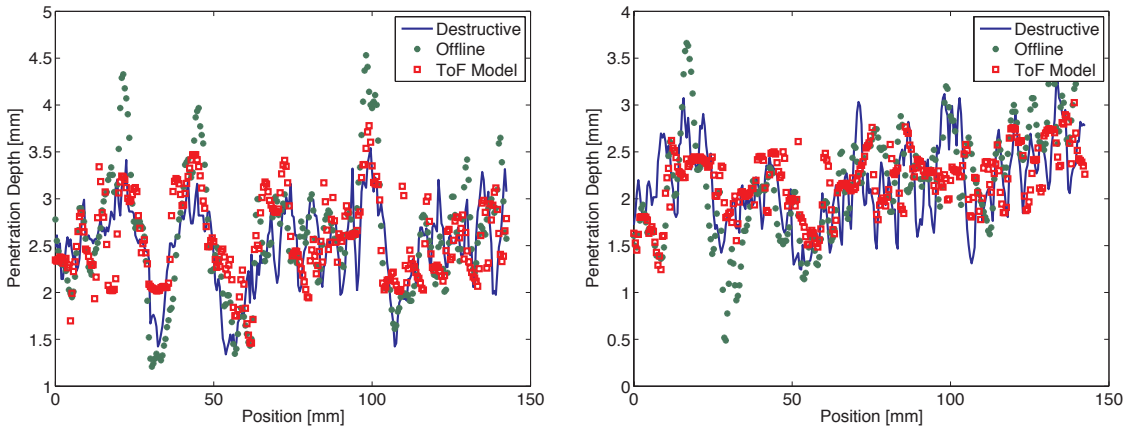

Figure 98: Penetration depths measured destructively, offline after welding and in-process using the ToF error compensation model. Figures 98(a) & 98(b) correspond to samples 8 & 9

The resulting penetration depth RMSE and mean absolute percent error for the nine samples are shown in Table 4. The mean absolute percent error is calculated by averaging the absolute values of the percent error obtained at all measurement locations. For all distances, the model was able to approximate the performance of the offline measurement and drastically reduce the effect of the temperature field on the penetration depth measurement. The offline and ToF error compensation model RMSE errors are comparable for each sample. No clear trend is present in the model error with respect to D_{TS}. This indicates that the model training performance is independent of torch to sensor distance. The error in the offline and in-process compensated penetration depth measurements is relatively large. This error is most likely due to the geometric effects as described earlier. However, the temperature induced error compensation model is very effective at removing the effects of the temperature field present during welding at a range of torch to sensor distances. The training procedure does not require destructive penetration depth measurements and can be performed online if necessary.

Table 4: RMSE and mean of the absolute percent error for offline and in-process compensated penetration depth measurements

Sample	D_{TS} [mm]	Offline RMSE [mm]	Offline Mean Absolute % Error	ToF Model RMSE [mm]	ToF Model Mean Absolute % Error
1	56	0.65	23.3	0.55	20.8
2	56	0.63	20.0	0.61	18.9
3	51	0.61	19.7	0.56	18.2
4	51	0.80	27.6	0.58	21.1
5	45	0.52	17.8	0.41	15.1
6	45	0.89	27.0	0.56	17.8
7	38	0.55	16.7	0.55	16.5
8	32	0.47	15.0	0.45	15.9
9	32	0.52	20.1	0.45	17.8

6.2.2 Destructive Measurement Prediction Model

The second scenario, where destructive penetration depth measurements are available, is now considered. The training procedure is similar, but with a different target output. Rather than the difference of in-process and offline times of flight, the neuro-fuzzy system is trained to produce the penetration depth obtained via destructive measurements. In this way, the model may be able to produce a more accurate measurement than the ToF error compensation model.

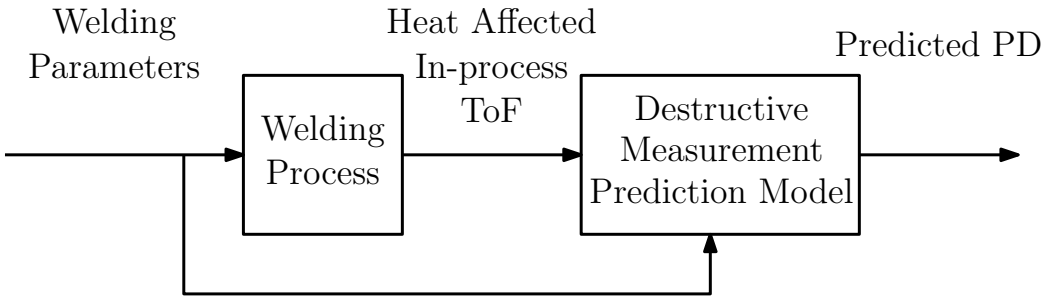

Figure 99: Destructive measurement prediction model block diagram

The model was trained with two and three inputs and with the number of membership functions ranging from two through four as in the previous scenario. The training and checking RMSE are shown in Figure 100 for the six structures. Similar to the ToF error compensation model, the structures with larger numbers of free parameters tend to have larger checking error. For this model, the structure with three inputs and three membership functions per input produces the lowest sum of training and checking error. The penetration depths measured destructively, offline using the LdLS technique, and using the destructive measurement prediction model are shown in Figures 101-103. The destructive measurement prediction model output tracks the destructively measured penetration depth very well. When compared to the penetration depth measured offline using the LdLS ToF technique, it is clear that the model has a much lower error.

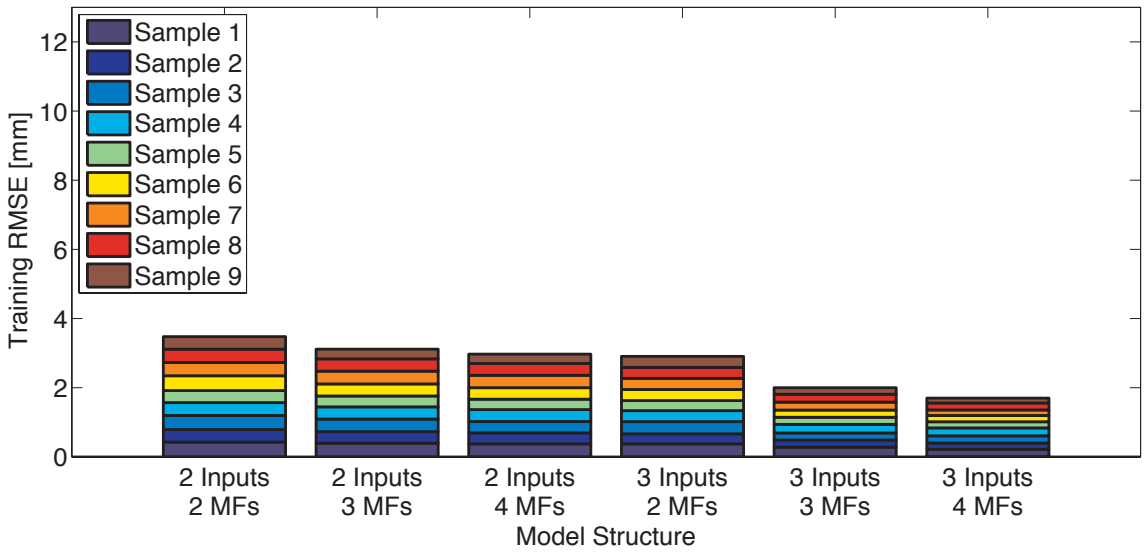

(a)

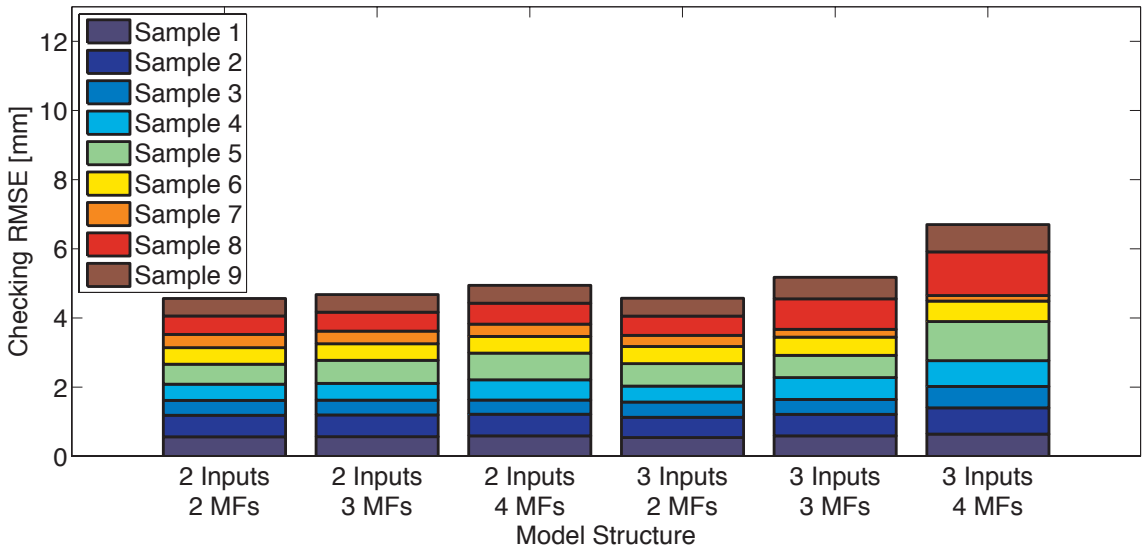

(b)

Figure 100: Destructive measurement prediction model performance for (a) training and (b) checking data

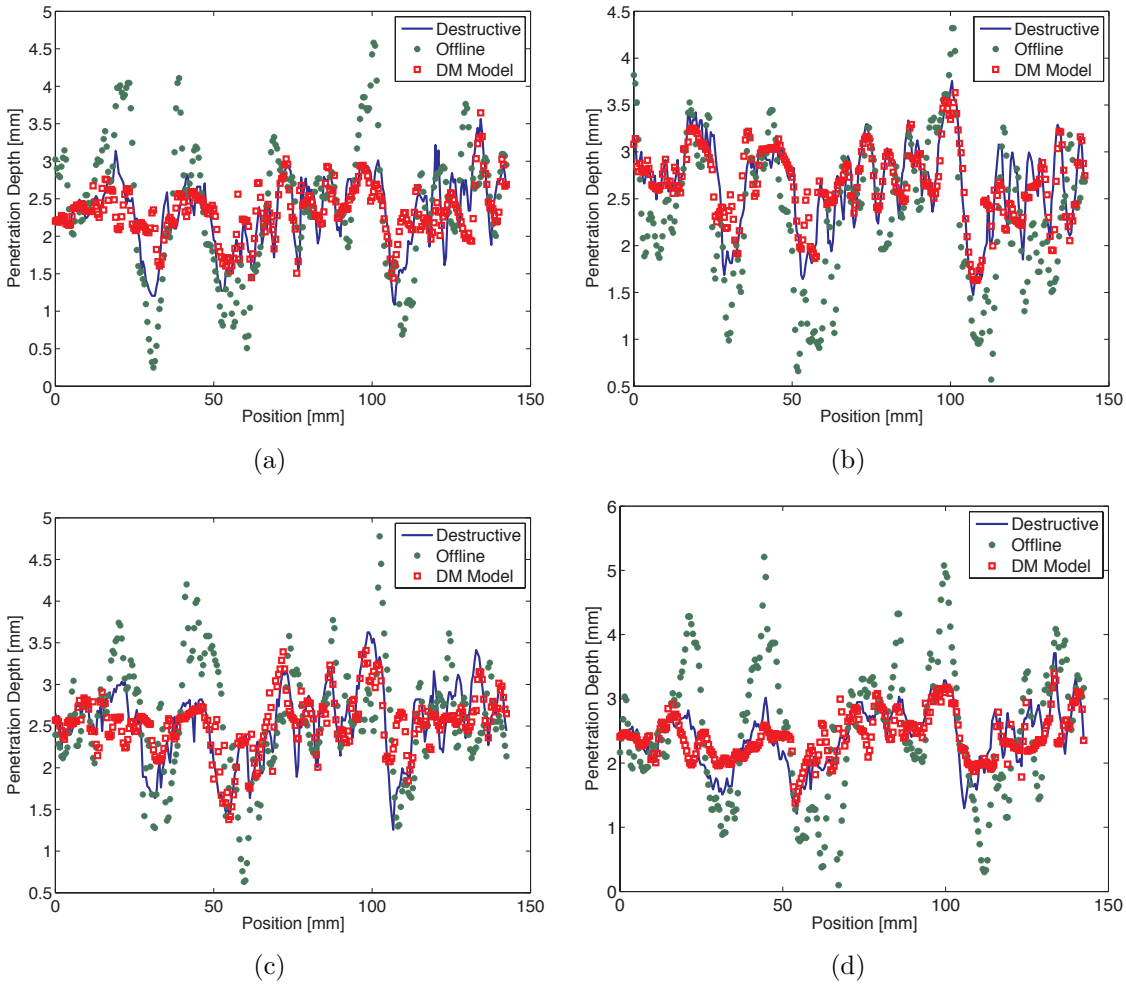

Figure 101: Penetration depths measured destructively, offline after welding and in-process using the destructive measurement prediction model. Figures 101(a)-101(d) correspond to samples 1-4

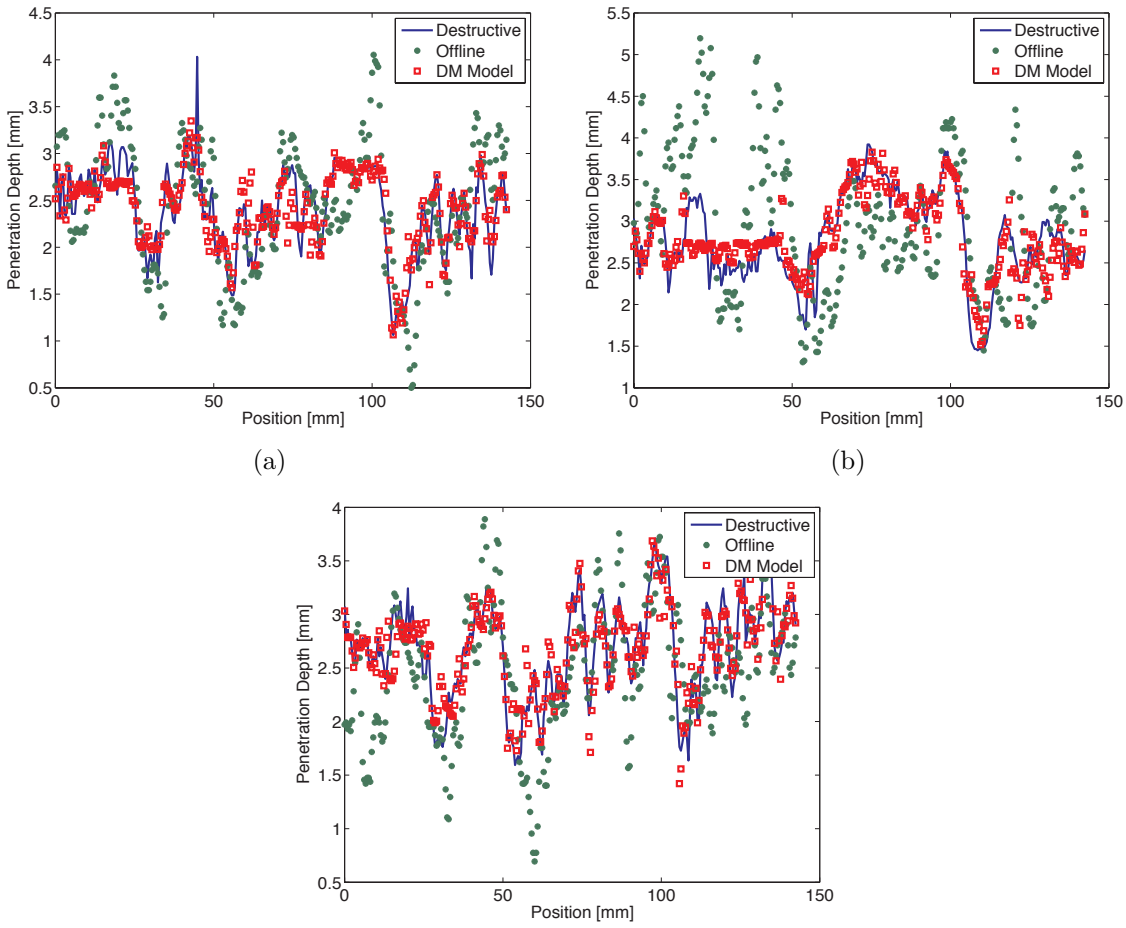

Figure 102: Penetration depths measured destructively, offline after welding and in-process using the destructive measurement prediction model. Figures 102(a)-102(c) correspond to samples 5-7

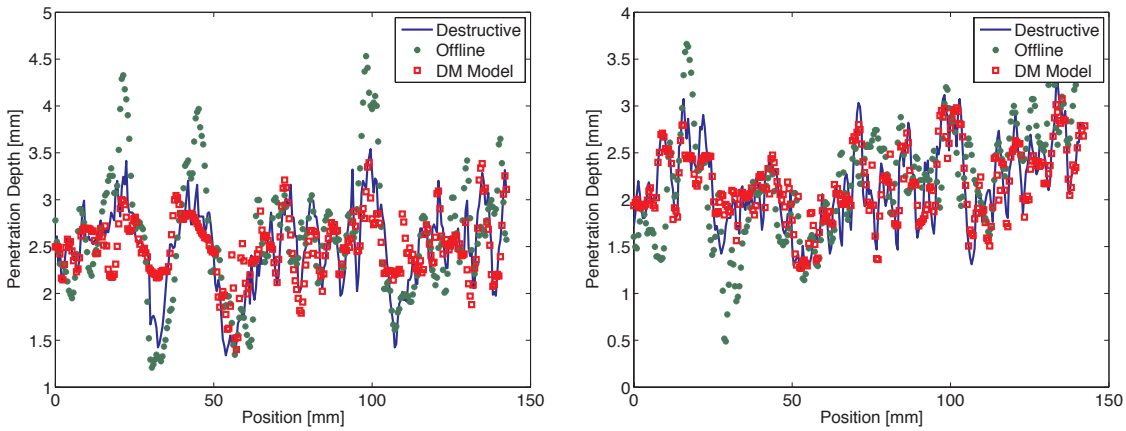

(a) (b)

Figure 103: Penetration depths measured destructively, offline after welding and in-process using the destructive measurement prediction model. Figures 103(a) & 103(b) correspond to samples 8 & 9

The RMSE and mean, minimum, and maximum absolute percent errors for all measurement locations per sample were calculated. The results are shown in Table 5. The RMSE is improved over the ToF error compensation model. The RMSE for the nine samples is comparable across the nine samples ranging from 0.20 to 0.34 mm and shows consistent performance independent of the distance from the torch to the sensor. The mean absolute percent error is good, with a maximum of 12.2% and a minimum of 5.9%. The minimum absolute percent error is very good, with a maximum of 0.05%. The maximum percent error is quite large for some samples. For Sample 1, the maximum percent error is 95.0%. This corresponds to location 31 mm where the actual penetration depth is 1.21 mm and the model penetration depth is 2.35 mm. This combination of a large error and small actual penetration depth results in a large percent error.

Table 5: RMSE and mean absolute percent error for destructive measurement prediction model output

Sample	D_{TS} [mm]	DM Model RMSE [mm]	Mean Absolute % Error	Min Absolute % Error	Max Absolute % Error
1	56	0.34	12.2	0.03	95.0
2	56	0.25	7.3	0.04	40.2
3	51	0.32	10.2	0.01	77.3
4	51	0.31	10.9	0.01	69.9
5	45	0.22	6.7	0.03	46.9
6	45	0.28	8.2	0.00	52.0
7	38	0.20	5.9	0.03	34.0
8	32	0.31	10.5	0.05	64.4
9	32	0.23	9.0	0.03	44.6

In order to show the performance of the offline LdLS technique, the ToF error compensation model and destructive measurement prediction model, the measurements, errors, and absolute percent errors were calculated for five locations in each sample. The locations are 0, 34, 71, 107, and 142 mm. Typically, the ToF error compensation

model performs comparably to the offline LdLS technique. The destructive measurement prediction model performs better overall. The mean absolute percent errors for all measurement locations for the offline LdLS, ToF error compensation model, and destructive measurement prediction model are 23.5, 18.0, and 9.0%, respectively. However, there is variation among the measurement locations. These results indicate that the two models both accomplish their goals. When destructive measurements are not available, the ToF error compensation technique can produce an estimate of the offline weld penetration depth measurement. When destructive measurements are available, the destructive measurement prediction model can be used to yield results with significantly improved performance.

Table 6: Penetration depth measurements obtained destructively, offline via LdLS technique, using ToF error compensation model (ToF Model) and destructive measurement prediction model (DM Model) for Sample 1

Location	0 mm	34 mm	71 mm	107 mm	142 mm
Destructive PD Measurement [mm]	2.18	2.59	2.78	1.13	2.63
Offline PD Measurement [mm]	3.02	2.10	2.88	1.58	2.95
Offline PD Error [mm]	0.84	-0.49	0.10	0.45	0.32
Offline Absolute % Error	**38.5**	**18.9**	**3.6**	**39.8**	**12.2**
ToF Model PD Measurement [mm]	2.85	2.28	3.15	1.53	2.16
ToF Model PD Error [mm]	0.67	-0.31	0.37	0.40	-0.47
ToF Model Absolute % Error	**30.7**	**12.0**	**13.3**	**35.4**	**17.9**
DM Model PD Measurement [mm]	2.20	2.15	2.71	1.44	2.69
DM Model PD Error [mm]	0.02	-0.44	-0.07	0.31	0.06
DM Model Absolute % Error	**0.9**	**17.0**	**2.5**	**27.4**	**2.3**

Table 7: Penetration depth measurements obtained destructively, offline via LdLS technique, using ToF error compensation model (ToF Model) and destructive measurement prediction model (DM Model) for Sample 2

Location	0 mm	34 mm	71 mm	107 mm	142 mm
Destructive PD Measurement [mm]	3.15	2.66	2.83	1.56	2.70
Offline PD Measurement [mm]	3.82	2.55	2.47	1.20	2.68
Offline PD Error [mm]	0.67	-0.11	-0.36	-0.36	-0.02
Offline Absolute % Error	**21.3**	**4.1**	**12.7**	**23.1**	**0.7**
ToF Model PD Measurement [mm]	3.59	2.98	2.55	1.31	2.67
ToF Model PD Error [mm]	0.44	0.32	-0.28	-0.25	-0.03
ToF Model Absolute % Error	**14.0**	**12.0**	**9.9**	**16.0**	**1.1**
DM Model PD Measurement [mm]	3.08	3.13	2.79	1.72	2.75
DM Model PD Error [mm]	-0.07	0.47	-0.04	0.16	0.05
DM Model Absolute % Error	**2.2**	**17.7**	**1.4**	**10.3**	**1.9**

Table 8: Penetration depth measurements obtained destructively, offline via LdLS technique, using ToF error compensation model (ToF Model) and destructive measurement prediction model (DM Model) for Sample 3

Location	0 mm	34 mm	71 mm	107 mm	142 mm
Destructive PD Measurement [mm]	2.53	2.89	2.67	1.06	2.38
Offline PD Measurement [mm]	2.66	2.16	3.02	1.85	2.38
Offline PD Error [mm]	0.13	-0.73	0.35	0.79	0.77
Offline Absolute % Error	**5.1**	**25.3**	**13.1**	**74.5**	**32.4**
ToF Model PD Measurement [mm]	2.99	2.77	2.66	1.76	2.68
ToF Model PD Error [mm]	0.46	-0.12	-0.01	0.70	0.30
ToF Model Absolute % Error	**18.2**	**4.2**	**0.4**	**66.0**	**12.6**
DM Model PD Measurement [mm]	2.52	2.62	2.66	1.07	2.40
DM Model PD Error [mm]	-0.01	-0.25	-0.01	0.01	0.02
DM Model Absolute % Error	**0.4**	**8.7**	**0.4**	**0.9**	**0.8**

Table 9: Penetration depth measurements obtained destructively, offline via LdLS technique, using ToF error compensation model (ToF Model) and destructive measurement prediction model (DM Model) for Sample 4

Location	0 mm	34 mm	71 mm	107 mm	142 mm
Destructive PD Measurement [mm]	3.03	2.36	3.54	1.55	2.65
Offline PD Measurement [mm]	2.98	3.13	2.95	2.29	3.08
Offline PD Error [mm]	-0.05	0.77	-0.59	0.74	0.43
Offline Absolute % Error	**1.7**	**32.6**	**16.7**	**47.7**	**16.2**
ToF Model PD Measurement [mm]	3.02	3.14	3.39	2.97	2.89
ToF Model PD Error [mm]	-0.01	0.78	-0.15	1.42	0.24
ToF Model Absolute % Error	**0.33**	**33.1**	**4.2**	**91.6**	**9.1**
DM Model PD Measurement [mm]	2.70	2.74	3.31	2.36	3.09
DM Model PD Error [mm]	-0.33	0.38	-0.23	0.81	0.44
DM Model Absolute % Error	**10.9**	**16.1**	**6.5**	**52.3**	**16.6**

Table 10: Penetration depth measurements obtained destructively, offline via LdLS technique, using ToF error compensation model (ToF Model) and destructive measurement prediction model (DM Model) for Sample 5

Location	0 mm	34 mm	71 mm	107 mm	142 mm
Destructive PD Measurement [mm]	2.45	2.23	2.51	1.68	3.08
Offline PD Measurement [mm]	2.78	1.63	2.73	1.67	2.57
Offline PD Error [mm]	0.30	-0.60	0.22	-0.01	-0.51
Offline Absolute % Error	**12.1**	**26.9**	**8.8**	**0.6**	**16.6**
ToF Model PD Measurement [mm]	2.35	2.05	3.06	2.22	2.79
ToF Model PD Error [mm]	-0.13	-0.18	0.55	0.54	-0.29
ToF Model Absolute % Error	**5.2**	**8.1**	**21.9**	**32.1**	**9.4**
DM Model PD Measurement [mm]	2.50	2.24	2.60	2.14	3.11
DM Model PD Error [mm]	0.02	0.01	0.09	0.46	0.03
DM Model Absolute % Error	**0.8**	**0.5**	**3.6**	**27.4**	**1.0**

Table 11: Penetration depth measurements obtained destructively, offline via LdLS technique, using ToF error compensation model (ToF Model) and destructive measurement prediction model (DM Model) for Sample 6

Location	0 mm	34 mm	71 mm	107 mm	142 mm
Destructive PD Measurement [mm]	1.72	1.89	3.03	1.31	2.78
Offline PD Measurement [mm]	1.60	1.66	2.25	2.48	3.84
Offline PD Error [mm]	-0.12	-0.23	-0.78	1.17	1.06
Offline Absolute % Error	**7.0**	**12.2**	**25.7**	**89.3**	**38.1**
ToF Model PD Measurement [mm]	1.63	2.03	2.27	1.81	2.26
ToF Model PD Error [mm]	-0.09	0.14	-0.76	0.50	-0.52
ToF Model Absolute % Error	**5.2**	**7.4**	**25.1**	**38.2**	**18.7**
DM Model PD Measurement [mm]	1.94	2.02	2.80	1.64	2.79
DM Model PD Error [mm]	0.22	0.13	-0.23	0.33	0.01
DM Model Absolute % Error	**12.8**	**6.9**	**7.6**	**25.2**	**0.4**

Table 12: Penetration depth measurements obtained destructively, offline via LdLS technique, using ToF error compensation model (ToF Model) and destructive measurement prediction model (DM Model) for Sample 7

Location	0 mm	34 mm	71 mm	107 mm	142 mm
Destructive PD Measurement [mm]	3.08	2.31	2.91	1.81	2.91
Offline PD Measurement [mm]	1.97	1.99	2.41	2.53	2.78
Offline PD Error [mm]	-1.11	-0.32	-0.50	0.73	-0.13
Offline Absolute % Error	**36.0**	**13.9**	**17.2**	**39.8**	**4.5**
ToF Model PD Measurement [mm]	1.89	2.28	2.91	2.32	2.28
ToF Model PD Error [mm]	-1.19	-0.03	0.00	0.51	-0.63
ToF Model Absolute % Error	**38.6**	**1.3**	**0.0**	**28.2**	**21.7**
DM Model PD Measurement [mm]	3.03	2.31	3.08	1.96	2.92
DM Model PD Error [mm]	-0.05	0.00	0.17	0.15	0.01
DM Model Absolute % Error	**1.6**	**0.0**	**5.8**	**8.3**	**0.3**

Table 13: Penetration depth measurements obtained destructively, offline via LdLS technique, using ToF error compensation model (ToF Model) and destructive measurement prediction model (DM Model) for Sample 8

Location	0 mm	34 mm	71 mm	107 mm	142 mm
Destructive PD Measurement [mm]	2.65	2.31	2.95	1.25	2.44
Offline PD Measurement [mm]	2.40	1.37	2.62	1.95	2.14
Offline PD Error [mm]	-0.25	-0.94	-0.33	0.70	-0.30
Offline Absolute % Error	**9.4**	**40.7**	**11.2**	**56.0**	**12.3**
ToF Model PD Measurement [mm]	2.34	2.38	2.69	2.47	2.73
ToF Model PD Error [mm]	-0.31	0.07	-0.26	1.22	0.29
ToF Model Absolute % Error	**11.7**	**3.0**	**8.8**	**97.6**	**11.9**
DM Model PD Measurement [mm]	2.57	2.51	3.18	0.97	0.21
DM Model PD Error [mm]	-0.08	0.20	0.23	0.97	0.21
DM Model Absolute % Error	**3.0**	**8.7**	**7.8**	**77.6**	**8.6**

Table 14: Penetration depth measurements obtained destructively, offline via LdLS technique, using ToF error compensation model (ToF Model) and destructive measurement prediction model (DM Model) for Sample 9

Location	0 mm	34 mm	71 mm	107 mm	142 mm
Destructive PD Measurement [mm]	2.48	2.10	2.74	1.59	2.36
Offline PD Measurement [mm]	2.16	1.14	3.11	2.10	3.17
Offline PD Error [mm]	-0.32	-0.96	0.37	0.51	0.81
Offline Absolute % Error	**12.9**	**45.7**	**13.5**	**32.1**	**34.3**
ToF Model PD Measurement [mm]	2.01	2.44	2.26	2.06	2.99
ToF Model PD Error [mm]	-0.47	0.34	-0.48	0.47	0.63
ToF Model Absolute % Error	**19.0**	**16.2**	**17.5**	**29.6**	**26.7**
DM Model PD Measurement [mm]	2.41	2.12	2.65	2.01	2.35
DM Model PD Error [mm]	-0.07	0.02	-0.09	0.42	-0.01
DM Model Absolute % Error	**2.8**	**1.0**	**3.3**	**26.4**	**0.4**

CHAPTER VII

CONCLUSION, CONTRIBUTIONS AND RECOMMENDATIONS

7.1 Conclusions

The overall objective of this research area is to create a real time weld quality monitoring and control system. Previous research has focused on development of a new sensing technique called the RGLS Time of Flight weld penetration depth measurement technique. The objective of this research is to compensate for the changes in time of flight exhibited when the RGLS ultrasonic technique is used during welding. Initially, the RGLS ToF technique was investigated in order to validate assumptions made during its development. Specifically, the means through which a laser generated Rayleigh wave generated on the top surface of a plate reaches the bottom surface of the plate was determined. It was shown that low frequency components of the Rayleigh wave extend below the top surface of the plate and reach the bottom surface at a critical radial distance from the source. This critical distance was determined via a model based on generalized ray theory and validated experimentally. The model and experimental results were also used to determine the dominant frequency of the Rayleigh wave after it reaches the bottom surface.

With the phenomena behind the RGLS ToF technique determined, the technique was applied towards penetration depth measurement. Surprisingly, the RGLS wave was not present in the received signals. Experiments were performed to determine if the wave was received when the source is located at a variety of distances from the weld. It was shown that the RGLS wave did not reach the receiver at any of the configurations. Since the RGLS wave was not received by the EMAT, an alternative

wave path was selected. Experiments were performed to identify the waves that reach the receiver for a range of sensor placement configurations. Experiments show that the Rayleigh wave traveling along the top surface can be diffracted at the edges of the weld bead, potentially interfering with the wave used to measure penetration depth. The LdLS path was shown experimentally to be the strongest candidate that was not interfered with by other bulk and diffracted Rayleigh waves. A theoretical model was developed to determine LdLS wave amplitude as a function of sensor placement. Using the optimal sensor placement, the LdLS wave was used to measure penetration depth and was shown to perform well.

The inspection system was then used to measure penetration depth during and after welding. The times of flight were measured under both conditions and shown to be larger during welding because of the decreased wave speeds at elevated temperature. The RMS difference in wave speed was shown to decrease as the sensing system was placed further from the welding torch, confirming previous results. The differences in time of flight caused by the temperature field during welding were large enough to produce penetration depth measurement errors as large as 5 mm. In order to improve the in-process penetration depth measurement, two models were created.

First, a temperature induced error compensation model was developed. The model produces an estimate of the offline time of flight based on the in-process time of flight and the time history of the wire feed rate. The estimated offline time of flight is then used to calculate penetration depth. The performance of the model is very good. The RMS difference in the estimated time of flight and the offline time of flight is reduced by a minimum of 68% and as much as 88%. The RMSE of the penetration depth measurement is comparable to that obtained ultrasonically after welding. The model has been shown to effectively compensate for the error introduced by the temperature field present during welding. Development of this model does not require destructive measurements. However, any error in the offline penetration depth measurement will

remain in the model penetration depth. When compared to destructively measured penetration depth, the RMSE of the model output for each sample ranges from 0.41 to 0.61 mm. The mean absolute percent error for all measurements is 20.1%. A second scenario was considered where destructive penetration depth measurements are available for model development. In this case, the destructive measurement prediction model was trained to produce a prediction of the penetration depth directly. The performance of this model is considerably better than the ToF error compensation model. The model output RMSE for each sample ranges from 0.20 to 0.32 mm and the mean absolute percent error is 9.7%. Clearly, the destructive measurement prediction model performs better than the ToF error compensation model. However, in a given application, destructive measurements may not be available. In this case, the ToF error compensation model can provide a penetration depth prediction comparable to offline ultrasonic measurement. In both cases, the model performance is independent of torch to sensor distance. Upon application, the optimal torch to sensor distance can be determined based on application specific constraints. The penetration depth prediction models are a major step toward using laser ultrasonic time of flight based penetration depth measurement techniques as real-time sensors for real-time weld quality monitoring and control.

7.2 Contributions

Major Results:

- Rayleigh waves present on bottom of plates are not created by mode conversion but rather by the extension of wavefront below the top surface
- Generalized Ray theory is an effective method of determining response of plate due to laser sources
- Created in-process weld inspection system capable of measuring penetration

depth during and after welding

- Time of flight error compensation model produces penetration depth prediction with RMSE comparable to that obtained with offline ultrasonic measurement
- Destructive measurement prediction model produces penetration depth prediction with RMSE approximately half that obtained with offline ultrasonic measurement

Experimentally proved:

- Means through which Rayleigh waves propagate to bottom surface of plate is not mode conversion of bulk waves
- Rayleigh waves are only present behind shear wavefront
- RGLS wave was not observed in butt weld samples
- Dominant frequency of Rayleigh waves on the bottom surface is dependent on plate thickness
- Neuro-fuzzy models can dramatically reduce error induced by temperature field
- Neuro-fuzzy models are capable of predicting destructive penetration depth measurements based on in-process time of flight measurements and process inputs

Derived:

- Generalized ray theory source function for thermoelastic laser generation of ultrasound
- Theoretical equation for ToF of Rayleigh waves when received on bottom surface of plates

- Theoretical equation for critical distance from laser source at which Rayleigh waves are present on bottom surface of plates
- Theoretical equation for LdLS ToF
- Theoretical equations that can be used to determine allowable sensor placement for a time of flight based penetration depth sensing technique

Manufactured:

- In-process weld control and inspection system (before proposal)
- Microcontroller firmware for coordination of experimental system (before proposal)
- Welder command interface circuitry (before proposal)
- Data acquisition and system control program (before proposal)
- Trigger sensor for sensing laser firing during welding
- Grounding yoke for LURL EMAT

7.3 Recommendations

The results of this work show that the technique is a significant step towards development of a sensor capable of measuring penetration depth for real time welding control. However, the performance of the technique must be improved before it can be applied towards a commercial system.

1. Implement a directional laser source such as a fiber phased array and design an EMAT with optimized directionality to increase strength of received ultrasound. The error present in penetration depth measurement is partially because of intrinsic sensor preamp noise and noise created by the welding arc. Since signal averaging is

not possible during in-process inspection, the most effective way to increase signal to noise ratio is to increase the amplitude of the received ultrasound.

2. Because other welding parameters such as torch travel velocity, torch standoff, and arc voltage may be used to control weld penetration depth, expand the error compensation model to include these parameters as inputs. Of particular interest is torch travel velocity since this parameter determines the time delay from actuation to sensing for a fixed torch to sensor distance.

3. A thermal distribution sensor could be added to the system in order to provide a direct measurement of the temperature field at the surface of the sample. This may reduce the reliance on training the model with a specific welding machine and permit operation in a wider range of conditions.

REFERENCES

[1] Adolfsson, S., Bahrami, A., and Claesson, I., "Quality monitoring in robotised welding using sequential probability ratio test," vol. vol.2, (Perth, WA, Australia), pp. 635 – 40, 1996.

[2] Andersen, K., Cook, G., Karsai, G., and Ramaswamy, K., "Artificial neural networks applied to arc welding process modeling and control," *IEEE Trans. Ind. Appl. (USA)*, vol. 26, no. 5, pp. 824 – 30, Sept.-Oct. 1990.

[3] Anon, "Gmaw best practices," *Welding Journal (Miami, Fla)*, vol. 85, no. 2, pp. 46 – 50, 2006.

[4] Aussel, J., Le Brun, A., and Baboux, J., "Generating acoustic waves by laser: Theoretical and experimental study of the emission source," *Ultrasonics*, vol. 26, no. 5, pp. 245 – 255, 1988.

[5] Aussel, J. and Monchalin, J., "Precision laser-ultrasonic velocity measurement and elastic constant determination," *Ultrasonics*, vol. 27, no. 3, pp. 165 – 177, 1989.

[6] Babuska, R. and Verbruggen, H., "Neuro-fuzzy methods for nonlinear system identification," *Annual Reviews in Control*, vol. 27 I, pp. 73 – 85, 2003.

[7] Barborak, D., Conrardy, C., Madigan, B., and Paskell, T., "'through-arc' process monitoring techniques for control of automated gas metal arc welding," *Proceedings - IEEE International Conference on Robotics and Automation*, vol. 4, pp. 3053–3058, 1999.

[8] Barnett, R. J., Cook, G. E., Damrongsak, D., and Strauss, A. M., "Through-the-arc sensing and control in pulsed gas metal arc welding," ASM Proceedings of the International Conference: Trends in Welding Research, (Pine Mountain, GA, United States), pp. 1068–1072, ASM International, 1998.

[9] Baskaran, G., Balasubramaniam, K., and Lakshmana Rao, C., "Shear-wave time of flight diffraction (s-tofd) technique," *NDT and E International*, vol. 39, no. 6, pp. 458 – 467, 2006.

[10] Bates, B. and Hardt, D., "Real-time calibrated thermal model for closed-loop weld bead geometry control.," *Journal of Dynamic Systems, Measurement and Control, Transactions of the ASME*, vol. 107, no. 1, pp. 25 – 33, 1985.

[11] Bigand, A. and Messaadi, K., "Arc welding fuzzy control using neural net supervisor," *IEEE International Conference on Fuzzy Systems*, vol. 3, pp. 2003 – 2006, 1996.

[12] Brzakovic, D. and Khani, D. T., "Weld pool edge detection for automated control of welding," *IEEE Transactions on Robotics and Automation*, vol. 7, no. 3, pp. 397 – 403, 1991.

[13] Carlson, N. M. and Johnson, J. A., "Ultrasonic sensing of weld pool penetration," *Welding Journal (Miami, Fla)*, vol. 67, no. 11, pp. 239–246, 1988.

[14] Ceranoglu, A. and Hsing, P. Y., "Propagation of elastic pulses and acoustic emission in a plate - 3. general responses.," *Journal of Applied Mechanics, Transactions ASME*, vol. 48, no. 1, pp. 139 – 147, 1981.

[15] Ceranoglu, A. and Pao, Y. H., "Propagation of elastic pulses and acoustic emission in a plate - 1. theory.," *Journal of Applied Mechanics, Transactions ASME*, vol. 48, no. 1, pp. 125 – 132, 1981.

[16] Ceranoglu, A. and Pao, Y. H., "Propagation of elastic pulses and acoustic emission in a plate - 2. epicentral responses.," *Journal of Applied Mechanics, Transactions ASME*, vol. 48, no. 1, pp. 133 – 138, 1981.

[17] Chapman, R., "Ultrasonic reflection from smooth flat cracks: exact solution for semi-infinite crack.," Tech. Rep. NW/SSD/RR/14/81, CEGB, 1981.

[18] Chen, S., Wu, L., and Wang, Q., "Self-learning fuzzy neural networks for control of the arc welding process," *ICNN 96. The 1996 IEEE International Conference on Neural Networks (Cat. No.96CH35907)*, vol. vol.2, pp. 1209 – 14, 1996.

[19] Chen, W. H., Nagarajan, S., and Chin, B. A., "Weld penetration sensing and control," vol. 972, pp. 268–72, 1988.

[20] Connor, L. P., ed., *Welding Handbook*. Miami, Fl: American Welding Society, 1987.

[21] Cook, G. E., Barnett, R. J., Andersen, K., and Strauss, A. M., "Weld modeling and control using artificial neural networks," *IEEE Transactions on Industry Applications*, vol. 31, no. 6, pp. 1484 – 1491, 1995.

[22] Dixon, S., Edwards, C., and Palmer, S., "A laser-emat system for ultrasonic weld inspection," *Ultrasonics (Netherlands)*, vol. 37, no. 4, pp. 273 – 81, 1999.

[23] Doumanidis, C. C., "Multiplexed virtual torch and distributed-parameter control of automated welding," vol. 1 of *Proceedings of the IEEE Conference on Control Applications*, (BC, BC, Can), pp. 33–40, Publ by IEEE, Piscataway, NJ, USA, 1993.

[24] Fan, Y., Dixon, S., Edwards, R., and Jian, X., "Ultrasonic surface wave propagation and interaction with surface defects on rail track head," *NDT & E Int. (UK)*, vol. 40, no. 6, pp. 471 – 7, 2007.

[25] Govardhan, S. M., Wikle, H. C., Nagarajan, S., and Chin, B. A., "Real-time welding process control using infrared sensing," vol. 3 of *Proceedings of the American Control Conference*, (Seattle, WA, USA), pp. 1712–1716, 1995.

[26] Hull, D., Kautz, H., and Vary, A., "Measurement of ultrasonic velocity using phase-slope and cross-correlation methods," *Mater. Eval. (USA)*, vol. 43, no. 11, pp. 1455 – 60, 1985.

[27] Hutchins, D., Dewhurst, R. J., and Palmer, S., "Directivity patterns of laser-generated ultrasound in aluminum," *J. Acoustical Society of America*, vol. 70, pp. 1362–1369, Nov. 1981.

[28] Jang, J.-S., "Neuro-fuzzy modeling for dynamic system identification," *Proceedings of the Asian Fuzzy Systems Symposium*, pp. 320 – 325, 1996.

[29] Jang, J.-S. R., "Anfis: adaptive-network-based fuzzy inference system," *IEEE Transactions on Systems, Man and Cybernetics*, vol. 23, no. 3, pp. 665 – 685, 1993.

[30] Jian, X., Baillie, I., and Dixon, S., "Steel billet inspection using laser-emat system," *J. Phys. D, Appl. Phys. (UK)*, vol. 40, no. 5, pp. 1501 – 6, 2007.

[31] Kaneko, Y., Yamane, S., Kugai, K., and Ohshima, K., "Neural control of weld pool in the robotic welding," *IAS '94. Conference Record of the 1994 Industry Applications Conference Twenty-Ninth IAS Annual Meeting (Cat. No.94CH34520)*, vol. vol.3, pp. 1914 – 19, 1994.

[32] Kita, A. and Ume, I., "Measuring on-line and off-line noncontact ultrasound time of flight weld penetration depth," *Welding Journal (Miami, Fla)*, vol. 86, no. 1, pp. 9–17, 2007.

[33] Kita, A., *Measurement of weld penetration depth using non-contact ultrasound methods*. Thesis, Georgia Institute of Technology, 2005.

[34] Kovacevic, R. and Zhang, Y. M., "Machine vision recognition of weld pool in gas tungsten arc welding," *Proceedings of the Institution of Mechanical Engineers, Part B (Journal of Engineering Manufacture)*, vol. 209, no. B2, pp. 141–52, 1995.

[35] Krehl, P., Schwirzke, F., and Cooper, A., "Correlation of stress-wave profiles and the dynamics of the plasma produced by laser irradiation of plane solid targets," *J. Appl. Phys. (USA)*, vol. 46, no. 10, pp. 4400 – 6, 1975.

[36] Krylov, V., "On dipole source representation for laser-generated sound," in *Proceedings of the IEEE Ultrasonics Symposium*, vol. 1, pp. 597 – 600, 2002.

[37] Mallat, S., *A wavelet tour of signal procesing*. San Diego: Academic Press, 1999.

[38] Masserey, B. and Fromme, P., "On the reflection of coupled rayleigh-like waves at surface defects in plates," *J. Acoust. Soc. Am.*, vol. 123, no. 1, pp. 88 – 98, 2008.

[39] Mi, B., *Implementation of Fiber Phased Array Ultrasound Generation System and Signal Analysis for Weld Penetration Control*. Dissertation, Georgia Institute of Technology, 2003.

[40] Mi, B. and Ume, C., "Real-time weld penetration depth monitoring with laser ultrasonic sensing system," *Journal of Manufacturing Science and Engineering, Transactions of the ASME*, vol. 128, no. 1, pp. 280–286, 2006.

[41] Mi, B. and Ume, I. C., "Parametric studies of laser generated ultrasonic signals in ablative regime: Time and frequency domains," *Journal of Nondestructive Evaluation*, vol. 21, no. 1, pp. 23–33, 2002.

[42] Mihara, T., Ohtsuka, Y., Cho, H., and Yamanaka, K., "Laser ultrasonic tofd method," in *Review of Progress in Quantitative Nondestructive Evaluation*, vol. 20, (USA), pp. 255 – 62, 2001.

[43] Miller, M., Mi, B., Kita, A., and Ume, I. C., "Development of automated real-time data acquisition system for robotic weld quality monitoring," *Mechatronics*, vol. 12, no. 9-10, pp. 1259–1269, 2002.

[44] Nagarajan, S., Banerjee, P., Chen, W., and Chin, B., "Control of the welding process using infrared sensors," *IEEE Trans. Robot. Autom. (USA)*, vol. 8, no. 1, pp. 86 – 93, 1992.

[45] Nagesh, D. and Datta, G., "Prediction of weld bead geometry and penetration in shielded metal-arc welding using artificial neural networks," *J. Mater. Process. Technol. (Switzerland)*, vol. 123, no. 2, pp. 303 – 12, 2002.

[46] Ochiai, M., Levesque, D., Talbot, R., Blouin, A., Fukumoto, A., and Monchalin, J., "Laser ultrasonic study of crack tip diffraction," *AIP Conf. Proc. (USA)*, no. 657B, pp. 1489 – 96, 2003.

[47] Ohshima, K., Yabe, M., Akita, K., Kugai, K., Kubota, T., and Yamane, S., "Sensor fusion using neural network in the robotic welding," *IAS '95. Conference Record of the 1995 IEEE Industry Applications Conference. Thirtieth IAS Annual Meeting (Cat. No.95CH35862)*, vol. vol.2, pp. 1764 – 9, 1995.

[48] Pao, Y. H. and Gajewski, R. R., "The generalized ray theory and transient responses of layered elastic solids," in *Physical Acoustics* (Mason, W. P., ed.), vol. XIII, pp. 183–265, Academic Press, 1977.

[49] Peng, J., Chen, Q., Lu, J., Jin, J., and van Luttervelt, C., "Real time optimization of robotic arc welding based on machine vision and neural networks," *IECON '98. Proceedings of the 24th Annual Conference of the IEEE Industrial Electronics Society (Cat. No.98CH36200)*, vol. vol.3, pp. 1279 – 83, 1998.

[50] Ravenscroft, F., Newton, K., and Scruby, C., "Diffraction of ultrasound by cracks: comparison of experiment with theory," *Ultrasonics (UK)*, vol. 29, no. 1, pp. 29 – 37, 1991.

[51] Rose, J. L., *Ultrasonic Waves in Elastic Media*. Cambridge University Press, 2004.

[52] Rose, L. R. F., "Point-source representation for laser-generated ultrasound.," *Journal of the Acoustical Society of America*, vol. 75, no. 3, pp. 723 – 732, 1984.

[53] Sanderson, T., Ume, C., and Jaizynski, J., "Experimental and numerical results for intensity modulated laser ultrasonics," *J. Acoust. Soc. Am. (USA)*, vol. 104, no. 4, pp. 2207 – 12, 1998.

[54] Santos, T., Caetano, R., Lemos, J., and Coito, F., "Multipredictive adaptive control of arc welding trailing centerline temperature," *IEEE Trans. Control Syst. Technol. (USA)*, vol. 8, no. 1, pp. 159 – 69, 2000.

[55] Scruby, C. B. and Moss, B. C., "Non-contact ultrasonic measurements on steel at elevated temperatures," *NDT&E International*, vol. 26, no. 4, pp. 177–88, 1993.

[56] Scruby, C. and Drain, L., *Laser Ultrasonics:Techniques and Applications*. New York: Taylor and Francis, 1990.

[57] Song, J.-B. and Hardt, D. E., "Estimation of weld bead depth for in-process control," vol. 22 of *American Society of Mechanical Engineers, Dynamic Systems and Control Division (Publication) DSC*, (Dallas, TX, USA), pp. 39–45, Publ by ASME, New York, NY, USA, 1990.

[58] Takagi, T. and Sugeno, M., "Fuzzy identification of systems and its applications to modeling and control," in *IEEE Transactions on Systems, Man and Cybernetics*, vol. SMC-15, pp. 116–132, 1985.

[59] Umeagukwu, C., Lambert, R., Teese, G., and Jarzynski, J., "Ultrasonic seam tracking in the vicinity of an operating welding torch," *Materials Evaluation*, vol. 48, no. 4, pp. 466–470, 1990.

[60] Viktorov, I. A., *Rayleigh and Lamb waves: Physical theory and applications*. Plenum Press, 1967.

[61] Zhang, Y. M., Kovacevic, R., and Li, L., "Adaptive control of full penetration gas tungsten arc welding," *IEEE Transactions on Control Systems Technology*, vol. 4, no. 4, pp. 394 – 403, 1996.

[62] Zhao, P., Wu, C., and Zhang, Y., "Numerical simulation of the dynamic characteristics of weld pool geometry with step-changes of welding parameters," *Modelling and Simulation in Materials Science and Engineering*, vol. 12, no. 5, pp. 765 – 780, 2004.